Modelling the Flow Behaviour of Gas Bubbles in a Bubble Column

by

Andrew Martin McMahon

Submitted to the Department of Chemical Engineering
in partial fulfilment of the requirements for the degree of

Master of Science in Chemical Engineering

at the

University of Cape Town

December 2009

Supervisor: Dr Randhir Rawatlal

Co-supervisors:
Professor Sue Harrison
Dr Tiri Chinyoka

Plagiarism Declaration

I know the meaning of plagiarism and declare that all the work in this document, save for that which is properly acknowledged, is my own.

Signature Date 8 May 2010

Signed by candidate

Abstract

The bubble column reactor is commonly used in industry, although the fluid dynamics inside are not well understood. The challenges associated with solving multiphase flow problems arise from the complexity of the governing equations which have to be solved, which are typically mass, momentum and energy balances. These time-dependent problems need to include effects of turbulence and are computationally expensive when simulating the hydrodynamics of large bubble columns.

In an attempt to reduce the computational expense in solving bubble column reactor models, a "cell" model is proposed which predicts the velocity flow field in the vicinity of a single spherical bubble. It is intended that this model would form the fundamental building block in a macroscale model framework that does predict the flow of multiple bubbles in the whole column.

The non-linear Navier-Stokes (NVS) equations are used to model fluid flow around the bubble. This study focusses on the Reynolds number range where the linear Stokes equations can be used to accurately predict the flow around the bubble. The Stokes equations are mathematically easier to solve than the NVS equations and are thus less computationally expensive. The validity of the NVS model was tested against experimental data for the flow of water around a solid sphere and was found to be in close agreement for the Reynolds number range 25 to 80. The simulation results from the Stokes flow model were compared with those from the NVS flow model and were similar at Reynolds numbers below 1. The application is then in the partitioning of the bubble column into regions governed by either Stokes or NVS equations.

For the flow of water past a bubble, the error between the Stokes flow model and the NVS flow model was determined for $0.1 < Re < 80$. The Stokes flow model accurately predicted the flow field at Reynolds numbers below 1. At higher Reynolds numbers, the error increased due to the high velocities on the bubble surface and the low velocity region behind the bubble which the NVS model predicted but the Stokes model did not. Although this is a relatively small range of Reynolds number in which the the Stokes solution can be trusted, it is anticipated that the volume fraction of such regions in a bubble column may be relatively high, especially in cases where the bubbles are approximately uniformly suspended. It can therefore be expected that a macroscale model framework

which introduces the Stokes approximation for low-Reynolds number bubbles and Navier-Stokes computations for the remaining can be solved significantly faster than frameworks reliant on Navier-Stokes solutions alone.

Contents

List of Figures

List of Tables

Acknowledgements

Firstly, I would like to take this opportunity to thank my sponsor, SASOL, for funding my MSc. Their financial support has played a very important role in the completion of the project. In addition, I am extremely grateful for the general interest that Cayle Sharrock, my mentor, showed towards my studies. He was always a pleasure to work with.

In no particular order, I would like to acknowledge those individuals who have made this project possible. Of course by naming people, I run the risk of making serious omissions. If I do, I apologise and ask that you know that I am not any less grateful for your help over the years.

My supervisor, Dr Randhir Rawatlal deserves a very special thanks for his continued support throughout the course of the project. More importantly, I would like to add that my confidence in problem solving has increased substantially which is partially due to my passion for the field of research of Computational Fluid Dynamics (CFD) which my supervisor has given me the freedom to explore and partially due to the frequent discussions we engaged in regarding this field.

Michael Rhapson played a crucial role in the completion of the project. He was always interested in developing ideas which were related to my work and was very generous with his time. He provided me with direct technical support for the computer programming which was a large and challenging component of my project and always seemed to have answers when I ran into problems regarding the mathematics. I thoroughly enjoyed working with Michael and appreciate his unique interest in multidisciplinary problems. This short acknowledgement is by no means sufficient thanks for the large number of hours that you gave up of your own time to help me.

I am very grateful for the support that the staff and students of CERECAM have given me. Their technical help in the field of CFD in general, the Finite Element Method and DEAL.II has been tremendous. Professor Daya Reddy, the director of CERECAM, facilitated the involvement of students in other research groups with CERECAM and provided excellent guidance for students such as myself. Dr Andrew McBride ran the DEAL.II user group which gave me the opportunity to learn how to use the DEAL.II software from scratch. He was also very generous with his time in helping me with specific technical issues regarding both the FEM mathematics and the computational aspects. JP Pelteret, whom I met in the user group, helped me get going with the software and was always interested in the challenges associated with my project despite the fact that

he was solving a very different research problem. Dr Victor Udoewa gave me some very good advice during critical stages of the project and was also always ready to discuss ideas. My colleague from Chemical Engineering, Alexey Cherkaev was always willing to help me with the FEM mathematics, IT problems as well as giving me some interesting ideas to think about for my project. I would like to thank every person in the DEAL.II user group for their support. Dr Case Bakker was very kind to help set up Linux on my computer during the early stages of the project.

I have also received plenty of support from my co-supervisors, Professor Sue Harrison and Dr Tiri Chinyoka. Outside of the university, I would like to thank Martin Kronbichler from Uppsala University for his permission for me to build on his very well developed code and for some of the very useful coding tips that he shared with me. My twin brother, Peter, helped me immensely with getting confident at programming during the early stages of the project and always gave me quality advice.

A very big thanks goes out to all of my colleagues in Chemical Engineering and more specifically CEBER for their support of my work in general. Thanos Kotsiopoulos deserves a special mention for his involvement in the progression of my research.

Finally I would like to thank God almighty for giving me the strength to complete this work. My family and friends have helped encourage me to perform to my best ability and my father gave me the financial edge as well. My digsmate Marco Becker was always there to support my interests, including my passion for the game of Squash which helped clear my mind at the end of each day.

Chapter 1

Introduction

1.1 The Bubble Column Reactor

The bubble column reactor is often used in industry due to its high heat and mass transfer rates as well as its simplicity of design and hence ease of construction for even large liquid volumes (Jakobsen et al., 2005). Typical processes which use bubble columns include absorption, bioreactions and catalytic slurry reactions. The bubble column reactor consists of an upright cylindrical or rectangular vessel, with an aspect ratio typically between 2 and 10 (Lapin and Lubbert, 1994). It contains a liquid through which a gas, fed in at the bottom via a sparger, is bubbled. In most columns the gas is fed in at a central point at the bottom and the bubble plume rises directly above it. This then causes an upwards flow of liquid in the center of the column and a downwards flow of both liquid and some bubbles near the walls of the column. Figure 1.1 illustrates the flow behaviour inside a typical bubble column. This is a result of the large contact area of the gas as well as the turbulent nature of the flow (Delnoij, 1998).

The flow in gas-liquid bubble columns is generally complex and unsteady (Delnoij, 1998). The fluid dynamics in bubble columns are thus not well understood. Delnoij (1998) categorised three flow regimes that prevail inside a bubble column, illustrated in Figure 1.2. The first is the homogeneous flow regime which consists of many small bubbles distributed evenly in the column. The liquid flows upwards with the bubbles and down between the bubbles. This behaviour is found at low superficial gas velocities up to 1.7 cm/s. At higher gas velocities, bubbles of different sizes move upwards in clusters and bubble coalescence and breakup occurs at gas velocities greater than 2.1 cm/s (Chen et al., 1994). The bubbles then form a central bubble stream which rotates and shifts laterally. The liquid flows upwards with the bubble stream and down near the column wall. Vortices exist near the wall, and such regions have good mixing characteristics. The

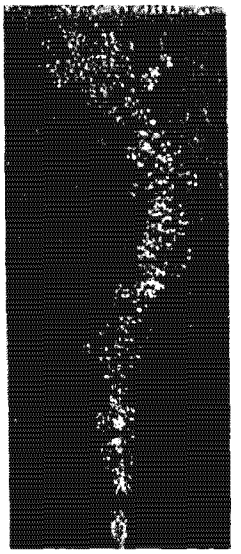

Figure 1.1: An example of bubble movement in a flat bubble column (Becker et al., 1999).

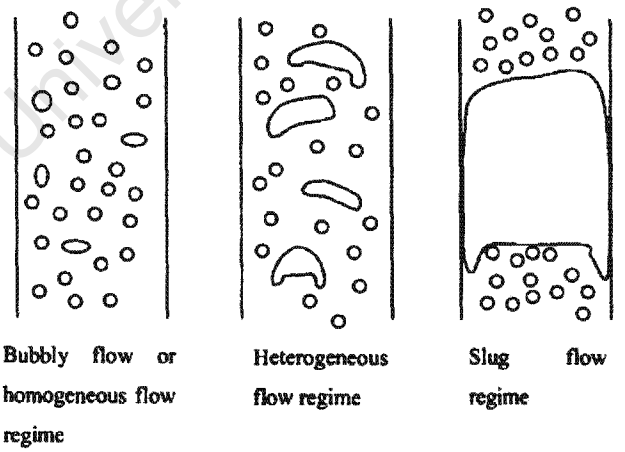

Figure 1.2: Flow regimes in the bubble column for varying superficial gas velocity (Delnoij, 1998).

regime is known as the vortical-spiral flow regime. The flow field is dynamic due to the existence of more than one bubble stream and the movement of the vortices. This flow regime is illustrated in Figure 1.3. At gas velocities greater than 4.9 cm/s, the flow is chaotic. Momentum is transferred by the roll-up and shedding of bubble wakes (Fan and Tsuchiya, 1990). At even higher superficial gas velocities the slug flow regime characterises the flow where bubbles with diameters as wide as the column exist as shown in Figure 1.2.

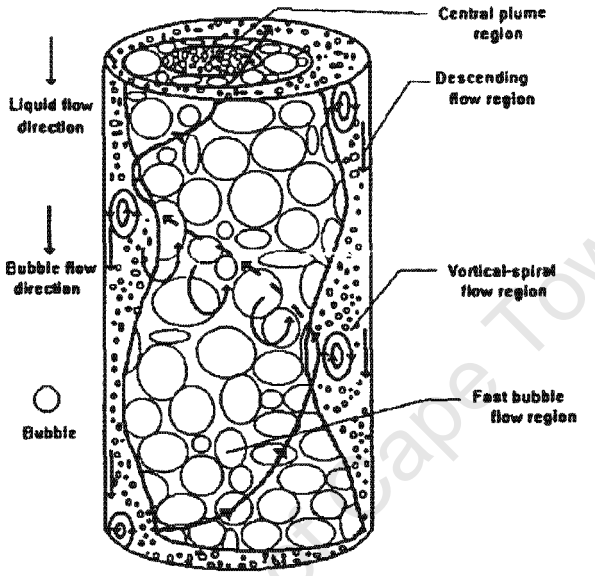

Figure 1.3: Detailed flow structure of the vortical-spiral flow regime for a gas-liquid bubble column (Chen et al., 1994).

1.2 Modelling Challenges

Multiphase flow appears in almost every processing technology, where the material involved is required to flow at some stage (Brennen, 2005). Generally speaking, it is still an important topic of research in science and engineering. A thorough understanding of the multiphase flow that takes place inside a bubble column is necessary for the design and scale-up of such reactors (Jakobsen et al., 2005).

The Navier-Stokes equations, which include mass and momentum balances, are used to model the flow fields of the continuous phase and the gas bubbles which exist in a bubble column. The solution of these equations are the velocity and pressure fields. An energy balance may be solved simultaneously to predict the temperature distribution.

When modelling a multiphase system, the general approaches include (i) solving the NVS (Navier-Stokes) equations for each phase separately, with transport occurring through the interface between the phases, (ii) the Euler-Lagrangian approach, which models the continuous phase with the Navier-Stokes and continuity equations, but the dispersed particles (bubbles) are modelled as moving boundaries using Newtonian equations of motion, with the fluid flow inside these boundaries being ignored and (iii) the Euler-Euler or Eulerian method which models the entire system as a pseudo-homogeneous phase.

The field of multiphase flows covers a wide range of engineering applications, and is evolving from one in which empirical data is a major component of the design process to one in which analysis and modelling are used to complement design and control (Crowe et al., 1998). Typical multiphase flows include gas-liquid flows, which could consist of a gas dispersed in a liquid, and vise-versa, or of two completely separated fluids. Gas-solid flows occur when solid particles are suspended in a gas, and liquid-solid or slurry flows consist of a solid suspended in a liquid. Three-phase flow could consist of bubbles in a slurry flow. A dispersed phase in a continuous phase is defined such that a particle travels from one point to another whilst remaining in the same medium. Some industrial applications of multiphase flows include spray-drying, where a liquid material is atomized subject to hot gases, and emerges as a powder, the removal of particles and droplets from industrial effluents, the transport of material by air or liquids, fluidisation and coal powder furnaces.

The challenges associated with solving multiphase flow problems arise from the complexity of the governing equations which have to be solved with the exchange of mass, momentum and energy across moving boundaries. In the case that governing equations are formulated for the continuous phase, and that boundary conditions are prescribed for

the dispersed phase, the computational grid would have to be at least as small as the smallest particle. An alternative solution is to use the Euler-Euler model with equations based on the average properties of the flow (Crowe et al., 1998). Figure 1.4 illustrates the many variables associated with this challenge.

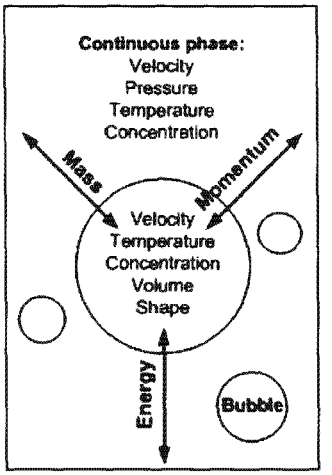

Figure 1.4: Diagram illustrating the interacting variables between the continuous phase and the dispersed phase (bubbles).

1.3 The Navier-Stokes Equations

The Navier-Stokes (NVS) equations are the governing equations for fluid flow. These are the classical means of solving fluid flow problems and are widely used in practice. A thorough framework of these NVS equations is established here, from which the rest of the modelling discussion will draw. This set of equations includes mass, momentum and energy balances, which are all solved simultaneously over the domain of interest. In this project they model the continuous phase (water) only, and are not used to solve for the gas inside the bubble. The mass balance may be represented in the form eq. (1.1) (Navier, 1822).

$$\frac{\partial \rho}{\partial t} + \nabla \cdot (\rho \mathbf{v}) = 0 \tag{1.1}$$

In the case that the fluid is incompressible, as considered in this study, where the continuous phase is water and can be approximated as an incompressible fluid, the mass balance equation reduces to the continuity equation, eq. (1.2) due to constant fluid density.

$$\nabla \cdot \mathbf{v} = 0 \tag{1.2}$$

The momentum balance is given in eq. (1.3). The momentum balance was originally derived in the paper released by Navier (1822).

$$\rho \frac{\partial \mathbf{v}}{\partial t} + \rho \mathbf{v} \cdot \nabla \mathbf{v} = -\nabla p + \mu \nabla^2 \mathbf{v} + \mathbf{f} \tag{1.3}$$

The terms on the left hand side of equation (1.3) represent the rate of change of momentum. The first term describes the local variation of velocity with time at a given point, whilst the second term, which is the non-linear convective term, describes the variation of velocity over a position in space. We note that it is still possible to observe non-zero acceleration even if $\frac{\partial \mathbf{v}}{\partial t} = 0$ because the convective term accounts for fluid particles being accelerated, whereas the flow field as a whole may be steady. The terms on the right hand side of equation (1.3) represent the forces acting on the fluid. The first term represents the pressure force, the second the viscous force where $\mu\ [kg/m \cdot s]$ is the fluid viscosity, and the third body forces such as gravity.

The total derivative is often used to represent the terms on the left hand side, thus another form of the momentum balance equivalent to equation (1.3) is eq. (1.4).

$$\rho \frac{D\mathbf{v}}{Dt} = -\nabla p + \mu \nabla^2 \mathbf{v} + \mathbf{f} \tag{1.4}$$

The energy balance equation is derived from the first law of thermodynamics, which states that the rate of change of energy of a fluid particle is equal to the rate of heat addition to the particle plus the rate of work done on that particle. The energy balance equation for an incompressible fluid may be represented in the form eq. (1.5).

$$\rho C_P \frac{DT}{Dt} = -P div \mathbf{v} + k \nabla^2 T + \Phi + S \tag{1.5}$$

The variable Φ is defined in eq. (1.6).

$$\Phi = 2\mu\left[\left(\frac{\partial v_x}{\partial x}\right)^2 + \left(\frac{\partial v_y}{\partial y}\right)^2 + \left(\frac{\partial v_z}{\partial z}\right)^2\right] + \mu\left(\frac{\partial v_x}{\partial y} + \frac{\partial v_y}{\partial x}\right)^2 + \mu\left(\frac{\partial v_x}{\partial z} + \frac{\partial v_z}{\partial x}\right)^2 + \mu\left(\frac{\partial v_y}{\partial z} + \frac{\partial v_z}{\partial y}\right)^2 \tag{1.6}$$

In equation (1.5), $\rho\,[kg/m^3]$ is the density, $C_P\,[kJ/kg{\cdot}K]$ the heat capacity and $k\,[W/m{\cdot}K]$ the thermal conductivity of the fluid. In most cases, these variables depend on the temperature, $T\,[K]$. S is the source term which includes forms of energy such as gravitational potential energy (Versteeg and Malalasekera, 2007).

Appropriate initial and boundary conditions (BC's) must be specified along with the equations in order for a solution to be obtained, which is the velocity, pressure and temperature fields in the space.

The Navier-Stokes equations can also be written in a dimensionless form in terms of the Reynolds number, which is the ratio of inertial to viscous forces, and is commonly used in fluid dynamics. In this case, each term in the NVS equations is dimensionless.

When doing so, a modified pressure term, $P_m{}'$ appears, which is the pressure field due to the flow only. It is useful for problems where gravity effects can be isolated from the boundary conditions. Equations (1.7) and (1.8) are the dimensionless forms of the mass and momentum balance equations respectively.

$$\nabla' \cdot \mathbf{v}' = 0 \tag{1.7}$$

$$\frac{D\mathbf{v}'}{Dt'} = -\nabla' P_m{}' + \frac{1}{Re}(\nabla')^2\mathbf{v}' \tag{1.8}$$

The dimensionless variables are defined in equations (1.9) to (1.12) below.

$$\mathbf{v}' = \frac{\mathbf{v}}{V_o}, \tag{1.9}$$

$$x' = \frac{x}{L}, \quad y' = \frac{y}{L}, \quad z' = \frac{z}{L}, \quad t' = \frac{tV_o}{L}, \tag{1.10}$$

$$P_m{}' = \frac{(p - p_o - \rho g h_v)}{\rho V_o{}^2}, \tag{1.11}$$

$$Re = \frac{\rho L V_o}{\mu}. \tag{1.12}$$

The variables L, V_o, p_o and h_v are reference quantities (Clift et al., 1978).

1.4 Turbulence

Turbulence is essentially the chaotic behaviour of a fluid at high Reynolds numbers and despite decades of research remains a difficult regime to model and predict. The Navier-Stokes equations for laminar flow are usually modified to be able to predict turbulent effects, although direct numerical simulations (DNS), which solves the Navier-Stokes equations on an extremely fine grid, have been performed to study the interaction between turbulence and bubbles. Due to the high computational cost of such simulations, studies in this area are limited (Pan and Banerjee, 1997). Brennen (2005) stated that turbulence could result in particle breakup and agglomeration, as well as the particles in turn affecting the turbulence itself.

Figure 1.5 illustrates the development of 2-D turbulence. As the Reynolds number is increased, the flow becomes increasingly chaotic on different time and length scales (Bohr et al., 1998). A major challenge in multiphase flow is the modelling of turbulence and its effect on mass, momentum and energy transfer. There are few accurate models for single-phase flows, and the effects of turbulence on particle motion are important except when massive particles are introduced into the system. In turbulent flows, vortical eddies are responsible for strong mixing. These eddies transport fluid via convection, which carry energy and momentum. Due to the momentum transfer, the fluid experiences additional shear stresses, know as the *Reynolds stresses*. The Reynolds-averaged Navier-Stokes equations include these Reynolds stresses. Various turbulence models are available to model these individual terms, such as the $k - \varepsilon$ and Reynolds stress models (Versteeg and Malalasekera, 2007).

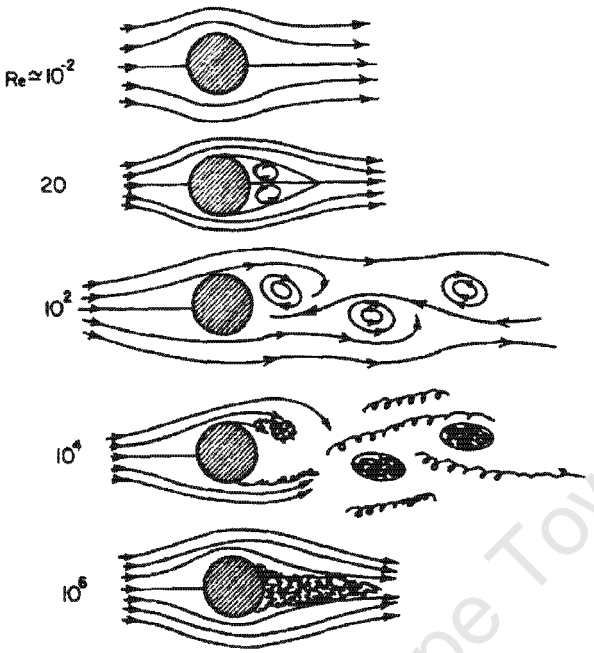

Figure 1.5: Rough sketch of flows around a cylinder at different Reynolds numbers, illustrating the development of turbulent flow (Bohr et al., 1998).

1.5 Summary

The modelling of multiphase flows has many complications which include the dynamic (time-dependent) solution of multiple partial differential equations (PDE's) which may be non-linear, moving boundaries and many process variables. In addition, the particles may experience changes in shape and size and the flow could be turbulent. Such phenomena cause the modelling and simulating of these flows to be complex, where a large amount of computational power is often needed, but cannot be acquired. This is despite various attempts in the modelling approaches to reduce the amount of computational power. In this thesis, a new modelling approach will be proposed with the intention of reducing the computational effort in simulating the operation of a bubble column.

Chapter 2

Literature Review

Bubble columns are widely used in the chemical industry, e.g., as strippers in petrochemical processes, as fermenters in bioprocesses, as slurry reactors in catalytic processes, etc. They are inexpensive to construct and easy to maintain, exhibiting power-efficient mixing. The last is particularly significant in reducing energy usage. However, scale-up using dimensional analysis is not possible due to their complex fluid dynamics.

The hydrodynamics of bubble columns is dependent on the scale of investigation. At large scales, the turbulent flow structure is determined by the dimensions of the vessel, while on a medium scale, the eddy structures are determined largely by the energy dissipation rate, and on small scales, the viscous forces control the flow structure (Lapin and Lubbert, 1994).

This chapter reviews the field of bubble column modelling by categorising the modelling approaches into three parts. The first part includes models associated with just the liquid phase, the second part with the fluid in close proximity to a hypothetical gas bubble, and the third with both the liquid and the bubbles. Figure 2.1 highlights three regions in a typical bubble column, indicating that region one consists of a liquid and a swarm of gas bubbles, region two liquid only and region three a single gas bubble relatively far from other bubbles. The modelling of each of these regions are discussed in each part accordingly. Finally numerical methods for solving the associated partial differential model equations are reviewed in this chapter.

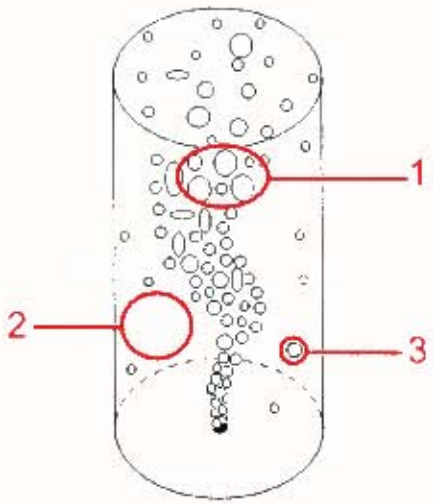

Figure 2.1: Drawing of a bubble column with both liquid and bubbles existing in region 1, liquid only in region 2 and a single gas bubble in region 3.

2.1 Modelling the Liquid Phase

2.1.1 Solving a Single-Phase Flow Problem

When solving a single-phase flow problem, the Navier-Stokes equations must be solved over the domain together with appropriate initial and boundary conditions. In the case of incompressible flow, the general mass balance is called the continuity equation and may be represented in the form eq. (2.1).

$$\nabla \cdot \mathbf{v} = 0 \tag{2.1}$$

The unsteady momentum balance for incompressible flow is shown in eq. (2.2).

$$\rho \frac{\partial \mathbf{v}}{\partial t} + \rho \mathbf{v} \cdot \nabla \mathbf{v} = -\nabla p + \mu \nabla^2 \mathbf{v} - \mathbf{f} \tag{2.2}$$

Equations (2.1) and (2.2) are named after Claude-Louis Navier and George Gabriel Stokes. The momentum balance was originally derived in the paper released by Navier (1822). In the case that the Reynolds number is much less than 1, the second term in equation (2.2) may be neglected, and the equation then becomes the momentum balance for Stokes flow given in equation (2.3) (Clift et al., 1978).

$$\rho \frac{\partial \mathbf{v}}{\partial t} = -\nabla p + \mu \nabla^2 \mathbf{v} + \mathbf{f} \tag{2.3}$$

Equations (2.1) and (2.2) are generally solved over either a 2D or a 3D domain. The solution to the NVS equations is the velocity vector field and the scalar pressure field inside the domain. An energy balance may be solved together with the mass and momentum balances to give the temperature field. As limited analytical solutions to the NVS equations are available, numerical methods are used in practice to solve the partial differential equations.

2.1.2 Turbulence

In turbulent flows, eddies or rotational flow structures are formed that bring together fluid particles spaced far apart. Hence effective mixing occurs which gives high values of diffusion coefficients for mass, momentum and heat transfer. Another type of rotational flow is the vortex, where the fluid moves around in a circle. The process of vortex stretching occurs when large turbulent eddies extract energy from the mean flow (Versteeg and Malalasekera, 2007).

For flow at a given Reynolds number, there usually exist transition zones over which the flow becomes fully turbulent. For example, in the case of jet flow where fluid flows out of an orifice, vortex roll-up which is the formation of a vortex on a solid surface, occurs at the nozzle. Vortex pairing is the coupling of two vortices into a larger vortex and takes place alongside the nozzle. Further downstream, the vortices become distorted and many small eddies are generated. The process by which the surrounding fluid is drawn into the turbulent zone is known as entrainment, and is the main mechanism for the spread of turbulent flows. It has been proven experimentally that the structure of the wake generated when a fluid flows past a sphere is independent of the nature of the flow source for turbulent flows. No turbulence is produced at the centreline, although turbulence is transported across the centreline *via.* eddies (Versteeg and Malalasekera, 2007).

Turbulent flow occurs when the flow properties, namely the velocity and pressure, vary in a random and chaotic manner above a certain critical Reynolds number, Re_{crit}. Each of these fluctuating properties can be split into a steady mean value and a fluctuating component, which is also known as the Reynolds decomposition. This is described mathematically by equation (2.4).

$$\mathbf{v}(t) = \mathbf{V} + \mathbf{v}'(t) \tag{2.4}$$

The steady mean value is **V** and the fluctuating component is $\mathbf{v}'(t)$. Figure 2.2 shows

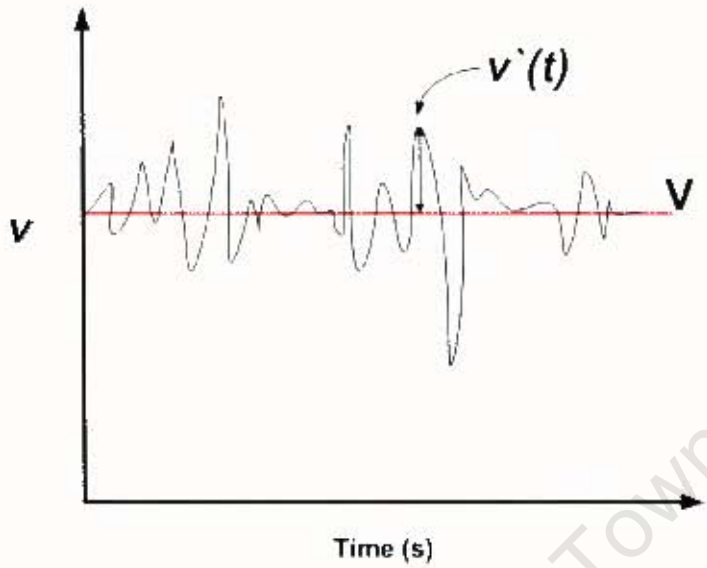

Figure 2.2: Plot showing the variables from equation (2.4). Here the velocity is denoted by **v**, the mean velocity by **V**, and the fluctuating component $\mathbf{v}'$.

a plot of velocity with time, indicating the fluctuating component and the steady mean value. The definition of the time average of the fluctuating velocity $\mathbf{v}'$ is given in equation (2.5).

$$\overline{\mathbf{v}'} - \frac{1}{\Delta t}\int_0^{\Delta t} \mathbf{v}'(t)\,\mathrm{d}t \tag{2.5}$$

The second moment of two fluctuating velocity components v_i' and v_j' is non-zero if the velocity components are dependent on one another. This is given in equation (2.6).

$$\overline{v_i'v_j'} = \frac{1}{\Delta t}\int_0^{\Delta t} v_i'v_j'\mathrm{d}t \tag{2.6}$$

Equations (2.4) to (2.6) will be used later on in the discussion.

When the flow variables **v** (velocity) and p (pressure) in the Navier-Stokes equations are replaced by the sum of the mean and fluctuating components (see eqns. (2.7), (2.8)) and the time average is taken, the Reynolds-averaged Navier-Stokes equations result (eqns. (2.9)-(2.12)). These are known as the density-weighted averaged equations for compressible flows (Anderson et al., 1984).

$$\mathbf{v} = \mathbf{V} + \mathbf{v}'; \quad v_x = V_x + {v_x}'; \quad v_y = V_y + {v_y}'; \quad v_z = V_z + {v_z}' \tag{2.7}$$

$$p = P + p' \tag{2.8}$$

$$\frac{\partial\left(\bar{\rho}\tilde{V}_x\right)}{\partial t} + div\left(\bar{\rho}\tilde{V}_x\tilde{\mathbf{V}}\right) = -\frac{\partial\tilde{p}}{\partial x} + div\left(\mu\ grad\ \tilde{V}_x\right) - \frac{\partial\left(\overline{\bar{\rho}{v_x}'^2}\right)}{\partial x} - \frac{\partial\left(\overline{\bar{\rho}{v_x}'{v_y}'}\right)}{\partial y} - \frac{\partial\left(\overline{\bar{\rho}{v_x}'{v_z}'}\right)}{\partial z} + S_x \tag{2.9}$$

$$\frac{\partial\left(\bar{\rho}\tilde{V}_y\right)}{\partial t} + div\left(\bar{\rho}\tilde{V}_y\tilde{\mathbf{V}}\right) = -\frac{\partial\tilde{p}}{\partial y} + div\left(\mu\ grad\ \tilde{V}_y\right) - \frac{\partial\left(\overline{\bar{\rho}{v_x}'{v_y}'}\right)}{\partial x} - \frac{\partial\left(\overline{\bar{\rho}{v_y}'^2}\right)}{\partial y} - \frac{\partial\left(\overline{\bar{\rho}{v_y}'{v_z}'}\right)}{\partial z} + S_y \tag{2.10}$$

$$\frac{\partial\left(\bar{\rho}\tilde{V}_z\right)}{\partial t} + div\left(\bar{\rho}\tilde{V}_z\tilde{\mathbf{V}}\right) = -\frac{\partial\tilde{p}}{\partial z} + div\left(\mu\ grad\ \tilde{V}_z\right) - \frac{\partial\left(\overline{\bar{\rho}{v_x}'{v_z}'}\right)}{\partial x} - \frac{\partial\left(\overline{\bar{\rho}{v_y}'{v_z}'}\right)}{\partial y} - \frac{\partial\left(\overline{\bar{\rho}{v_z}'^2}\right)}{\partial z} + S_z \tag{2.11}$$

$$\frac{\partial\bar{\rho}}{\partial t} + div\left(\bar{\rho}\tilde{\mathbf{V}}\right) = 0 \tag{2.12}$$

In equations (2.9) to (2.12), $\tilde{V}_i$ and $\tilde{\mathbf{V}}$ are the density-weighted averaged velocities and S_i is the source term in direction i. Note that equations (2.9) to (2.11) are identical to the momentum balance equations for the compressible Navier-Stokes equations, except that additional terms are present in each equation, which includes products of fluctuating velocities caused by turbulent eddies. These additional terms are also known as additional turbulent stresses or *Reynolds stresses* and are much greater than the viscous stress terms for fully turbulent flow. Figure 2.3 illustrates the mechanism through which these stresses develop, which is the exchange of momentum between the eddies and the fluid due to convective transport. The eddies cause the fluid layers in contact to accelerate or decelerate thus these layers experience additional turbulent shear stresses (Versteeg and Malalasekera, 2007).

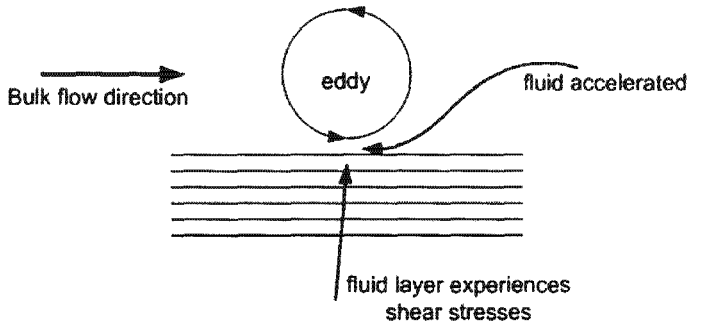

Figure 2.3: The mechanism through which turbulent eddies cause the surrounding fluid to experience turbulent shear stresses.

The numerical approaches available to simulate the effects of turbulence include solving the Reynolds-averaged Navier-Stokes (RANS) equations (Anderson et al., 1984), performing a Large Eddy Simulation (LES) (Smagorinsky, 1963) or performing a Direct Numerical Simulation (DNS). The LES tracks eddies at great computational cost. In the DNS, the mean flow and all turbulent velocity fluctuations are calculated on fine spacial grids using small time steps, also at an extremely high computational cost.

It is often the case that time-averaged properties of the flow are adequate for engineering purposes, and turbulent fluctuations may be neglected. The solution of the RANS equations is therefore often considered to be sufficient. In order to solve the RANS equations, turbulence models are needed to predict the Reynolds stresses, thus closing the system of equations (2.9) to (2.12). These are modelled using classical turbulence models such as the $k-\varepsilon$ (Launder and Spalding, 1974) and Reynolds stress models (Launder et al., 1975) at a moderate computational cost, which are used in many industrial Computational Fluid Dynamics (CFD) codes. Other models are required depending on the number of additional transport equations that must be solved, for example an energy balance.

In the $k-\varepsilon$ model, additional transport PDE's are solved together with the RANS equations for the turbulent kinetic energy k and for the rate of dissipation of turbulent kinetic energy ε, in the form eq. (2.13) and eq. (2.14), developed by (Launder and Spalding, 1974).

$$\frac{\partial(\rho k)}{\partial t} + div(\rho k \mathbf{V}) = div\left[\frac{\mu_t}{\sigma_k} grad\, k\right] + 2\mu_l S_{ij} \cdot S_{ij} - \rho\varepsilon \tag{2.13}$$

$$\frac{\partial(\rho \varepsilon)}{\partial t} + div(\rho \varepsilon \mathbf{V}) = div\left[\frac{\mu_t}{\sigma_k} grad\, \varepsilon\right] + C_{1\varepsilon}\frac{\varepsilon}{k} 2\mu_l S_{ij} \cdot S_{ij} - C_{2\varepsilon}\rho\frac{\varepsilon^2}{k} \tag{2.14}$$

In equation (2.13) the rate of change of k plus the transport of k by convection equals the transport of k by diffusion plus the rate of production of k minus the rate of destruction of k. Equation (2.14) is analogous to eq. (2.13). The rate of dissipation of turbulent kinetic energy per unit mass is denoted by ε, which is caused by the work done by the smallest eddies against viscous stresses. The last two terms in eq. (2.14) are production and destruction terms respectively, which are balanced with the last two terms in eq. (2.13) by the constants $C_{1\varepsilon}$ and $C_{2\varepsilon}$. This ensures that when k increases or decreases rapidly, then so does ε, which prevents unrealistic turbulence. Finally, the Reynolds stresses are linked to the turbulent kinetic energy by eq. (2.15) (Versteeg and Malalasekera, 2007).

$$-\rho\overline{v_i' v_j'} = \mu_t \left(\frac{\partial V_i}{\partial x_j} + \frac{\partial V_j}{\partial x_i} \right) - \frac{2}{3}\rho k \delta_{ij} \tag{2.15}$$

The parameter $\delta_{ij} = 1$ if $i = j$ and $\delta_{ij} = 0$ if $i \neq j$.

The $k-\varepsilon$ model was used by Schwarz and Turner (1988) in the modelling of a gas-stirred bath which led to results in good agreement with experimental data. In this case separate balance equations for the gas and liquid were used. The result is shown in Figure 2.4 which gives the vertical component of velocity for both the experimental data and the model results.

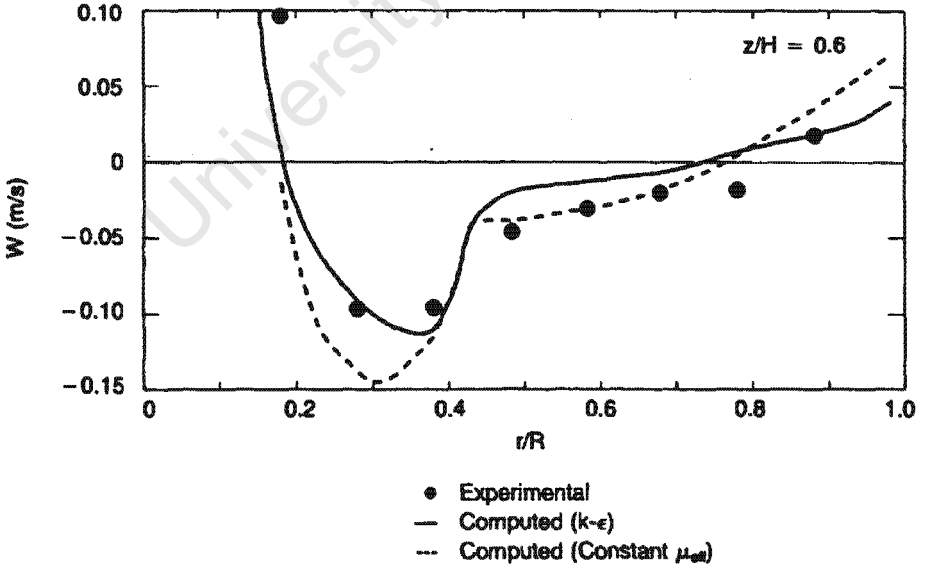

Figure 2.4: Experimental and calculated vertical velocities in the gas-stirred bath taken from Schwarz and Turner (1988).

The k–ε model is sufficient for many engineering applications and is well validated. How-

ever it does not accurately predict swirling flows and flows driven by Reynolds stresses which are directionally dependent (anisotropic). On the other hand, the Reynolds stress equation model (RSM) does account for these directional effects. The RSM model originally developed by Launder et al. (1975) is given in eq. (2.16), where $k = \frac{1}{2}\left(\overline{v_1{}'^2} + \overline{v_2{}'^2} + \overline{v_3{}'^2}\right)$.

$$\begin{aligned}\frac{\partial R_{ij}}{\partial t} + div\left(\rho\overline{v_i{}'v_j{}'}\mathbf{V}\right) = &-\left(R_{im}\frac{\partial V_j}{\partial x_m} + R_{jm}\frac{\partial V_i}{\partial x_m}\right) + div\left(\frac{\nu_t}{\sigma_k}grad\left(R_{ij}\right)\right)\\ &-\frac{2}{3}\varepsilon\delta_{ij} - 1.8\frac{\varepsilon}{k}\left(R_{ij} - \frac{2}{3}k\delta_{ij}\right)\\ &+0.6\left(\left(R_{im}\frac{\partial V_j}{\partial x_m} + R_{jm}\frac{\partial V_i}{\partial x_m}\right) + \frac{2}{3}p\delta_{ij}\right)\\ &-2\omega_k\left(\overline{v_j{}'v_m{}'}e_{ikm} + \overline{v_i{}'v_m{}'}e_{jkm}\right)\end{aligned} \tag{2.16}$$

Equation (2.14) from the $k-\varepsilon$ model is solved with eq. (2.16). The Reynolds stress is denoted by $R_{ij} = \overline{v_i'v_j'}$. The variable ω_k is a rotation vector and $e_{ijk} = 1$ if i, j and k are different and in cyclic order, $e_{ijk} = -1$ if i, j and k are different and in anti-cyclic order and $e_{ijk} = 0$ if any two of i, j or k are identical. Versteeg and Malalasekera (2007) mentioned suitable constants for eq. (2.16), based on commercial CFD codes, namely $\nu_t = 0.09\frac{k^2}{\varepsilon}$ and $\sigma_k = 1$. There are six independent Reynolds stresses and ε, and hence seven extra PDE's to be solved together with the RANS equations. This model is not validated as well as the $k-\varepsilon$ model and is not used much in industry due to the high computational cost and the numerical instability problems associated with the complex equations.

The use of the $k-\varepsilon$ model to account for liquid turbulence for single phase flow has been used by others in the field for the modelling of both uniformly and nonuniformly aerated bubble columns. Schwarz and Turner (1988) found that the use of the standard $k-\varepsilon$ model produced an experimentally valid result for a locally aerated bubble column, although most of the gas bubbles only rose through the middle of the reactor. However, Sokolichin and Eigenberger (1994) found that reasonably good results were obtained using laminar two-phase flow models. Due to inaccurate solutions being obtained if the step size was not sufficiently small, the time stepping was carried out by performing three integrations for each time step. These included two with half and one with the full step size, which resulted in a factor of 1.5 of the computational time. This procedure was more efficient than using a small but constant step size because the appropriate step size was always used. A relatively coarse computational mesh was chosen because the greater the number of mesh points, the smaller the time steps needed to accurately calculate variations in the local vortices.

In the large eddy simulation (LES) approach (Smagorinsky, 1963), the large eddies are computed with a time-dependent simulation, similar to the RSM approach, due to their interaction with the mean flow. The smaller eddies have a universal behaviour and can be computed with a more compact model. The method uses a filtering function to separate the eddies based on size.

Direct numerical simulation (DNS) uses the Navier-Stokes equations to solve for the velocities and pressure on a fine spacial mesh with very small time steps, to account for the fastest fluctuations. An advantage is that instantaneous results can be obtained that are not experimentally measurable so that advanced experimental techniques can be validated. The computational power required to perform 3-D calculations for turbulent flows is enormous, and the number of computational grid points has been proven to be approximately equal to $Re^{9/4}$ (Versteeg and Malalasekera, 2007).

2.2 Modelling a Single Bubble

The flow of a fluid around a bubble may be determined by the solution to the NVS equations. In addition, the flow field inside the bubble may also be modelled. This section will focus on the modelling approaches to solve for the flow field around a bubble and will also discuss some methods used to validate such flow fields.

It is known that bubbles and drops remain nearly spherical at Reynolds numbers below 500 (Clift et al., 1978), where Re=$\frac{\varrho DU}{\mu}$ and D is the diameter of the bubble, U is the free stream velocity of the continuous phase and ρ and μ is the density and viscosity of the continuous phase respectively. The free stream velocity U may also be defined as the relative velocity of the bubble in the continuous phase. Generally speaking, in the case where little internal circulation in a bubble or droplet is present, which generally occurs when $\kappa = \frac{\mu_d}{\mu}$ is high, where μ_d and μ are the viscosities of the dispersed and continuous phases respectively, the flow is similar to that around a solid sphere at the same Reynolds number (Juncu, 1999). If the flow around a solid sphere is to be modelled, a zero slip BC is applied to the surface, which means that a velocity of zero is prescribed everywhere on the surface (Cliffe and Lever, 1986).

In the case of a gas bubble rising in water, the value of κ is approximately zero and the solution of the Navier-Stokes equations gives accurate information regarding the flow of the continuous phase for Reynolds numbers less than 300 (Clift et al., 1978). When

modelling the flow both inside and around the bubble, the tangential fluid velocities and shear stresses of the continuous phase are set to equal those of the fluid inside the bubble, on the surface of the bubble (Juncu, 1999). In this case, the Navier-Stokes equations must be formulated for both phases, and each set of NVS equations are linked through the interface between the phases. The solution is easier to obtain when the viscosity of the dispersed phase differs greatly from the viscosity of the continuous phase.

In order to solve for the fluid flow around the bubble without modelling the flow inside the bubble a 'slip' boundary condition (BC) is applied to the bubble surface and the Navier-Stokes equations for the continuous phase are solved (Clift et al., 1978). This BC enforces zero shear stress tangential to the bubble surface, and the component of flow normal to the surface has a zero velocity, ie. mass cannot pass through the bubble/liquid interface. This means that the bubble acts as a void in the continuous phase. Hamielec et al. (1967) used this BC in solving for the flow around a fluid sphere of low viscosity and obtained results in good agreement with experimental data for Reynolds numbers between 50 and 200.

Analytical solutions are available for the flow around a spherical particle, but are meaningless for flows with Reynolds numbers that are greater than 1 (Clift et al., 1978). Boundary layer solutions for Re $>$ 50 are available which lead to analytic forms for the drag coefficient and Sherwood number. The Sherwood number is $\frac{kL}{D}$, where k is the mass transfer coefficient, L is a characteristic length and D is the mass diffusivity. The drag coefficient may be computed from the numerical solution for the flow field and compared to values available in literature. Numerical predictions of the drag coefficient for a bubble at various Reynolds numbers are available, which are in good agreement with experimental data (Clift et al., 1978). This framework for describing the flow field of the continuous phase is used in the next section for modelling the flow around multiple bubbles.

2.3 Modelling the Liquid and Bubbles

In determining the hydrodynamics of a bubble column, the movement of multiple bubbles and the flow of the continuous phase must be calculated. The modelling of multiple bubbles rising in a column requires techniques which take into account such phenomena. Hirt and Nichols (1981) stated that a multiphase flow problem can generally be solved by using either a Eulerian or a Lagrangian approach, where the computational mesh for the discrete phase in a Lagrangian problem moves as time is stepped forward, whilst for a problem formulated using the Eulerian method, the meshes for both the discrete and dispersed phases are fixed. In the bubble column modelling work performed by Delnoij (1998), a Lagrangian approach was implemented, where Newtonian equations of motion were used to determine the trajectory of the bubble. If the dispersed and discrete phases are treated separately, ie. equations for mass, energy and momentum are formulated for each phase, and the exchange of these properties is linked through the interface between the phases, then this is referred to as an Euler-Euler approach. On the other hand, the Euler-Lagrangian approach models the continuous phase in the same manner as the Euler-Euler approach, but the motion of the discrete phase is governed by Newtonian equations of motion.

2.3.1 The Volume of Fluid Method

Hirt and Nichols (1981) developed the Volume of Fluid (VOF) method which can be used to track free boundaries such as the interface of a bubble moving in a liquid. This approach was designed for Eulerian problems where free boundaries are deformed significantly, to the extent that Lagrangian methods can not be used. In the VOF method, a function $F(\mathbf{x}, t)$ is defined which represents the fractional volume of a computational cell occupied by liquid. Thus a unit value of F implies that the cell contains only liquid whereas a zero value of F implies that the cell contains only gas. Cells with values between zero and unity then contain an interface. Equation (2.17) gives the time dependence of F as it moves through the fluid.

$$\frac{\partial F}{\partial t} + (\mathbf{u} \cdot \nabla) F = 0 \tag{2.17}$$

In this method, both the gas and liquid are treated as a pseudo-homogeneous phase and a single set of balance equations describes both phases. At each time step, the algorithm first calculates the flow field by solving the Navier-Stokes equations, then updates the value of F for each cell by solving equation (2.17). A cell interface is reconstructed with a straight line that is either parallel to the cell wall (Hirt and Nichols, 1981) or sloped, by

using the values of F of the surrounding cells. The position of the line inside the cell is such that the volume fraction of liquid is equal to F, and boundary conditions are imposed on the interface.

Delnoij (1998) studied the fluid dynamics of gas-liquid bubble columns, and used the VOF model to predict the time-dependent behaviour of a few (< 10) gas bubbles rising in an initially quiescent liquid. This model incorporated a reconstruction algorithm developed by Rudman (1997), which used straight lines in any orientation to reconstruct the interface. The VOF model was able to predict the motion of a deforming gas bubble in the bubble column. The simulations included the formation and rise of a skirted and spherical cap bubble, the coalescence of two identical gas bubbles and the flow of two bubbles rising from adjacent orifices.

2.3.2 The Euler-Lagrangian Method

In this method, the flow of the continuous phase is calculated using the volume-averaged Navier-Stokes equations. The continuous phase is treated as a quasi-homogeneous gas-liquid phase. At each new time step, the relevant forces on the bubble are calculated, the trajectory and motion of the bubble is determined, and the flow of the liquid phase around the bubbles is calculated from the NVS equations. The exchange of momentum between the gas and the liquid phase is accounted for by a source term in the NVS equations (Delnoij, 1998). The advantage of using a Euler-Lagrangian approach in modelling the hydrodynamics of a bubble column is that forces on individual bubbles resulting from bubble-bubble interaction may be included. In addition, bubble coalescence and breakup, as well as chemical reaction may also be incorporated into the model (Sokolichin and Eigenberger, 1994). The Euler-Lagrangian method was implemented by Delnoij (1998), who calculated the overall force on the particle (bubble) as that shown in equation (2.18).

$$\mathbf{F}_{total} = \mathbf{F}_P + \mathbf{F}_D + \mathbf{F}_{VM} + \mathbf{F}_L + \mathbf{F}_{Hydro} + \mathbf{F}_G \tag{2.18}$$

The total force comprises of the sum of contributions from pressure gradient $\mathbf{F}_P$, drag $\mathbf{F}_D$, virtual mass $\mathbf{F}_{VM}$, vorticity $\mathbf{F}_L$, interaction between bubbles $\mathbf{F}_{Hydro}$ and gravity $\mathbf{F}_G$. This total force is calculated using Newtons second law in equation (2.19).

$$m_b \frac{d\mathbf{v}}{dt} = \mathbf{F}_{total} \tag{2.19}$$

Equation (2.20) gives the new bubble velocity after each time step Δt, where n denotes

the current time and *n+1* denotes the current time plus Δt.

$$\mathbf{v}^{n+1} = \mathbf{v}^n + \left(\frac{d\mathbf{v}}{dt}\right)^n \Delta t \tag{2.20}$$

Thus the bubble positions can be obtained from the velocity and the position from the previous time step.

All the individual forces that constitute $\mathbf{F}_{total}$ are given in equations (2.21) to (2.28) below.

Eq. (2.21) gives the force due to the pressure gradient.

$$\mathbf{F}_P = -V_b \nabla P \tag{2.21}$$

Eq. (2.22) is the drag force given by Odar and Hamilton (1964).

$$\mathbf{F}_D = -\frac{1}{2} C_D \rho_l \pi {R_b}^2 |\mathbf{v} - \mathbf{u}| (\mathbf{v} - \mathbf{u}) \tag{2.22}$$

The drag coefficient C_D is a function of the flow regime and can be approximated from a standard drag curve. The bubble velocity is $\mathbf{v}$ and the liquid velocity is $\mathbf{u}$.

The virtual mass force is due to liquid close to the bubble that is accelerated when the bubble accelerates, which causes the bubble to resist accelerating and is given in eq. (2.23).

$$\mathbf{F}_{VM} = -\left(\frac{D\mathbf{I}}{Dt} + \mathbf{I} \cdot \nabla \mathbf{u}\right) \tag{2.23}$$

$$\mathbf{I} = C_{VM} \rho_l V_b (\mathbf{v} - \mathbf{u}) \tag{2.24}$$

A bubble rising in a liquid experiences a lift force due to vorticity or shear, which acts towards the region of lower liquid velocity if the velocity of the bubble exceeds that of the liquid, and towards the region of higher liquid velocity if the bubble velocity is less than that of the liquid. The lift force can be described by eq. (2.25).

$$\mathbf{F}_L = -C_L \rho_l V_b (\mathbf{v} - \mathbf{u}) \times \Omega \tag{2.25}$$

$$\Omega = \nabla \times \mathbf{u} \tag{2.26}$$

The hydrodynamic force $\mathbf{F}_{Hydro}$ modelled the additional velocity disturbance induced by neighbouring bubbles on the virtual mass force and is given in eq. (2.27).

$$\mathbf{F}_{Hydro} \approx 3 \cdot C_{VM} \rho_l V_b (\mathbf{v} - \mathbf{u}) \cdot \nabla \mathbf{u}_{induced} \tag{2.27}$$

Finally the force due to gravity is given in eq. (2.28).

$$\mathbf{F}_G = \rho_g V_b \mathbf{g} \tag{2.28}$$

Delnoij (1998) used an Euler-Lagrange discrete bubble model to simulate the flow of small, spherical gas bubbles in a 2D column operating in the homogeneous regime. This included a collision model developed by Hoomans et al. (1996) who modelled the forces due to the interactions between bubbles. This Euler-Lagrange model was validated by experimental results obtained in literature.

2.3.3 The Euler-Euler Method

An Euler-Euler model was used by Sokolichin and Eigenberger (1994), which treated the gas phase as a pseudo-continuum and the mass and momentum equations were formulated for both phases and solved simultaneously. This meant that each volume element in the space contained a fraction ε of the dispersed phase. The momentum equations for the gas and liquid phases were coupled using an interaction force term. The continuity equations for the liquid and the gas are of the form shown in eq. (2.29).

$$\frac{\partial (\varepsilon_k \rho_k)}{\partial t} + \nabla \cdot (\varepsilon_k \rho_k \mathbf{u}_k) = 0, \qquad k = l, g \tag{2.29}$$

Similarly, eq. (2.30) gives the momentum balances for both phases.

$$\begin{aligned} &\frac{\partial (\varepsilon_k \rho_k \mathbf{u}_k)}{\partial t} + \nabla \cdot (\varepsilon_k \rho_k \mathbf{u}_k \mathbf{u}_k) \\ &= \varepsilon_k \nabla \cdot \mu_k \left(\nabla \mathbf{u}_k + \nabla \mathbf{u}_k^t \right) - \varepsilon_k \nabla p + \varepsilon_k \rho_k \mathbf{g} \pm \mathbf{F}_W, \qquad k = l, g \end{aligned} \tag{2.30}$$

Here l denotes the liquid phase and g the gas phase. Equations need to be developed for each set of bubbles with different masses. These mass and momentum balances are analogous to those described by equations (2.1) and (2.2). The main difference is that

the fraction ε is included in each term in the overall balance, which describes the fraction of the dispersed phase or continuous phase in a given computational cell.

The interaction force term includes forces due to friction, added mass and lift. The friction force (eq. (2.31)) is the most dominant of the three forces.

$$\mathbf{F}_s = -\varepsilon_g C_w \left(\mathbf{u}_g - \mathbf{u}_l\right) \tag{2.31}$$

Here C_w is the friction coefficient and although correlations for it exist, the value of $5 \times 10^4 \frac{kg}{m^3 s}$ is a good approximation according to Schwarz and Turner (1988). This force describes the interaction between the liquid and the bubble under non-accelerating conditions only. When the bubble accelerates relative to the liquid, it causes the liquid close to it to accelerate. This extra force of acceleration is known as the added mass force, given in eq. (2.32).

$$\mathbf{F}_a = -\varepsilon_g C_a \rho_l \frac{D\left(\mathbf{u}_g - \mathbf{u}_l\right)}{Dt} \tag{2.32}$$

The volume fraction of liquid which is accelerated with the bubble is C_a. Cook and Harlow (1986) claimed that a value for C_a of 0.25 is sufficient for gas bubbles. The final force is the lift force, also known as the magnus force which arises when the bubble rotates. This force is exerted perpendicular to the main flow direction.

2.3.4 Comparison Between Euler-Euler and Euler-Lagrangian Two-fluid Models

In the study by Sokolichin and Eigenberger (1994), it was mentioned that both the Euler-Euler and Euler-Lagrangian approaches should give the same result. The advantage of the Euler-Lagrangian model is that each bubble is modelled individually, so that interactions between the bubbles themselves and the bubbles and the liquid can be incorporated into the model. Such effects include mass transfer and chemical reaction. Webb et al. (1992) stated that the Lagrangian approach approximates convection without difficulties and particles of different sizes can be modelled. The disadvantage for dynamic problems is that the tracking of the bubbles involves storing the position of each bubble at each time step, and the solution of the equations of motion for many bubbles becomes too computationally expensive for larger columns. The Euler-Euler approach however, does not require increasing computational power for an increasing number of bubbles, but rather for an increasing number of volume elements in the computational mesh. An increase in the number of different bubble sizes requires an increase of gas phase balance equations,

which increases the computational load. Numerical techniques for solving the coupled balance equations have been developed. These features of the Euler-Euler formulation make it easer to use than the Euler-Lagrange method (Sokolichin and Eigenberger, 1994).

2.3.5 Comparison Between Steady-state and Dynamic Models

In the modelling and simulation of a bubble column, the hydrodynamics may be steady or dynamic. In this section the advantages of using either steady-state or dynamic models for the simulation of a bubble column are studied, which illustrate the importance of choosing a particular model under certain operating conditions.

In flat bubble columns, a two-dimensional flow structure develops (Becker et al., 1994). The experimental validation of a two-dimensional model can be performed using a wafer-shaped or flat bubble column. Anemometers are used to measure the bubble or liquid velocities in the column. These probe measurements only produce reproducible data when the signals are averaged (Lapin and Lubbert, 1994).

Sokolichin and Eigenberger (1994) studied the differences between steady state and dynamic modelling for various reactors. For a locally aerated flat bubble column with a sparger in the left corner and a superficial gas velocity exceeding $3.3\,mm/s$, a steady circulating flow structure was observed, which was also obtained using a numerical simulation. This is shown in Figure 2.5, where a large vortex which describes the swirling motion of a fluid around a center, occupied most of the column, with the bubble swarm on the left hand side of the column. A small vortex was present in the top left corner which directed the upwardly flowing bubbles back down towards the center. The liquid flowed with the bubble swarm and down along the walls. This was replaced by three smaller vortices when the gas velocity dropped below $3.3\,mm/s$. The centers of these vortices also shifted up and down. This was validated by experimental results by Becker et al. (1994), where a superficial gas velocity of $0.66\,mm/s$ was used. A laminar flow model and a coarse grid simulated a steady solution, which was validated experimentally by time-averaging the Laser Doppler Anemometer (LDA) measurements. When the computational grid was refined, the solution became transient, which reproduced the observed oscillations of the bubble swarm. This is shown in Figures 2.6 and 2.7. When the instantaneous velocity fields were time-averaged, the result matched with the steady state solution obtained with the coarse grid. Thus it was shown that the flow may change from steady to dynamic depending on the superficial gas velocity. The hydrodynamics inside the column may be dynamic but a steady-state model could be used and validated against time-averaged experimental data.

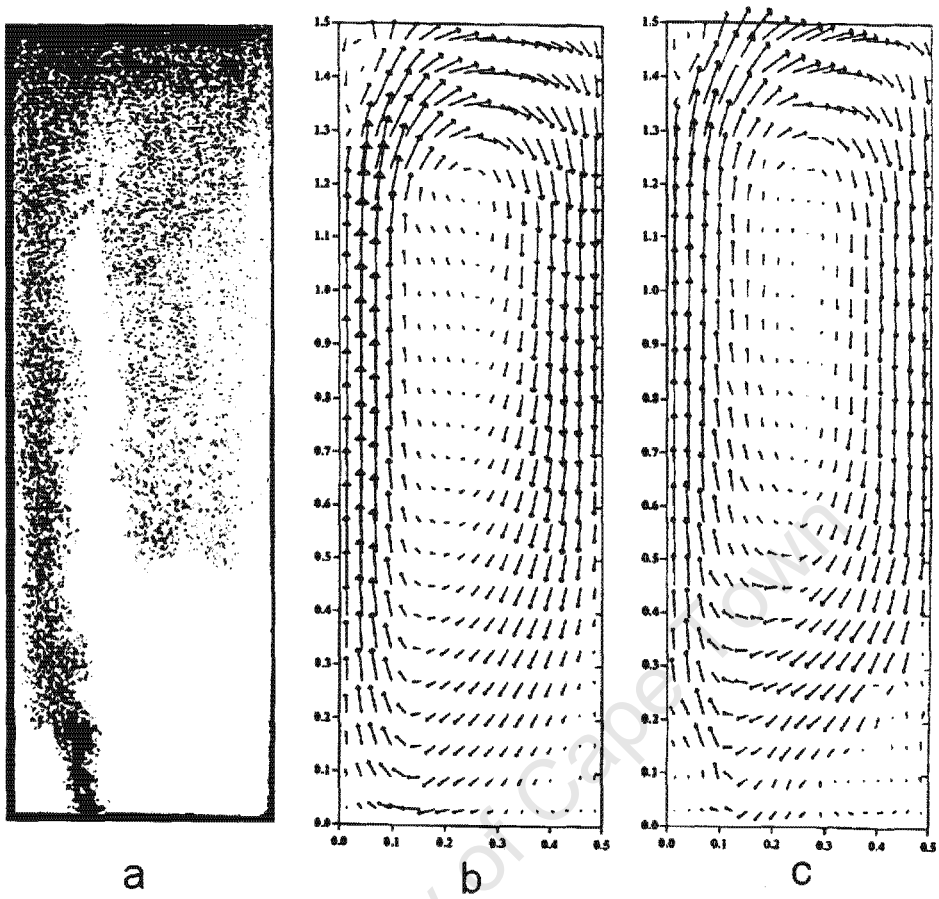

Figure 2.5: Partially aerated flat bubble column ($U_G = 3.3\,mm/s$): (a) photograph; (b) calculated and (c) measured liquid velocity field (Becker et al., 1994).

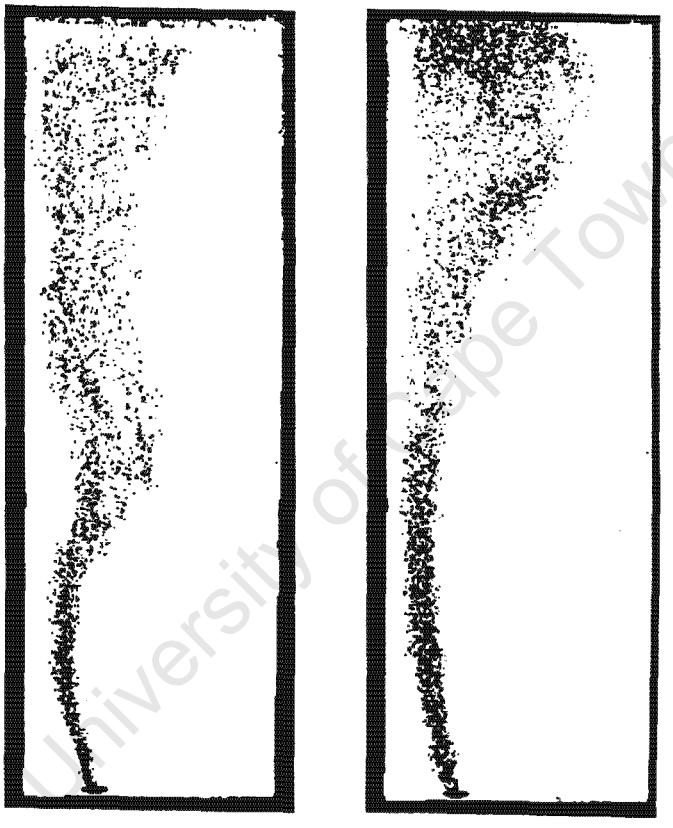

Figure 2.6: Partially aerated flat bubble column ($U_G = 0.66\,mm/s$): photographs of the oscillating bubble swarm at two different times (Becker et al., 1994).

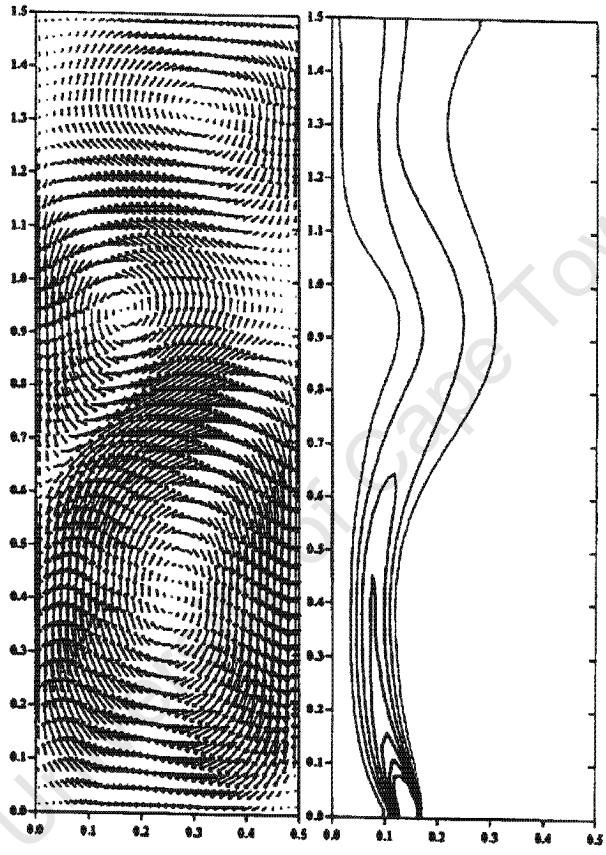

Figure 2.7: Dynamic simulations of a partially aerated flat bubble column ($U_G = 0.66\,mm/s$): instantaneous results of (a) liquid velocity field and (b) gas hold-up (Becker et al., 1994).

For uniformly aerated bubble columns, the gas is introduced over the entire bottom of the column. At low superficial gas velocities, the homogeneous regime is apparent. At higher gas velocities, liquid vortices form at the sparger and move up along the walls of the column. Torvic and Svendsen (1990) found large gas hold-up with liquid upflow in the column center and liquid downflow near the walls. The problem with the steady state Euler-Lagrange and Euler-Euler two-fluid models is that if the friction force is the only coupling force term, and the grid is too coarse, then the solution represents the homogeneous regime, with little liquid movement. The mechanism which draws the bubbles to the column center was found to use the Magnus force with opposite sign (Torvic and Svendsen, 1990).

In the work performed by Sokolichin and Eigenberger (1994), an Euler-Euler model was used to simulate a flat two-dimensional bubble column. Above a superficial gas velocity of approximately $2\,cm/s$, the flow structure was unsteady. Vortices were generated near the sparger and moved upwards along the column walls. The local velocities and gas hold-ups were averaged over a substantial length of time, and that result matched well with the measured data which was also time-averaged. However time-averaged flow patterns cannot be obtained from steady state models because long time integrals over flow functions do not vanish, but lead to additional terms, which are difficult to approximate. Dynamic models are necessary to predict steady as well as transient flows due to the numerical difficulty associated with the convergence of the steady state solution. The disadvantage of solving dynamic equations is that more complex mathematical techniques are required. The numerical load is a function of the number of different terms in the modelling equations and the convergence rate of the iteration loops, which depends on the number and complexity of the coupling terms itself (Sokolichin and Eigenberger, 1994).

The hydrodynamics of a bubble column may be steady or dynamic, depending on the operating conditions of the column and the position of the gas sparger. Generally speaking, a dynamic model is more computationally expensive to use compared to a steady-state model, but is often necessary to accurately simulate the flow behaviour in a bubble column.

2.3.6 Modelling Bubble Clusters

The need for a more efficient approach to predict the hydrodynamics in bubble columns becomes apparent when the modelling of a pilot plant bubble column is considered. In this case, an order of 2 million bubbles would need to be followed. In most bubble columns used in industry, bubbles tend to move in clusters, which means that bubbles do not move

independently from each other, but rather that adjacent bubbles have a similar motion. Bubble clusters are characterised by a position in space, a size and a bubble size (Lapin and Lubbert, 1994). The approach taken by Lapin and Lubbert (1994) was to break the model up into different scales. On the macroscale, the gas-liquid system was considered as a quasi-single-phase fluid. The bubble motion determined the local density of the two-phase gas-liquid medium. The inhomogeneities in density lead to buoyancy effects, which drives convective flows. The bubble paths are dependent on the local motion of the liquid phase and the slip velocity of the bubbles. However, on the small scale, the dynamics of the bubble wake determine the relative motion of the bubble and the local mixing effects.

The clusters were modelled using spacial density functions. The macroscale model used the standard Navier-Stokes equations. The Eulerian model was based on the balance equation on the bubble distribution density function W, which describes the number of bubbles within a given volume in the reactor. This function varies with position in the reactor and bubble mass and is given by equation (2.33).

$$\frac{\partial W}{\partial t} + div\left(\mathbf{u}_b, W\right) + \frac{\partial}{\partial m}\left(\frac{dm}{dt}W\right) = div\left(a_{eff} grad W\right) + \frac{\partial}{\partial m}\left(a_d \frac{\partial W}{\partial m}\right) \tag{2.33}$$

The first term in the equation is the total change of W with time, the next the flow of bubbles across the boundaries of the control volume and the third the change of mass due to mass transfer to the bulk fluid. The variable $\mathbf{u}_b$ is the absolute bubble velocity. The terms on the right-hand side represent diffusion where a_{eff} and a_d are coalescence and dispersion coefficients respectively. The density of the volume element is a function of the temperature T, and W. In the work performed by Lapin and Lubbert (1994) a 2-D bubble column was simulated. The height of the column was $1.5\,m$ and the width $1\,m$. Equation (2.33) was solved using a computationally fine grid, due to the numerical (false) diffusion problems which arose when the grid was too coarse. The results obtained from this model indicated that numerical diffusion dominated and it was concluded that two-fluid Eulerian simulations are sensitive to false diffusion.

The Lagrangian medium scale model calculated the bubble paths. Equation (2.34) gives the bubble trajectory.

$$\frac{d\mathbf{r}_k}{dt} = \mathbf{u}_b\left(D_k, \mathbf{u}, \nabla p\right) \tag{2.34}$$

Here $\mathbf{u}_b$ is the absolute velocity of the bubble, which depends on the liquid flow velocity

$\mathbf{u}_l$, the slip velocity $\mathbf{u}_{slip}$(velocity of the bubble relative to the liquid flow) and the velocity fluctuation $\mathbf{u}_{ran}$, which takes into account random path fluctuations such as vortex shedding. The absolute velocity of the bubble is given by eq. (2.35).

$$\mathbf{u}_b = \mathbf{u} + \mathbf{u}_{slip} + \mathbf{u}_{ran} \tag{2.35}$$

The local density of the two-phase fluid is a function of the number of bubbles in that region. Probability density functions were used to describe the number of bubbles of a certain size class per unit volume. These were bell shaped curves. The algorithm involved solving for the local velocity field, then used that field to calculate the new positions of the bubbles. The density of the two-fluid was then calculated and the process was repeated until convergence was obtained. The advantage of this method was that numerical diffusion was negligible (Lapin and Lubbert, 1994).

2.3.7 Turbulence Modelling for Systems Containing a Dispersed Phase

Before the 1970s, it was not possible to take direct measurements of turbulence in the presence of particles. This is because hot-wire anemometry was the only method available and hot-wire probes could not be used in flows with solid particles. However, laser Doppler anemometry (LDA) can be used now to measure both instantaneous and time-averaged velocities with high spatial resolution for the continuous and dispersed phases in a two-phase flow. This technique makes use of the *Doppler effect*, which relates the interaction of sound or light waves with a moving observer to the source of the waves. Turbulence is generally decreased by the presence of small particles in the continuous phase, and increased by larger particles. The basic approach modifies the generation and dissipation terms in the $k - \varepsilon$ equations to account for the dispersed phase. An approach to model the effect of particles on the dispersed phase turbulence, which does not require Reynolds stress modelling or empirical closure models is to use direct numerical simulation (DNS). The intrinsic turbulence energy is the energy of the continuous phase without particles and can increase or decrease due to particle motion. Averaging techniques including time averaging and volume averaging are used to model turbulence due to the difficulty in modelling local details. Large eddy simulations (LES) are used to model turbulent flow at high Reynolds numbers whilst maintaining relatively good accuracy. This method uses both direct simulation and Reynolds-averaging approaches. Another method known as the eddy life time model, originally developed by Yuu et al. (1978), involved considering the turbulent flow as a collection of turbulent eddies with discrete velocities and life times (Crowe et al., 1998).

2.4 Numerical Methods

2.4.1 The Finite Difference Method

A finite difference method has always been popular to solve fluid mechanics based equations of motion (Zienkiewicz and Taylor, 2000). A fully discrete finite difference method discretizes all the independent variables. For a given PDE, all the derivatives are replaced by finite difference approximations. This means that a system of algebraic equations is set up for the unknowns at the mesh points. The solution is obtained by stepping forward in time and space, starting with the initial values at a domain boundary (Heath, 2002).

2.4.2 The Finite Volume Method

The finite volume method is a subclass of the finite difference method (Zienkiewicz and Taylor, 2000). The first step in the finite volume method is the division of the spatial domain into a number of smaller subdomains or control volumes. Figure 2.8 illustrates a general 1-D domain, which consists of smaller control volumes including central nodal points, which coincide with the domain boundaries.

For the steady state diffusion of a property ϕ in a 1-D domain, the governing PDE is eq. (2.36).

$$\frac{\mathrm{d}}{\mathrm{d}x}\left(\Gamma\frac{\mathrm{d}\phi}{\mathrm{d}x}\right) + S = 0 \tag{2.36}$$

In this example Γ is the diffusion coefficient and S is the source term. The PDE is integrated over the control volume which gives a discretized equation of the form eq. (2.37) at the nodal point P.

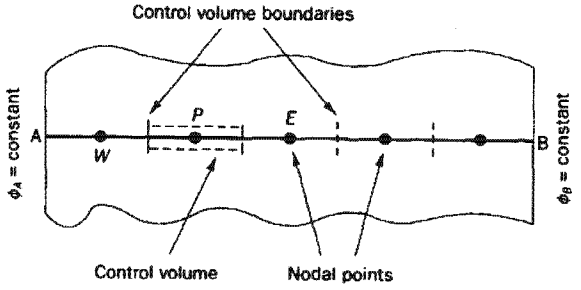

Figure 2.8: Diagram representing the discretization of the space for a 1-D problem (Versteeg and Malalasekera, 2007).

$$\int_{\Delta V} \frac{\mathrm{d}}{\mathrm{d}x}\left(\Gamma\frac{\mathrm{d}\phi}{\mathrm{d}x}\right)\mathrm{d}V + \int_{\Delta V} S\mathrm{d}V = \left(\Gamma A\frac{\mathrm{d}\phi}{\mathrm{d}x}\right)_e - \left(\Gamma A\frac{\mathrm{d}\phi}{\mathrm{d}x}\right)_w + \overline{S}\Delta V = 0 \tag{2.37}$$

In equation (2.37) A is the cross sectional area of the control volume face and ΔV is the control volume. When a linear interpolation method is used between nodes, eq. (2.38) gives the values for Γ.

$$\Gamma_w = \frac{\Gamma_W + \Gamma_P}{2} \qquad \Gamma_e = \frac{\Gamma_P + \Gamma_E}{2} \tag{2.38}$$

Equations (2.39) and (2.40) give the diffusive flux terms.

$$\left(\Gamma A\frac{\mathrm{d}\phi}{\mathrm{d}x}\right)_e = \Gamma_e A_e\left(\frac{\phi_E - \phi_P}{\delta x_{PE}}\right) \tag{2.39}$$

$$\left(\Gamma A\frac{\mathrm{d}\phi}{\mathrm{d}x}\right)_w = \Gamma_w A_w\left(\frac{\phi_P - \phi_W}{\delta x_{WP}}\right) \tag{2.40}$$

Substitution of equations (2.38) to (2.40) into equation (2.37) yields a linear algebraic equation with ϕ_P, ϕ_W and ϕ_E unknown. Similar equations are set up at all the nodal points, which results in a linear system of algebraic equations, and boundary conditions are applied. The solution of this system is the values of ϕ at all the nodal points. The same principles are applied for 2-D and 3-D domains (Versteeg and Malalasekera, 2007).

2.4.3 The Finite Element Method

The finite element method (FEM) solves for the continuous solution in the space using a discrete number of points, which are interconnected and result in a system of simultaneous algebraic equations. The space is discretized by dividing it into a number of finite elements, each interconnected to nodes common to two or more elements or boundary lines or surfaces. In 2-D problems the domain may constructed using either triangles, quadrilaterals or a combination of both types of elements. In 3-D the domain may constructed using either tetrahedra, hexahedra or a combination of both. This provides a suitable framework to model domains with curved boundaries. Instead of solving for the entire solution in one operation, equations for each finite element are constructed and combined to obtain an overall solution. This discrete model composes of a set of piecewise-continuous functions defined within each finite domain or finite element. The boundary conditions, which are invoked after construction of the global system of equations, can be the value

of the function itself (Diriclet BC), the value of its derivative (Neumann BC) or a linear combination of these two (Robin BC). A linear solver is used to solve the system of equations (Belytschko and Fish, 2006). Figure 2.9 illustrates the discretization of the domain.

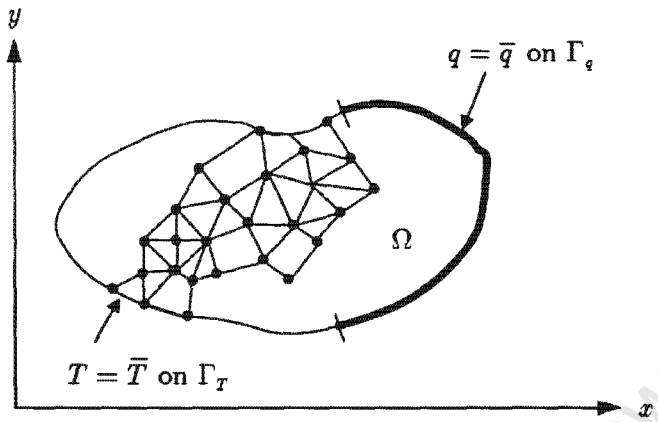

Figure 2.9: Mesh for a 2-D domain using a combination of triangular and quadrilateral elements (Belytschko and Fish, 2006).

In order to illustrate how the finite element method works an example from Belytschko and Fish (2006) is shown below. Equation (2.41) describes heat conduction in one dimension. Boundary conditions for the heat flux at $x = 0$ and temperature at $x = L$ are described by eq. (2.42) and eq. (2.43) respectively. These equations represent the strong form of the problem. Here A is the cross sectional area, k the heat transfer coefficient, T the temperature, s the heat source and q the heat flux for the problem.

$$Ak\frac{d^2T}{dx^2} + s = 0 \qquad 0 < x < L \tag{2.41}$$

$$q = \bar{q} = -k\frac{dT}{dx} \quad on \quad \Gamma_q \tag{2.42}$$

$$T = \overline{T} \quad on \quad \Gamma_T \tag{2.43}$$

The weak form of the problem is then developed by multiplying each eq. (2.41) and eq. (2.42) by the arbitrary weight function $w(x)$ and integrating over the domain Ω for eq. (2.41) and Γ_q for eq. (2.42). This yields eq. (2.44) and eq. (2.45) respectively.

$$\int_\Omega w\frac{d}{dx}\left(Ak\frac{dT}{dx}\right)dx + \int_\Omega wsdx = 0 \quad \forall w \tag{2.44}$$

$$\left(wA\left(qn-\bar{q}\right)\right)|_{\Gamma_q}=0 \quad \forall w \tag{2.45}$$

Integration by parts is performed on the first term in eq. (2.44) to give eq. (2.46).

$$\int_\Omega \frac{dw}{dx}Ak\frac{dT}{dx}dx=\left(wAk\frac{dT}{dx}n\right)|_\Gamma+\int_\Omega wsdx \quad \forall w \quad \textit{such that } w=0 \textit{ on } \Gamma_T \tag{2.46}$$

As $w=0$ on Γ_T, eq. (2.46) may be combined with eq. (2.45) to give the weak form, eq. (2.47).

Find $T(x)\in U$ such that

$$\int_\Omega \frac{dw}{dx}Ak\frac{dT}{dx}dx=-\left(wA\bar{q}\right)|_{\Gamma_q}+\int_\Omega wsdx \quad \forall w\in U_0 \tag{2.47}$$

Here U and U_0 are the set of suitable trial functions and weight functions respectively. $T(x)$ and $w(x)$ are constructed as a linear combination of shape functions. For example, $T(x)=T_1N_1(x)+T_2N_2(x)+T_3N_3(x)$, for a mesh containing 3 nodes. The shape functions, N_i may be linear, quadratic or of a higher order. In eq. (2.47), the integral over the entire domain may be replaced by the sum of the integrals over the element domains. The integrals may then be approximated using gauss quadrature to form a system of matrix equations, with $T(x)$ and $w(x)$ approximated by the shape functions. The solution to this system of matrix equations is the vector of temperatures across the domain.

For Stokes flow, the weak form poses a symmetric saddle point problem. A solution only exists if the function spaces in which a solution is searched for satisfies certain conditions. In this case it is the LBB (Ladyzhenskaya-Brezzi) condition. When the continuous function spaces, which satisfy such conditions, are discretized by replacing the continuous variables and test functions by finite element functions, then these also have to satisfy the LBB condition (Bangerth et al., 2007).

The advantages of the finite element method are that it can model irregularly shaped domains, it can handle various types of boundary conditions, the size of the elements can be varied so that small elements can be used in conjunction with larger elements and that it can handle non-linear behaviour. This method provides approximations which are superior or at least equal to the results provided by finite difference methods (Logan, 2002). However Zienkiewicz and Taylor (2000) mentioned that conservation equations are only satisfied within a region of a few elements, whereas in the finite volume method, local conservation equations are satisfied within individual elements.

2.5 Summary

It was found that the hydrodynamic modelling of bubble columns presents multiple challenges, predominantly in the large amounts of computational power required to simulate even small, lab-scale columns. As the computational expense generally increases with the size and number of bubbles in the column, the accurate modelling of pilot plant and industrial sized columns becomes impracticable. Various modelling approaches have been discussed which differ mainly in the governing equations used to describe the two-phase flow. In addition, phenomena including turbulence, heat transfer and chemical reaction need to be incorporated into the modelling framework.

Chapter 3

Thesis Objectives

The previous models described in the literature were formulated to predict the flow behaviour of gas and liquid in a bubble column. Although formulation of these models is well-established, their simulation in multiphase flows is computationally expensive. Accurate simulation of large bubble columns therefore offers significant numerical challenges.

The solution to the Navier-Stokes equations for a single phase problem is already computationally expensive, and the addition of another phase typically means that multiple moving boundaries need to be included in the solution algorithm, which corresponds to an order of magnitude increase in the computational load. Generally speaking, the computational power required to solve the governing equations for a bubble column increases with the number of bubbles in the column. Apart from the numerical challenges associated with columns containing large numbers of bubbles, as mentioned in Chapter 2, complex phenomena including turbulence, bubble coalescence and breakup, bubble-wall interaction, heat transfer and possibly chemical reaction need to be considered in the model. In addition, the modelling of systems containing more than two phases, eg. slurry reactors, pose even more challenges due to their complexity. Thus a fundamentally new approach that solves these systems with less computational effort is needed to better predict the hydrodynamics of bubble columns.

To investigate the computational expense of modelling multiphase systems, the flow of water around a single rigid, spherical gas bubble is modelled. Both the Stokes and the Navier-Stokes equations are used to describe the velocity and pressure fields of the water around the bubble. Figure 3.1 illustrates the basic concept.

In an attempt to reduce the computational expense in solving the bubble column reactor, this study proposes a "cell" model, which predicts the velocity vector field in the vicinity

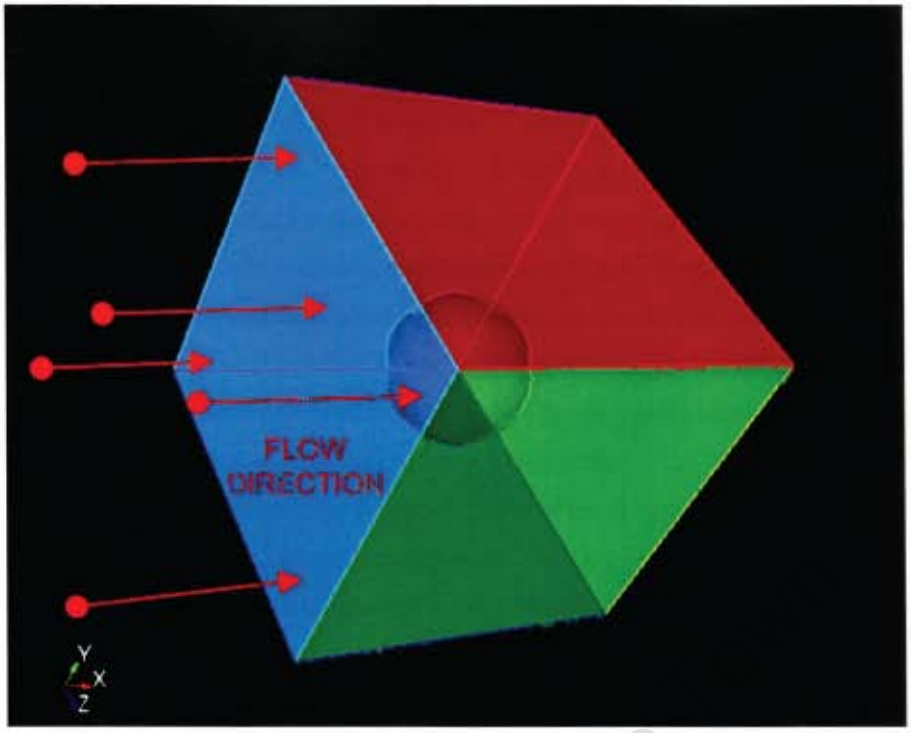

Figure 3.1: Illustration of the 3-D domain for the single bubble model. Simulation results are not shown.

of a single bubble. This model can then be incorporated as the fundamental building block of a larger framework, such as a population balance, in order to predict the flow of multiple bubbles on the bubble column scale. Additional phenomena such as bubble deformation or heat and mass transfer could be dealt with in the single cell model, whilst the column-scale model accounts for the interactions between the smaller cell models by way of the continuum phase (the liquid, in the case of bubble columns).

This MSc study focusses on the cell model, in particular, an analysis of the Reynolds number domain in which the Stokes equations, which are easier to solve than the Navier-Stokes equations due to their being linear, can be used to accurately predict the flow around the bubble. Thus flows modelled with the Stokes equations are less computationally expensive to solve. The value of the Stokes simulation may be summarised as follows. In the case where the entire bubble column is simulated, the simulation domain may be partitioned into two zones, i) where the local Reynolds number is low enough for application of Stokes flow, and ii) where the flow is non-linear, making the Navier-Stokes, or models that can simulate turbulence, essential. This study therefore focusses on establishing the accuracy of the Stokes equations as a function of the Reynolds number. The performance of the Stokes simulation as reflected by the computation time involved is reported. The intended application is then in decreasing computational expense by par-

titioning the solution domain into two types of region, namely Stokes and Navier-Stokes regimes.

In order to understand how the sub-model developed in this study fits into a larger scale model, it should be mentioned that this study was performed in conjunction with two other students at the University of Cape Town in the Department of Chemical Engineering. Waldo Coetzee, a PhD. student, calculated the trajectory of a bubble moving in a liquid with time by performing a force balance on the bubble, then used the net force to calculate the acceleration of the bubble. In the case that the bubble is moving at terminal velocity, a quasi-steady state may be assumed. At a given time, the velocity vector field around the bubble may be used to determine the *Re*. If the *Re* is sufficiently low according to the results obtained in this study, then the Stokes approximation may be used to determine the velocity vector field around the bubble at the next time step. By using the Stokes approximation, the results should be generated faster. However, if the *Re* is too high, then the NVS equations need to be solved. This is an example of a Lagrangian problem, where each separate bubble is regarded as a moving boundary. In this approach, the velocity of a bubble and hence the local Reynold's number is known. From the criterion developed in the present thesis, it becomes possible to decide if the Stokes solution could be applied or whether the Navier-Stokes equations had to be solved to determine the local fluid velocity vector field.

In developing the cell model, an assumption was made that the bubble is perfectly spherical, which is true for relatively small bubbles. Although large bubbles tend to be cap-shaped, such bubbles rising in a column are associated with high Reynolds numbers, which cannot be modelled using the Stokes equations anyway. This study therefore focuses on regions of flow in a column at low Reynolds numbers around small, spherical bubbles. It is understood that the volume fraction of such regions in a bubble column at any given time is significant. We therefore intend in this work not so much to produce a module that can be used to simulate the entire column, but one that will significantly reduce overall column simulation time by identifying the regions in which the Stokes approximation can be applied.

Before bubble simulations are even attempted, the validity of the numerical solutions obtained from both the Stokes and Navier-Stokes solvers to be used in this work must be established against experimental data for the flow of water past a solid sphere. Once the accuracy of a solver has been established, it can then be used to simulate the flow field around a bubble. As an additional consistency check, the conservation of mass must be

tested by performing an overall mass balance across the entire solution domain. Since the CFD simulation reveals the velocity in each segment in the domain, it is indeed possible to integrate over all the faces of the domain to ensure that the net rate of change of mass of the liquid is zero.

The intention here is to compare the steady state velocity vector fields that evolve around a bubble by applying both the Stokes and Navier-Stokes solvers, with the Navier-Stokes solutions regarded as the most accurate prediction. The computation times required to simulate the steady NVS and Stokes flow fields will be compared, as well as against that for multiprocessor algorithms. The approach taken is therefore to i) simulate NVS flow at increasingly higher mesh resolutions until there is no change in the solution obtained, and ii) simulate unsteady state NVS flow until it is observed that the solution does not change with time. This solution can then be accepted as the standard against which the steady Stokes flow solution can be tested. The accuracy of the Stokes flow solution may then be plotted against the Reynolds number for both the flow around a solid sphere and for the flow around a bubble.

Chapter 4

Stokes Flow

4.1 Physical Description of the Problem

In order to determine the dependence of Stokes flow accuracy on Reynolds number for flow around the bubble, the governing equations for fluid flow must be solved over a suitable domain, such as that illustrated in Figure 4.1. The solution to these equations is the velocity vector field and the pressure field inside the domain. Figure 4.1 indicates the boundary conditions (BC's) on each face, which were used for both the Stokes flow and NVS flow simulations. The prescribed velocity on the flow inlet face is $\mathbf{v}_0$. The free-slip BC's applied on the sides of the domain enforce that the component of flow perpendicular to the face is zero, whereas the components of flow on the face are free to move without stress. A free flow condition means that the fluid may move in any direction without stress. In addition, a reference pressure (P=0), was specified on the flow exit face. The boundary conditions imposed on the surface of the sphere will be discussed later on in this chapter.

There are two reasons why it was decided to enforce free-slip BC's on the sides of the domain, which prevented the fluid from departing from those faces. Firstly, it was found that the computational volume was sufficiently large to capture the necessary features including regions of low and high pressure as well as regions where the velocity changes significantly, such as the wake generated behind the bubble. This was tested by varying the size of the domain, until the solution at a fixed point sufficiently far from the sphere did not change significantly with increasing size. Figure 4.2 shows this domain with the white line indicating the region over which the velocity magnitudes were plotted. This line was positioned $20mm$ from the center of the bubble, parallel to the flow and was $130mm$ long. The velocity magnitude was plotted along this line for three different sized domains each with a bubble diameter of $15mm$ with the smallest domain having dimensions of

130mm by 50mm by 25mm, the medium sized domain having dimensions of 180mm by 100mm by 100mm and the largest domain having dimensions of 160mm by 160mm by 160mm. The change in velocity magnitude with domain size is shown in Figure 4.3, for the flow past a bubble at a Reynolds number of 30. As the domain size increased, the velocities appeared to converge. Minor changes in the velocity were observed when the domain size increased from the medium size to the large size. Thus the base case design was found to have dimensions of 180mm by 100mm by 100mm, for a sphere of diameter 15mm.

The second reason for enforcing free-slip BC's on the sides of the domain was because this "cell" model has similar dimensions to that of a lab scale bubble column, where the fluid is restricted to within the walls of the column.

The centre of the bubble is positioned a distance of 80mm from the flow inlet face, in the x-direction. To generalise these results, the evolution of this space is simulated in terms of the Reynolds number, which is itself a function of the bubble diameter and fluid velocity. In this chapter, the flow profiles around both the solid sphere and the bubble are presented at various Reynolds numbers using the equations for steady Stokes flow.

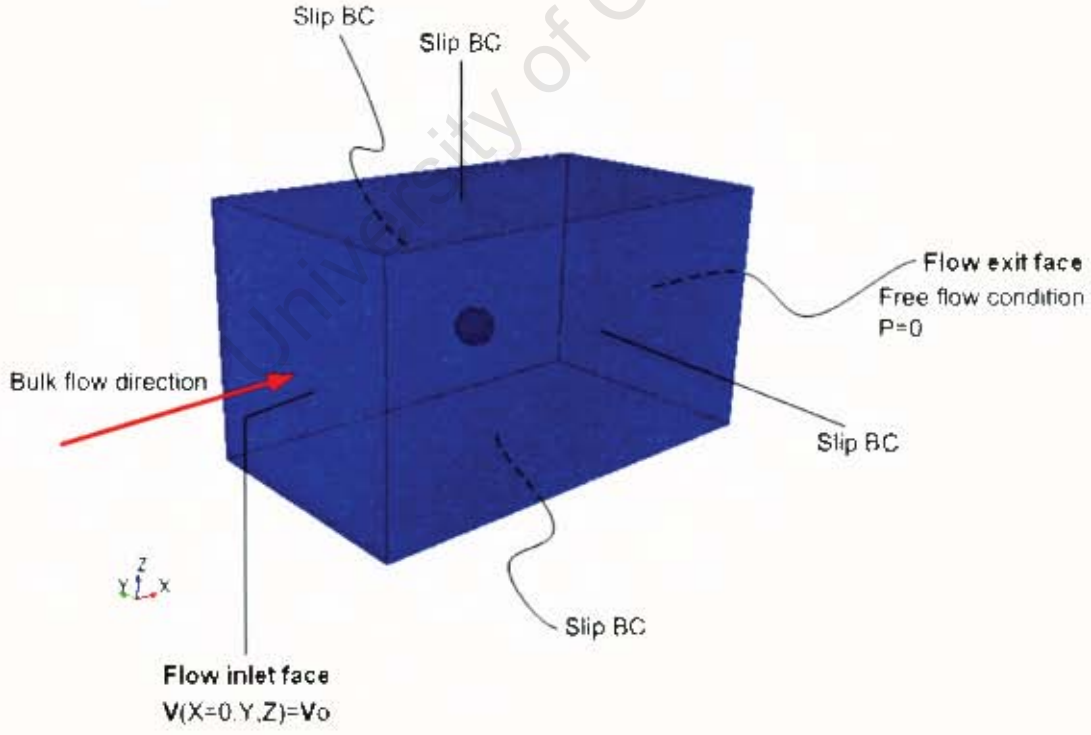

Figure 4.1: The physical domain.

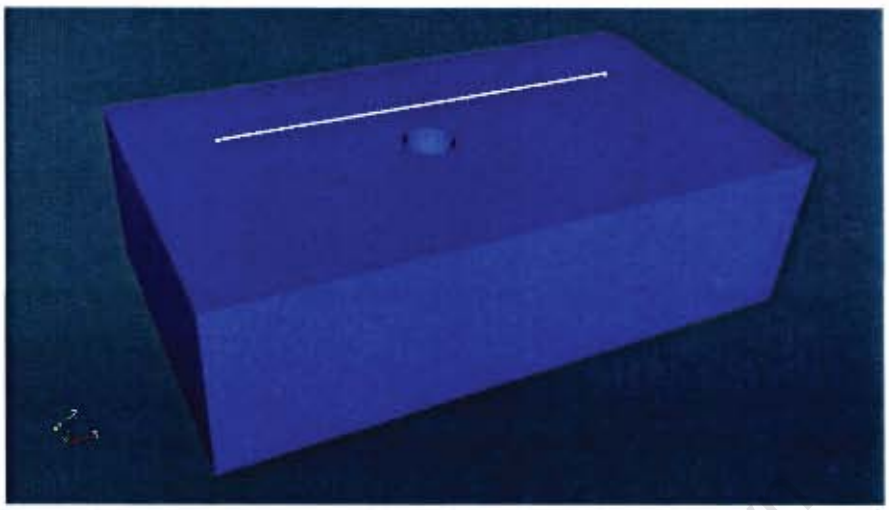

Figure 4.2: Domain containing the white line over which the velocity magnitudes were plotted.

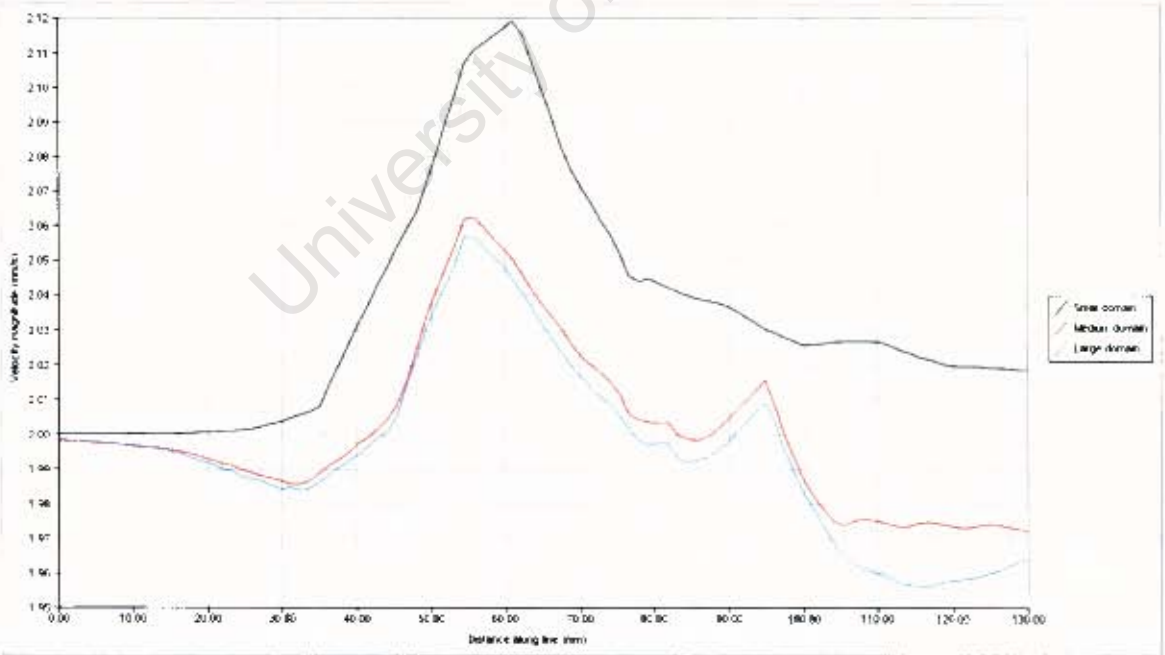

Figure 4.3: Plot of the velocity magnitude profile along the line shown in Figure 4.2 for flow past a bubble for a Reynolds number of 30.

The Stokes equations result from the assumption that the non-linear convective acceleration term in the momentum balance as presented in the Navier-Stokes equations is small in comparison with the other terms. Thus the steady state momentum balance for Stokes flow reduces to that given in equation (4.1) (Clift et al., 1978).

$$0 = -\nabla p + \mu \nabla^2 \mathbf{v} \tag{4.1}$$

The mass balance for incompressible flow which is solved with the momentum balance is given in equation (4.2).

$$\nabla \cdot \mathbf{v} = 0 \tag{4.2}$$

These two equations constitute a fully specified set from which both the velocity vector and pressure fields may be determined.

4.2 Algorithm

The finite element method was chosen to solve the governing fluid flow equations because it can model the curved boundaries that occur in simulating fluid flow around bubbles. In addition, more efficient use can be made of the computational grid space since the method allows for variable resolution across the domain. Finally, the solution is piecewise continuous, which may be considered more accurate than a discontinuous solution.

There are three main steps involved in solving a 3-D computational fluid dynamics (CFD) problem using the finite element method. Firstly, the problem domain must be constructed. This domain, also simply referred to as the geometry, must be meshed as a set of cells, that are normally tetrahedral or hexahedral in shape. This mesh is then used in a finite element program, which discretizes the governing equations, applies boundary conditions and solves the resulting system of matrix equations. The solution vector, which contains values of the unknowns over the entire domain must then be sorted by post-processing software in order to provide the user with a meaningful display of the solution.

4.3 Computational Techniques

4.3.1 Creating the Meshed Geometry

The pre-processor used to create the geometry and mesh was Cubit version 11.0. Figure 4.4 shows a meshed geometry using hexahedra cells, which was used as a starting mesh for all the simulations. This geometry comprised of a cube with a sphere extracted from it, where the cube was itself constructed by joining six pyramids together, as well as an extra block on the front and a longer block on the opposite end to model the fluid wake behind the sphere. The mesh comprised of 1536 cells, which translates to 10,133 nodes and to 40,532 degrees of freedom, as at each node in the mesh the pressure and velocities in each direction are calculated. The central cube was meshed with increasing refinement closer to the surface of the sphere. Boundary indicators were assigned to those faces of cells positioned on the surface of the sphere, and on the outer faces of the domain. These boundary indicators together with the coordinates of the vertices of each cell in the mesh were all imported into the finite element program.

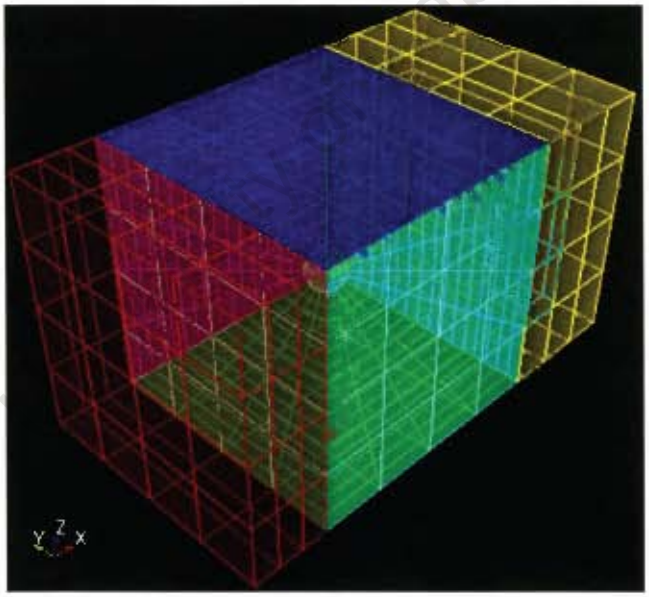

Figure 4.4: The starting meshed geometry used in all the simulations.

4.3.2 deal.II

The governing fluid flow equations for both Stokes and Navier-Stokes flow were solved using deal.II, version 6.1.0, which is an Open Source finite element Differential Equations Analysis Library (DEAL) developed by Bangerth, Hartmann and Kanschat (Bangerth

et al., 2007). This library was written in C++ and provided the user with the necessary tools to write finite element code. The object orientated structure freed the applications programmer from handling the complex data structures. The main advantages of the library included the option to write code independent of the space dimension, to solve finite element method (FEM) problems without writing extensive code and the support for code written in parallel for multiprocessor machines or clusters.

4.3.3 Adaptive Mesh Refinement

In the Stokes flow code, the steady state mass and momentum balances given by Equations (4.2) and (4.1) were solved for the flow past a solid sphere in the domain illustrated in Figure 4.1. Once a solution had been obtained, the velocity vector field was then passed into a function in the code, which calculated the error associated with each cell by integrating the gradients of the velocity over each face of the cell and summing up the resulting values over the entire cell. A refinement fraction was also specified in the function, such that the cells with the highest errors were marked for refinement. This data was saved to file. Each marked cell was then refined by subdividing the cell into eight smaller cells. The above steps were repeated meaning that a total of two refinement cycles had been performed. A mesh smoothing algorithm was implemented to prevent cells with two refinements sitting directly alongside cells with no refinement, by automatically refining cells around the finer cell. The refinement of cells next to the sphere approximated the curve of the sphere more accurately with increasing refinement, as vertices of the new cell were projected onto the boundary.

Simulations were performed at a Re of 80 using adaptive mesh refinement in the Stokes code, with this particular Reynolds number chosen as it was the highest in the range of interest, thus resulting in the largest gradients. The two resulting meshes were used in the Stokes and Navier Stokes codes for $0.1 < Re < 80$. This was achieved by importing the file generated from the Stokes code, which contained cell numbers that were marked for refinement. The starting mesh of 1536 cells increased to 1984 cells after one refinement cycle, and to 3720 cells after two refinement cycles. A portion of the resulting mesh after two refinement cycles is given in Figure 4.5, which shows the refined cells around the sphere. Each quadrilateral has a diagonal line drawn through it, and four quadrilaterals comprise of a face of a cell. This mesh was visualised using Paraview.

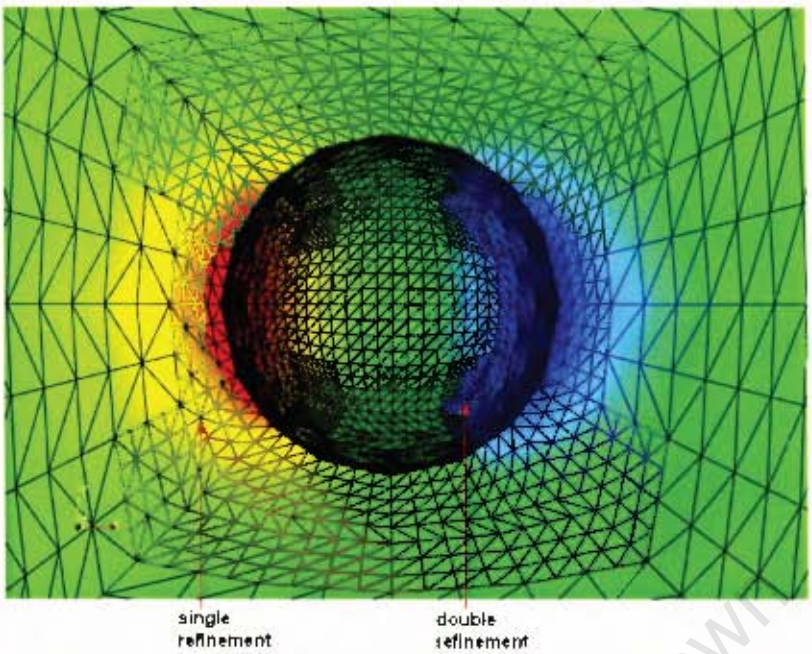

Figure 4.5: A view of the mesh close to the sphere after two Stokes refinement cycles (3720 cells).

4.3.4 Visualisation of the Results

Paraview version 3.2.1 was used to process the results from the deal.II simulations such that the solution data for the 3-D domain was represented in a meaningful manner. The data set was visualised by plotting the pressures and velocities in each direction and linearly interpolating the values to obtain a continuous field. This interpolation was not done using the solution values at the mesh nodes, but rather by using quadratically interpolated solution values between mesh nodes that were determined in the deal.II program. The scalar valued pressures were represented with a colour field only, whilst the vector valued velocities were drawn with a colour field and arrows indicating the direction.

Figure 4.6 illustrates a typical solution, where the velocity field is plotted. The top half of the solution has been sliced off, which allowed the flow field close to the sphere to be visualised. A blue colour represents low velocity magnitudes whilst red indicates high velocity magnitudes. The arrows indicate the direction of the flow for the point located at the base of the arrow, and the size of the arrow is proportional to the velocity magnitude. Thus small, blue arrows indicate low velocity magnitudes and large, red arrows indicate high velocity magnitudes. Figure 4.7 is a pressure field of the gauge pressure, where blue indicates low pressure and red indicates high pressure. These plots are similar to those that will be used in visualising the future results.

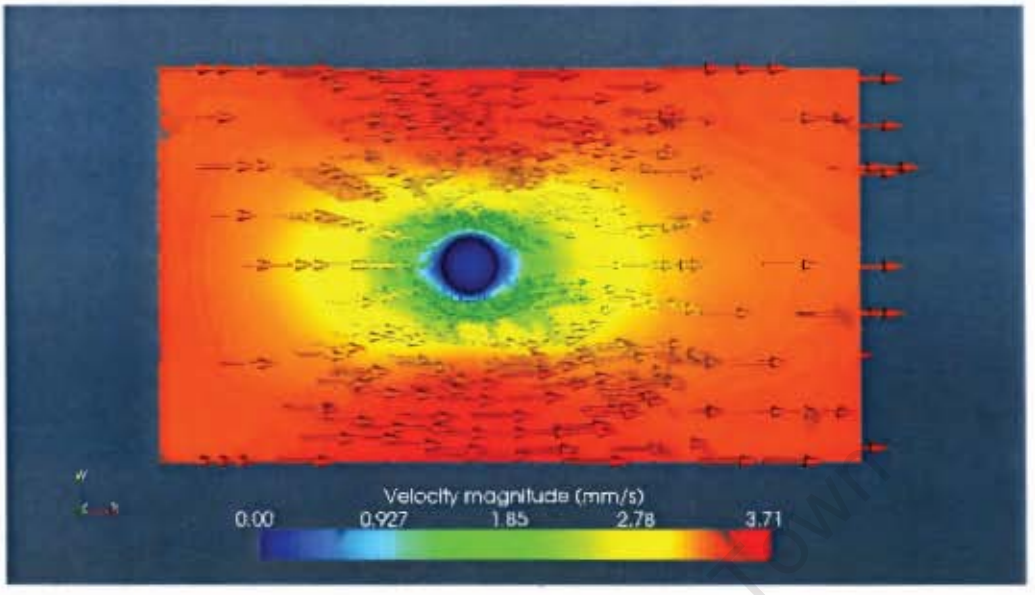

Figure 4.6: Velocity vector field for Stokes flow for a Reynolds number of 50.

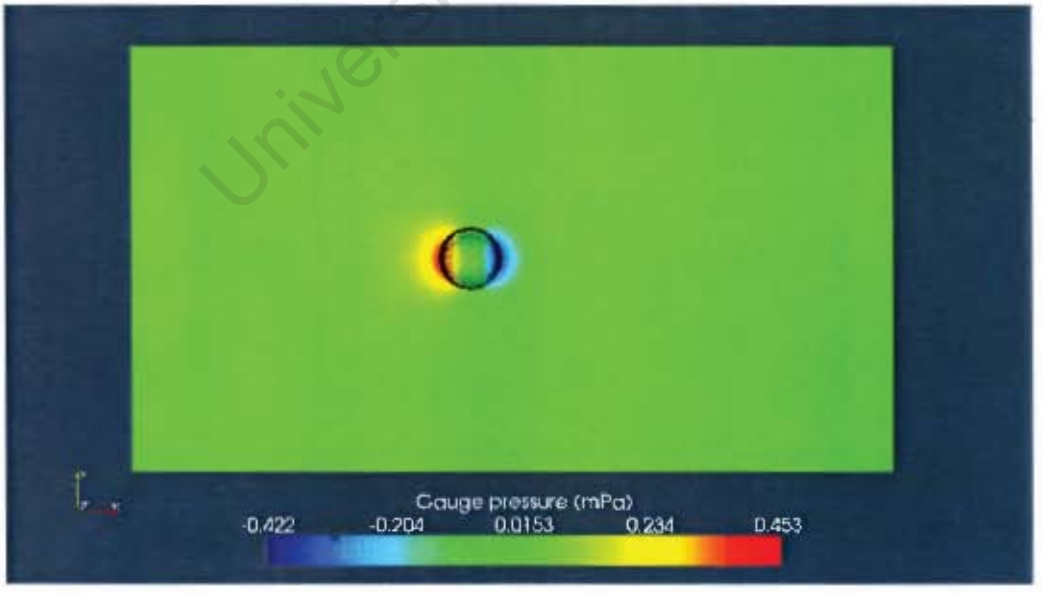

Figure 4.7: Pressure field for Stokes flow for a Reynolds number of 50.

4.4 Flow Past a Solid Sphere

4.4.1 The Experimental Result

In order to validate the simulation, and given the lack of available experimental data for the case of flow past bubbles, the flow of water past a solid sphere was first investigated. Once the FEM model for the flow past a solid sphere was validated, the model for the flow of water past a bubble could be considered correct as the only difference is in the setting of the BC's on the surface of the sphere, which will be explained later on in this chapter. Indeed, as we shall see, the boundary conditions in the case of a solid sphere generate far sharper discontinuities in the solution than in the case of the bubble. As such, if the simulator can be shown to give accurate results in this case, it can also be trusted for the case of gas bubbles.

The experimental result is shown in Figure 4.8, which illustrates the flow pattern of water behind a solid sphere at a Reynolds number of 26.8, with the free stream flow direction from left to right. The lines in the picture are streamlines which indicate the direction of the flow, as each point on a streamline is tangential to the velocity field. These streamlines were visualised by the illumination of aluminium dust and the solid sphere was a steel ball-bearing. The picture captures the small concave wake behind the sphere.

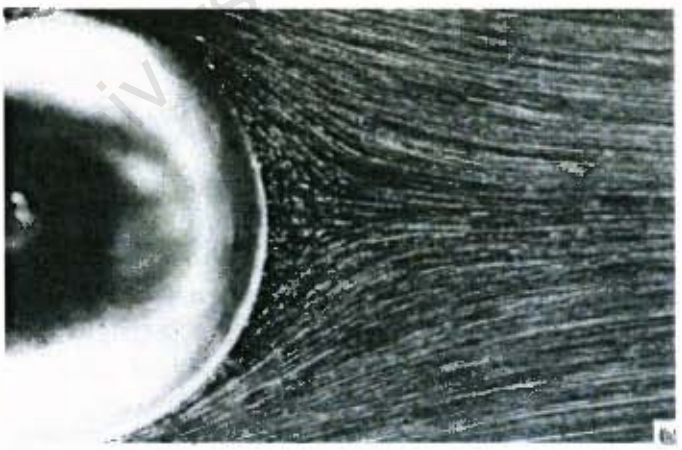

Figure 4.8: Experimentally observed flow field behind a solid sphere for Re=26.8 taken from Taneda (1956).

4.4.2 Numerical Results

In this section, the setting of the model parameters and BC's are described for the flow around the solid sphere, with some preliminary results presented. These results indicate typical trends for Stokes flow, such as the velocity field around the sphere and how this field changes with the Reynolds number. Here $Re = \frac{DU}{\nu}$, where D is the sphere diameter, U is the free stream velocity and ν is the kinematic viscosity of the fluid.

The Stokes equations were solved over the computational domain illustrated in Figure 4.1. A velocity of $0.0\overline{6}\,mm/s$ was prescribed everywhere on the flow inlet face. The boundary condition for the surface of the solid sphere was a 'no slip' condition, which meant that the fluid velocity was set to be zero everywhere on that surface. The fluid kinematic viscosity was set to $1\,mm^2/s$ (water at 25 °C). Figure 4.9 illustrates the bottom half of the steady state velocity field for Stokes flow at a Reynolds number of 1. The arrows indicate the fluid direction and the colour field gives the magnitude of the fluid velocity. As the fluid approached the sphere, it diverged and slowed down, whilst the velocity of the fluid on the outskirts of the domain increased. On the right hand side of the sphere, the fluid velocity increased with increasing distance from the sphere. Figure 4.10 shows this change in velocity for the fluid near the sphere. As the Reynolds number was increased, the trend remained the same.

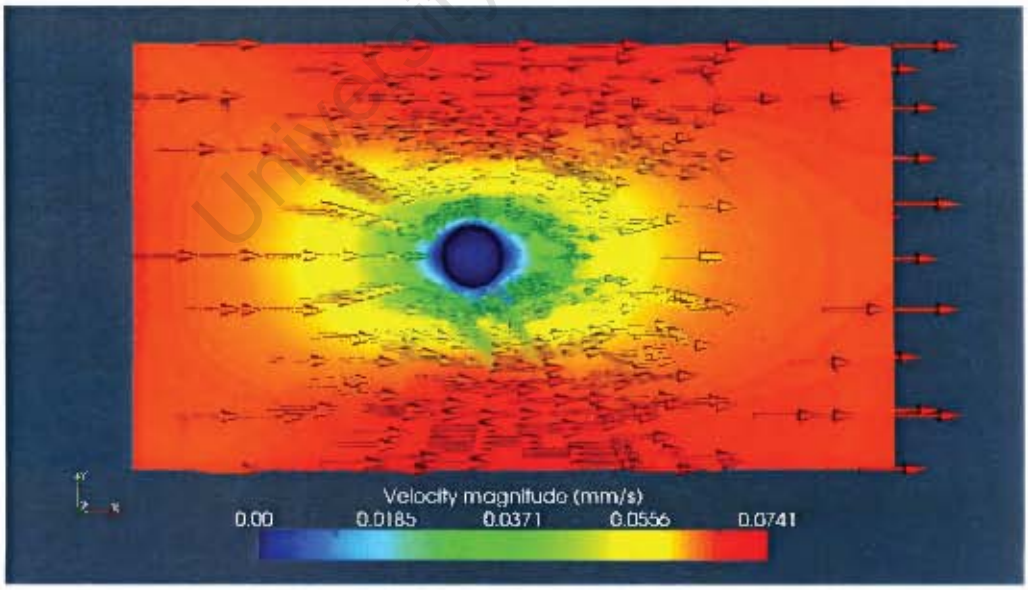

Figure 4.9: Velocity field for water flowing past a solid sphere at Re=1.

These trends give a qualitative representation of the model for the flow of water past a solid sphere, thus a comparison can be made between these results and those for the

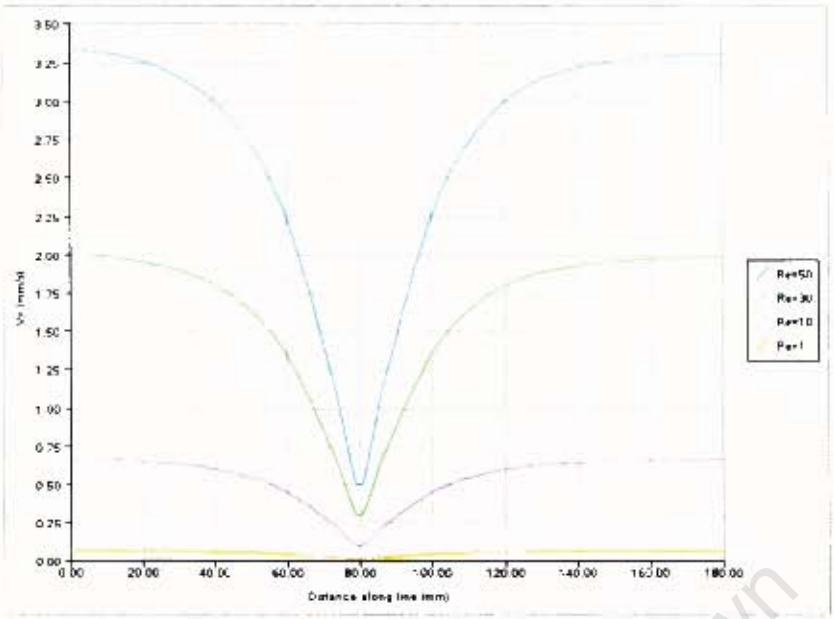

Figure 4.10: Plot of v_z along the center line in the x-direction, $0.5mm$ away from the sphere.

flow of water around a bubble, presented in the next section. Such a comparison may be considered useful in understanding the effect of the change in the BC implemented on the surface of the bubble.

4.5 Flow Past a Bubble

A model of fluid flow past a bubble differs from that of fluid flow past a solid sphere, only in terms of the boundary condition applied on the sphere surface. In this case, the 'slip' velocity boundary condition given in equations (4.3) and (4.4) was used, proposed by Clift et al. (1978).

$$\mathbf{v} \cdot \mathbf{n} - 0 \tag{4.3}$$

$$\tau = 0 \qquad \text{(everywhere tangential to the sphere)} \tag{4.4}$$

Equation (4.3) states that the component of velocity in the normal direction to the surface of the sphere is zero. Equation (4.4) states that the shear stresses (τ) tangential to the sphere are zero. Generally, these conditions specify that the fluid is allowed to flow freely past the bubble, such that the bubble behaves as a void in the flow domain.

In a similar fashion to the previous section on the flow past a solid sphere, the parameters for a typical simulation for the flow of water past a bubble are described. To understand the implications of the boundary conditions described, a particular simulation result is presented here. In this exercise, a velocity of $0.0\overline{6}\,mm/s$ was prescribed everywhere on the flow inlet face. The resulting velocity field for a Reynolds number of 1 is shown in Figure 4.11. The difference between this result and the one for flow around a solid sphere was that the bubble did not slow the fluid down as much. In contrast to no-flow in the case of the no-slip solid sphere, the arrows drawn on the bubble surface indicate significant movement of fluid flow there. Figure 4.12 shows the general decrease in velocity in the x-direction as the fluid approaches the bubble, although the velocity increases slightly at the point $0.5mm$ from the bubble, which is caused by high velocities on the bubble surface where the surface is tangential to the bulk flow direction. This trend remains constant with the Reynolds number.

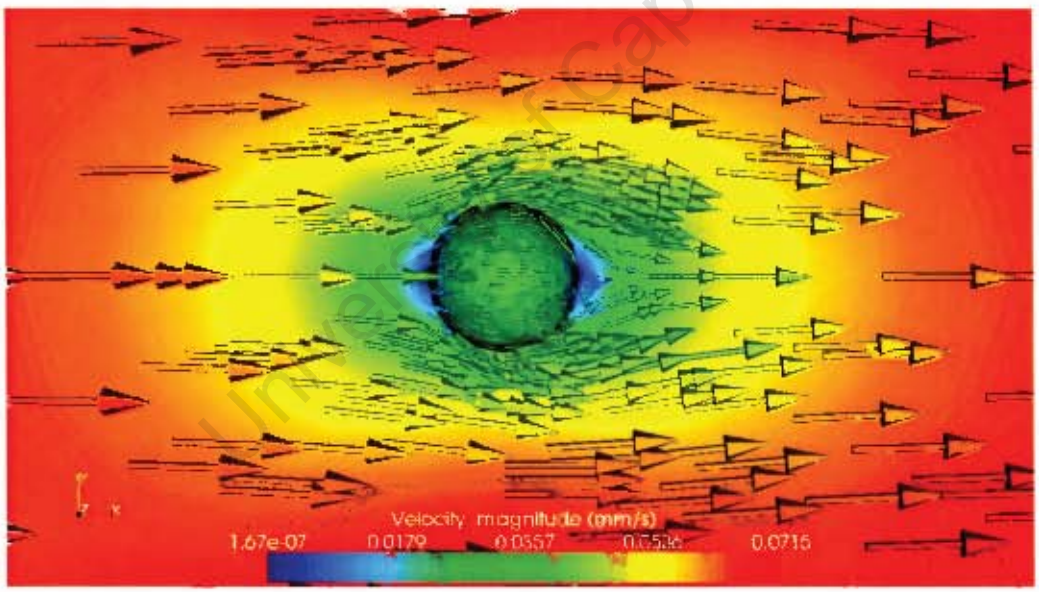

Figure 4.11: Velocity field for water flowing past a bubble at Re=1.

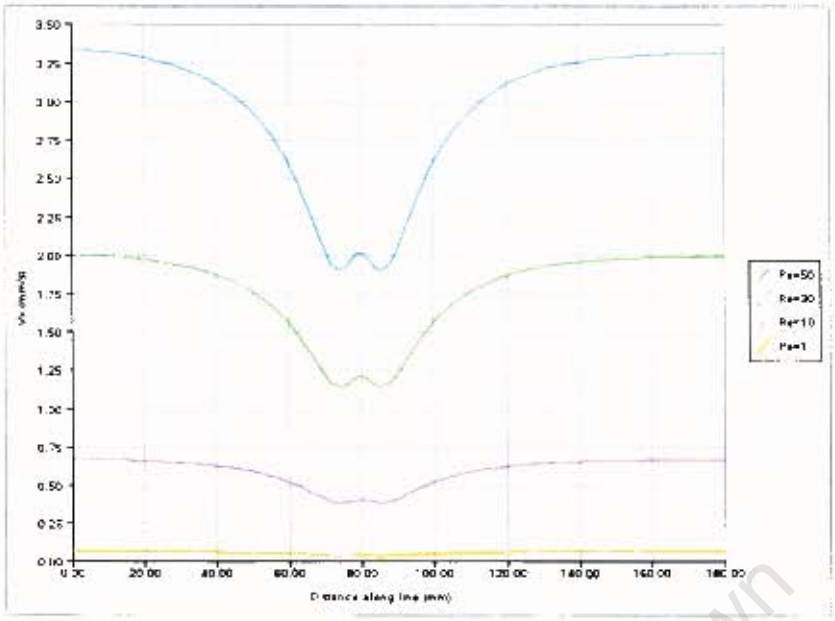

Figure 4.12: Plot of v_x along the center line in the x-direction, $0.5mm$ away from the sphere.

From the trends in the velocity field observed above in Figures 4.11 and 4.12, there was no region of disturbed flow of low velocity downstream of the bubble. This is unexpected, as a wake comprising of a sharp front and a long tail should be present due to the displacement of the fluid. These trends in the velocity profile around both the solid sphere and the bubble at various Reynolds numbers will be compared to those obtained from the solution of the full NVS equations.

Chapter 5

Navier-Stokes Flow

The intention of this chapter is to firstly develop the governing equations and BC's for Navier-Stokes flow, then to explain how the equations were solved using the finite element method, and finally to demonstrate how the results may be interpreted.

5.1 Physical Description of the Problem

The Navier-Stokes equations, introduced in Chapter 1, Section 3, are solved over the identical domain used for Stokes flow. This domain together with the boundary conditions, is described in Chapter 4, Section 1. In this study, the Navier-Stokes equations to be solved include the momentum and mass balances. The momentum balance is given in eq. (5.1) and the continuity equation is given in eq. (5.2).

$$\rho\frac{\partial \mathbf{v}}{\partial t} + \rho\mathbf{v}\cdot\nabla\mathbf{v} = -\nabla p + \mu\nabla^2\mathbf{v} \tag{5.1}$$

$$\nabla\cdot\mathbf{v} = 0 \tag{5.2}$$

The difference between this set of equations and those solved for Stokes flow is that the momentum balance includes a non-linear convective term, which describes the bulk transport of momentum through the system, and an accumulation term, which describes the unsteady nature of the flow. However, the steady state solution will be found and used for comparison against the Stokes flow results.

The boundary conditions imposed on the domain were identical to those used in the Stokes flow simulations. These include a constant velocity everywhere on the flow inlet face, a free flow condition on the flow exit face together with a zero pressure, and 'slip'

BC's on the remaining sides. A 'no-slip' condition was enforced on the surface of the solid sphere, and a 'slip' BC was enforced on the surface of the bubble, given by equations (4.3) and (4.4) in chapter 4.

The velocity and pressure everywhere within the fluid were given the initial values of zero. The entry of an incompressible fluid was then modelled as entering one face of the domain. Since 'slip' BC's were chosen on all other faces (to simulate free flow), and due to the simplicity of the expression for the incompressible material balance, the fluid was expected to reach steady state in a short period of time.

5.2 Algorithm

The finite element method was used to solve the governing fluid flow equations (5.1) and (5.2). The momentum balance included an unsteady state term, which yielded a time dependent solution. The simulation was performed over a reasonably long period of time to converge to a steady flow field. The general algorithm for solving the FEM problem described in Chapter 4, Section 2, was implemented. In this approach to solving the NVS equations, the algorithm was designed for multiple processors by splitting the task of assembling the matrix equations so as to speed up the program run time. The time step size and the overall time were input variables. At each time step, the solution from the previous time step was used as the initial condition, the equations solved and the results were saved to file.

5.3 Computational Techniques

5.3.1 Tools Used

The mesh generated in Cubit shown in Figure 4.4 which was imported into the Stokes flow code, was also imported into the Navier-Stokes flow code. In addition, the adaptively refined mesh generated in the Stokes flow program, was used in the NVS code, allowing for direct comparison of the predictions from each approach. The refinement is regarded as adequate for both the Stokes and NVS simulations since cells close to or on the surface of the sphere were at a higher resolution than in the bulk fluid, which is in alignment with the region of the greatest velocity gradient changes. Although the flow field behind the sphere is of particular interest, these cells were already comparatively small, even without any refinement.

The incompressible, unsteady Navier-Stokes equations were solved in 3-D using a Navier-Stokes solver program, written using deal.II. This code was originally developed by Martin Kronbichler from Uppsala University in 2008 and was validated by comparing the Beltrami flow solution from simulation with the analytical solution and found to be in excellent agreement. Paraview was used to view and analyse the solution data.

The finite elements used were polynomial functions of order 2 for the vector-valued velocity components and of order 1 for the pressure. Thus a LBB-Stable element pair $Q_2 \text{x} Q_1$ were used, also known as the Taylor-Hood element. For this problem, a solution only exists if the function spaces in which a solution is searched for satisfies certain conditions. These particular conditions are the Ladyzhenskaya-Brezzi (LBB) conditions. In addition, the finite element spaces must also be compatible with the LBB condition. Identical finite elements were chosen for the Stokes problem for the same reasons.
The time integration algorithm chosen was BDF-2. The BDF-2 method comprises of a trapezoid step over part of the time step followed by a second order backward difference step over the remainder of the time step. The quality of the initial guess for the nonlinear iteration is considerably improved when using this method compared to implicit Euler, which just uses the solution value at the previous time step. In the BDF-2 algorithm, the previous two solution values are extrapolated to obtain the initial guess for the nonlinear iteration.

The simulations were performed on a quad core PC, with each processor at 2.4 GHz, and with the system at 8 GB of RAM. Programs were also run on the Chimera cluster housed in the Chemical Engineering Department at the University of Cape Town, which comprised of multiple nodes, with a single node typically having four CPUs, each running at 2.2 GHz, and 8 GB of RAM. The option for parallel processing was enabled for all the NVS simulations.

5.3.2 Convergence to Steady State

As the momentum balance from equation (5.1) contains a time dependent term, namely $\rho \frac{\partial \mathbf{v}}{\partial t}$, the solution to equations (5.1) and (5.2) result in a solution which is a function of time. The steady state solution to the NVS equations needed to be determined for each simulation in order for comparison with the steady Stokes flow results. Thus a given NVS simulation was run with an error analysis to determine steady state. The flow field was also observed in Paraview with time, although an accurate steady state time could not be determined by this means because small changes in the flow field occur that are not visible in the Paraview solution. The mathematical approach to determining the steady

state time which was implemented used the L2 norm ($\|\mathbf{x}\|_2$), also known as the L2 error given in equation (5.3).

$$\|\mathbf{x}\|_2 = \sqrt{\sum_{i=0}^{n} |x_i|^2} \tag{5.3}$$

In equation (5.3), x_i is the i^{th} component of vector $\mathbf{x}$ and n is the length of the vector. A large L2 norm indicates that one or more components have a large value. In terms of using the L2 norm to determine steady state, the vector $\mathbf{x}$ was generated by subtracting the NVS velocity vector field at a given time step number from the velocity vector field at the previous time step. This subtraction meant that each component of velocity at each node in the computational domain was subtracted from the equivalent velocity component at the corresponding node. Thus as every velocity component in the solution remains constant with time, each component in the vector $\mathbf{x}$ should be close to zero, thus the L2 norm should also be close to zero.

In order to determine the steady state time the L2 errors for a given NVS simulation were saved to file and plotted against time using Gnuplot version 4.2. Figure 5.1 is the plot of the L2 error between successive time steps for the flow of water around a solid sphere at a Reynolds number of 10, with a time step size set to one second. This step size was the length of time the fluid flowed through the domain before the equations were solved again. A steady state time of 500s was read off Figure 5.1 by taking the time where the error stopped decreasing and reached an approximately constant value. This steady state value was in good agreement with the qualitative value mentioned earlier. The system was interpreted as reaching steady state even though the data was scattered because the source of the scatter was considered to be numerical error. This seemed reasonable as the value of the L2 norm after a time of 500s was orders of magnitude smaller than even the highest values of velocity magnitude present. This analysis was performed for NVS simulations for a range of Reynolds numbers between 0.1 and 100, including flows around the solid sphere and the bubble. In addition, NVS simulations were also performed using different simulation operating conditions, such as mesh refinement and time step size.

5.4 Flow Past a Solid Sphere

The NVS equations were solved over the same computational domain used in the Stokes flow simulations, with the same boundary conditions, thus a 'no slip' condition or zero

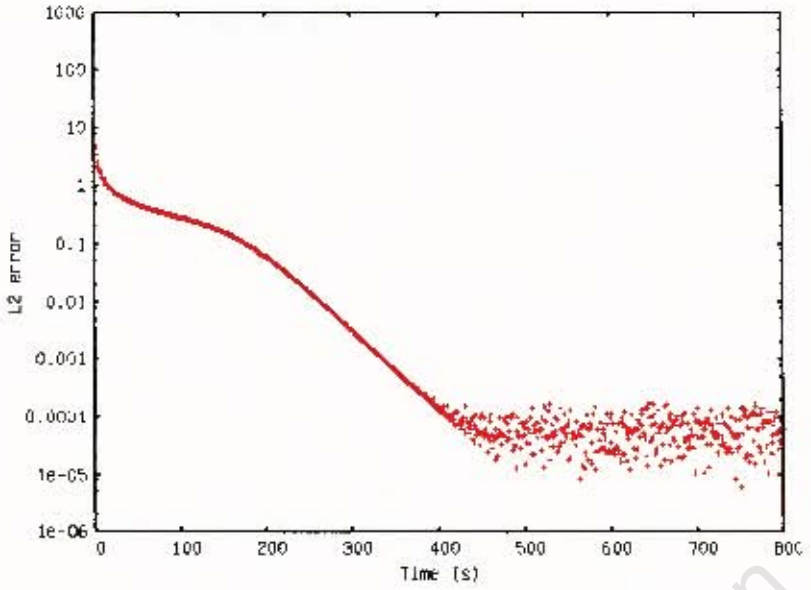

Figure 5.1: The velocity-based L2 error plotted with time for the flow of water past a solid sphere at a Reynolds number of 10.

velocity was applied to the surface of the sphere. The velocity on the flow inlet face was varied to control the Reynolds number, as the diameter of the sphere and the kinematic viscosity of the fluid were constant. Figure 5.2 illustrates half of the steady state velocity field at a Reynolds number of 50. A velocity of $3.33\overline{3}\,mm/s$ was prescribed everywhere on the flow inlet face. The time step size was set to 1 second for the simulation and the steady state time was 100 seconds. As the fluid approached the anterior face of the sphere, it decelerated and diverged, with the fluid identically on the surface of the sphere having a no-slip zero velocity. The fluid flowed around the sphere, but a wake was formed in the region directly behind the sphere, with a significantly lower velocity than that found in the free stream.

In order to quantitatively understand the flow mechanics of the wake, the x-component of velocity was plotted along the center line in the x-direction, directly through the sphere, indicated by the white line in Figure 5.2. This was repeated for a variety of flow rates with the trends shown in Figure 5.3. The Reynolds number ranged from 10 to 80, and a common trend observed was that the velocity decreased to zero as the fluid approached the sphere. However, the velocity of the fluid in the wake behind the sphere was significantly less than that of the free stream velocity. As the Reynolds number was increased, the ratio of the wake velocity to the free stream velocity decreased. For Reynolds numbers above 50, the fluid directly behind the sphere travelled in the reverse direction to the main flow. This was very different to the velocity flow field behind the solid sphere for Stokes flow,

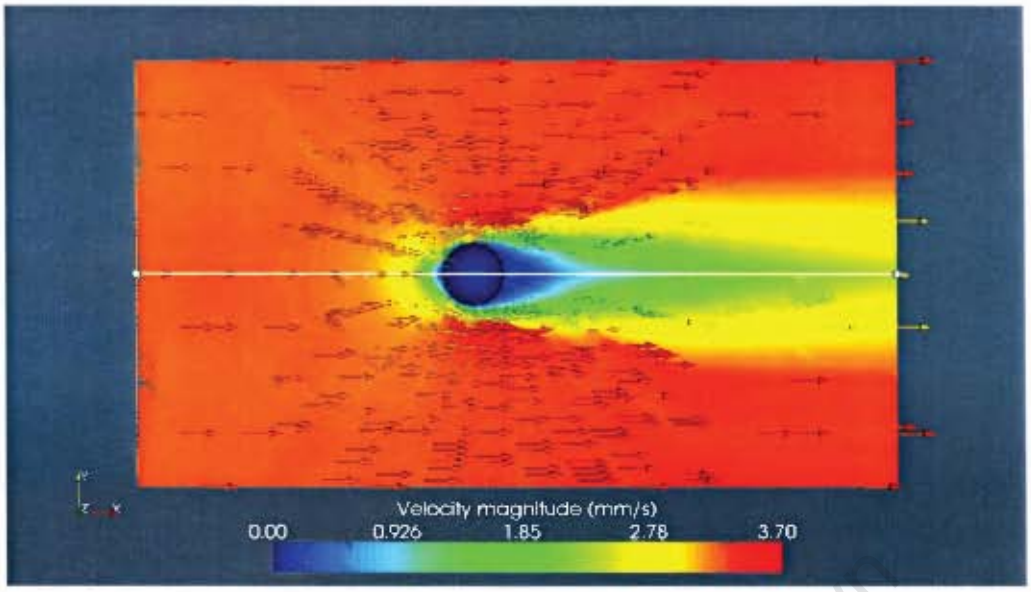

Figure 5.2: A section of the velocity field for water flowing past a solid sphere at Re=50. The arrows indicate the direction of the flow and the colour bar indicates the velocity magnitude.

where no low velocity wake was present at the same Reynolds numbers. In the case of Stokes flow, the absence of a wake behind the sphere may be expected as the momentum balance does not include the convective transport term namely $\rho \mathbf{v} \cdot \nabla \mathbf{v}$. This convection term may also be considered as an inertial term, as it contains the product of density and the spatial acceleration of the fluid. This phenomena of a wake existing behind the solid sphere is observed experimentally, and is shown in Chapter 6. It is observed that a significant change in the velocity field around a solid sphere occurs when the fluid motion is modelled using the Stokes equations compared to using the NVS equations. In the next section a similar comparison will be made for the flow around a bubble.

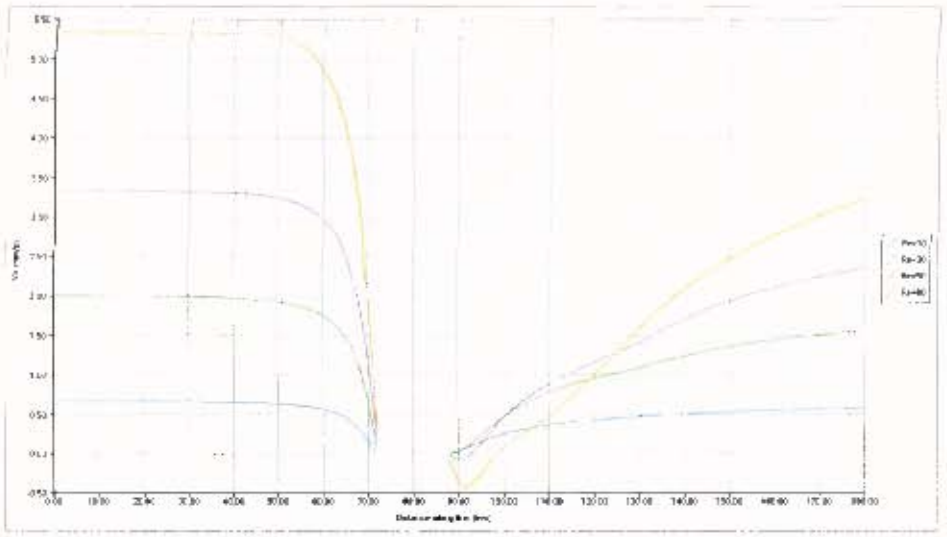

Figure 5.3: Plot of u_x along the center line in the x-direction, directly through the sphere, for flow around a solid sphere.

5.5 Flow Past a Bubble

In determining the velocity field around a bubble using the NVS equations given by eq. (5.1) and eq. (5.2), a comparison can be made against the equivalent flow field obtained by solving the Stokes equations. The NVS simulation was performed where a velocity of $3.33\overline{3}\,mm/s$ was prescribed everywhere on the flow inlet face, thus setting the inlet Reynolds number to 50. The simulation setup was identical to that of the flow past a solid sphere in the previous section although the BC on the surface of the bubble was changed to the 'slip' condition. The velocity flow field around a bubble for a Reynolds number of 50 is shown in Figure 5.4. Again the difference between this result and the one for flow around a solid sphere was that the bubble did not slow the fluid down as much. Red arrows are visible on the bubble surface, indicating significant movement of fluid on the surface. A small wake is present behind the bubble, with the fluid in the wake having a slightly lower velocity than that around it. This wake behind the bubble was not observed for the Stokes flow simulation at the same Reynolds number.

The x-component of velocity was plotted along the center line in the x-direction, directly through the sphere for various Reynolds numbers, shown in Figure 5.5, which is an equivalent plot to that in Figure 5.3. This plot showed the existence of a wake, as the velocity of the fluid behind the sphere, ie. after $88\,mm$, was less than that in front of the sphere, ie. before $72\,mm$. As the Reynolds number was increased, the existence of a wake became more noticeable. In this case the velocity directly behind the sphere did not drop below zero, whereas for the flow around the solid sphere negative flows existed.

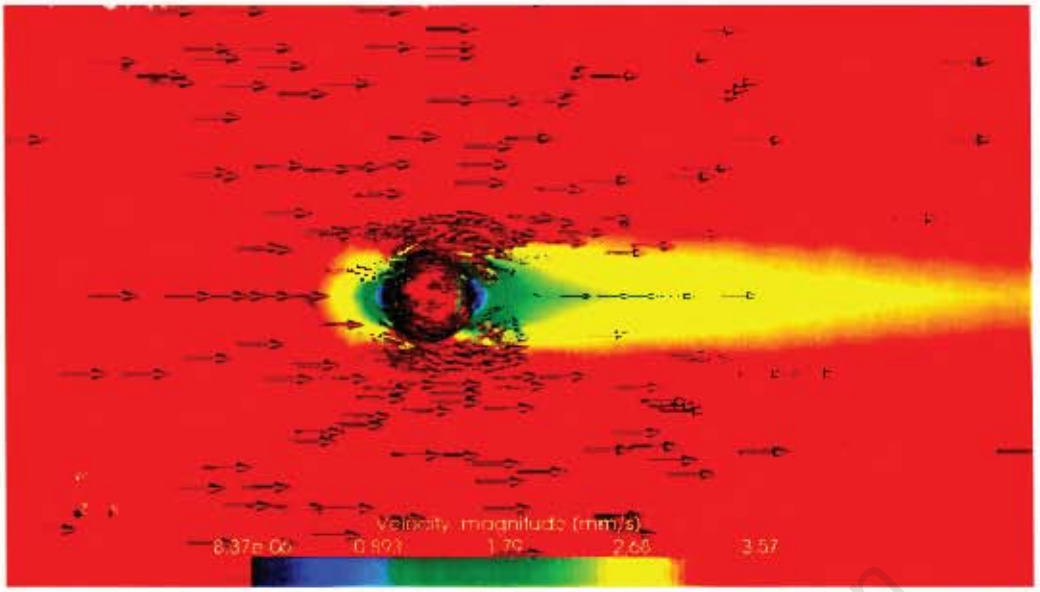

Figure 5.4: Velocity field for water flowing past a bubble at Re=50. The arrows indicate the direction of the flow whereas the colour field indicates the velocity magnitude.

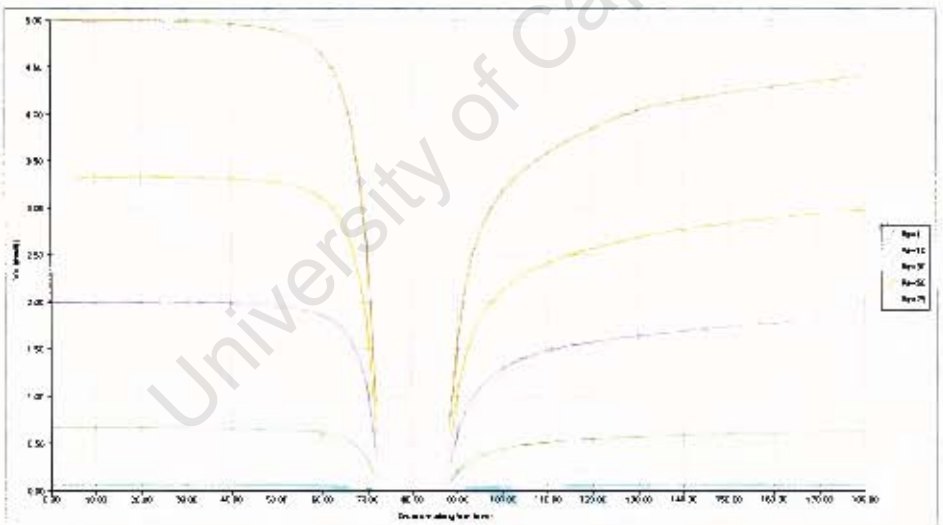

Figure 5.5: Plot of v_x along the center line in the x-direction, directly through the sphere, for flow around a bubble.

The results for the NVS model in this chapter show that for both the flow around a solid sphere and the flow around the bubble a wake or low velocity region is present behind the sphere, whereas equivalent Stokes results did not show this. This fundamental difference in the simulation results may be attributed to the convective transport term which appears in the NVS momentum balance but in not the Stokes momentum balance. Secondly, as the Reynolds number is decreased, the existence of the wake becomes less noticeable,

which is also consistent with the theory as Reynolds number is the ratio of the inertial to viscous forces, so at low Re the convective term becomes less dominant and the NVS velocity fields resemble the Stokes velocity fields.

The validation of these simulations is necessary in order to make an accurate comparison between the Stokes flow and the NVS flow velocity fields around a bubble. This work on the validation of the NVS program is presented in the next chapter.

Chapter 6

Validation of Model for Flow Past a Solid Sphere

This chapter presents validation of the Navier-Stokes simulations for the flow of water past a solid sphere at Reynolds numbers below 100 by comparison with published data in the literature. It was shown that the Navier-Stokes model predicts the correct velocity fields for Reynolds numbers of 26.8 and 73.6. At Reynolds numbers above 30, eddies occur behind the sphere, and can be predicted by the Navier-Stokes solver but not by the Stokes approach.

In validating the NVS simulations for the flow past a solid sphere, the resultant flow fields may then be considered as trustworthy benchmark standards, against which the Stokes simulations can be assessed. The flow field of water past a bubble as simulated by the NVS solver may then be considered correct also because only the BC on the sphere surface is different compared to the solid sphere. This is likely to be even more correct as the 'slip' BC does not create sharp velocity gradients on the bubble surface.

6.1 Validation Approach

The first step in validating the Navier-Stokes flow simulations (NSFS) with published experimental data from literature is to qualitatively compare the results in terms of their flow structures. Important features include the shape of the fluid streamlines particularly behind the solid sphere, and regions of velocity which differ considerably to that of the free stream. In the cases where the NSFS do match the equivalent experimental results, numerical comparisons of the velocity fields will be performed to completely validate the result. However, the flow structures around a solid sphere are not equivalent to those around a bubble at the same Reynolds number, due to the no-slip BC applied to the

surface of the solid sphere. Despite this, if the NSFS can be shown to predict the correct flow structures and the onset of turbulence around the solid sphere, then in the case of a bubble, where the BC is actually milder because there are no sharp gradients at the sphere surface, the NVS simulations for flow around a bubble can be accepted as correct. It is therefore accepted in this work that validation in the more conservative case of a non-slip sphere constitutes validation of a free-slip bubble. Such an approach is necessary because there are no equivalent experimental data available for bubbles due to the experimental difficulty of fixing a bubble and measuring the flowstreams around it.

6.2 Comparison of Flows at Re=26.8

In this simulation, the Navier-Stokes solver was used on the adaptively refined mesh consisting of 3720 cells, described in Chapter 5. The boundary conditions are as follows:

i) The Reynolds number was set to 26.8 by adjusting the free stream velocity to $1.78\overline{6}\,mm/s$.
ii) The no-slip condition was applied to the surface of the sphere.
iii) The BC's on the sides of the domain remain the same as described in Chapter 5.

Figure 6.1 shows the velocity field directly behind the sphere for this simulation. From the direction of the arrows, the fluid appears to simply flow around the sphere and rejoin again to form the free stream. The low velocity region directly behind the sphere is slightly concave, and there are no eddies or backmixing. Taneda (1956) found the same result at a Reynolds number of 26.8, for an experiment where a solid sphere was dragged through initially still water, shown in Figure 6.2. In this picture the flow field is represented by streamlines, which by definition are tangential to the velocity field. These streamlines indicate the path that a small particle would travel if placed in the fluid. A low velocity region can be observed directly behind the sphere indicated by the broken streamlines. It is clear that the streamlines follow a concave path behind the sphere before rejoining to form the free stream. This result is therefore considered a qualitative validation of the result produced by the NVS solver, since the same basic flow structures are evident.

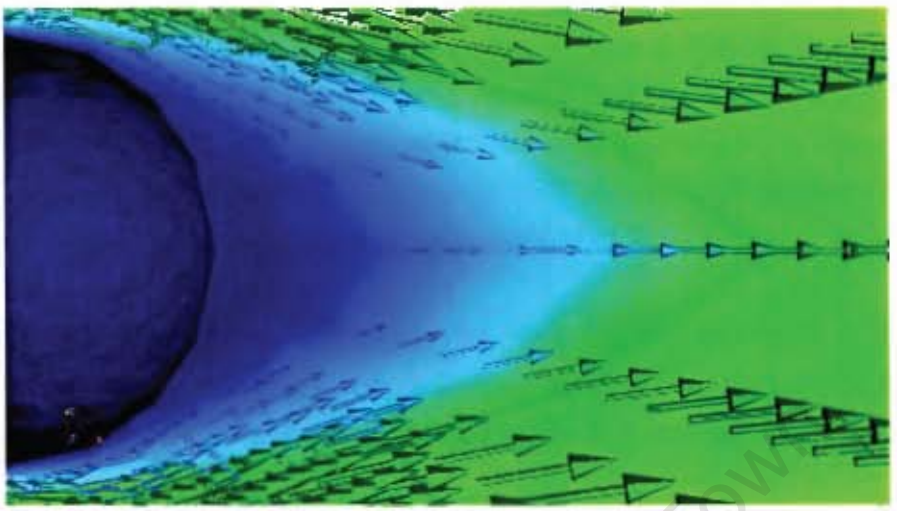

Figure 6.1: Velocity flow field behind a solid sphere for Re=26.8 using the NVS solver.

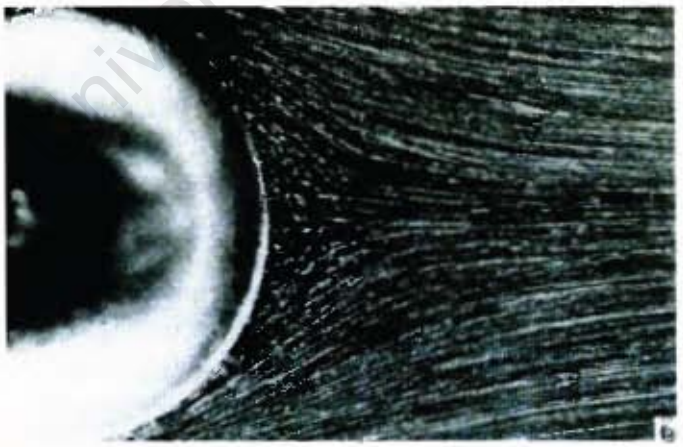

Figure 6.2: Experimentally observed flow field behind a solid sphere for Re= 26.8 taken from Taneda (1956).

6.3 Comparison of Flows at Re=73.6

The experimental result for the flow of water past a solid sphere at a Reynolds number of 73.6 taken from Taneda (1956) is illustrated in Figure 6.3. This shows different flow patterns in comparison with the flow at a Reynolds number of 26.8. In this case a convex wake exists behind the sphere together with symmetrical eddies (circulation patterns) and backmixing. The wake which converges to form the free stream, is longer than that found at a Reynolds number of 26.8. Nakamura (1976) showed that the shape of the wake changes from concave to convex at a Reynolds number of 35.

This experimental result is in close agreement with the simulation result. When the Reynolds number was increased to 73.6 by adjusting the free stream velocity to $4.90\overline{6}\ mm/s$ in the Navier-Stokes solver, a number of changes to the flow structure were observed. Figure 6.4 shows a view of the wake behind the sphere generated by the NVS solver. A slightly convex wake was formed with eddies and backmixing. The low velocity region indicated by the blue colour extended much further behind the sphere compared to the flow at a Reynolds number of 26.8.

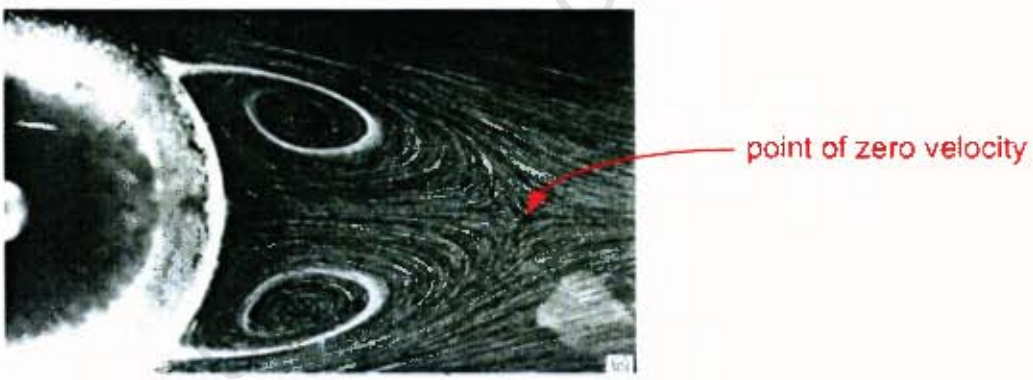

Figure 6.3: Experimentally observed flow field behind a solid sphere for Re=73.6 taken from Taneda (1956).

In order to compare the results generated by the Stokes and Navier-Stokes simulations, the Stokes flow solver was also used to predict the flow around a solid sphere at a Reynolds number of 73.6. The velocity flow field directly behind the sphere is shown in Figure 6.5. In contrast to the results from the NSFS, the prediction from the Stokes flow simulation (SFS) does not show circulating eddies nor backmixing. Thus the Stokes flow solver does not predict the correct velocity field at this high Reynolds number. Generally speaking, due to the assumption of negligible convective flow, Stokes flow models tend to fail at higher Reynolds numbers. A comprehensive accuracy analysis is attempted in Chapter 7.

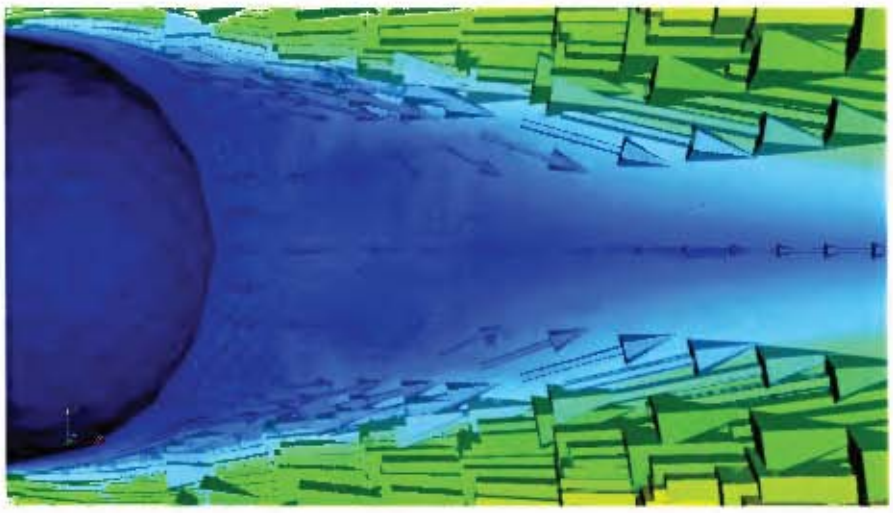

Figure 6.4: Velocity flow field behind a solid sphere for Re=73.6 using the NVS solver.

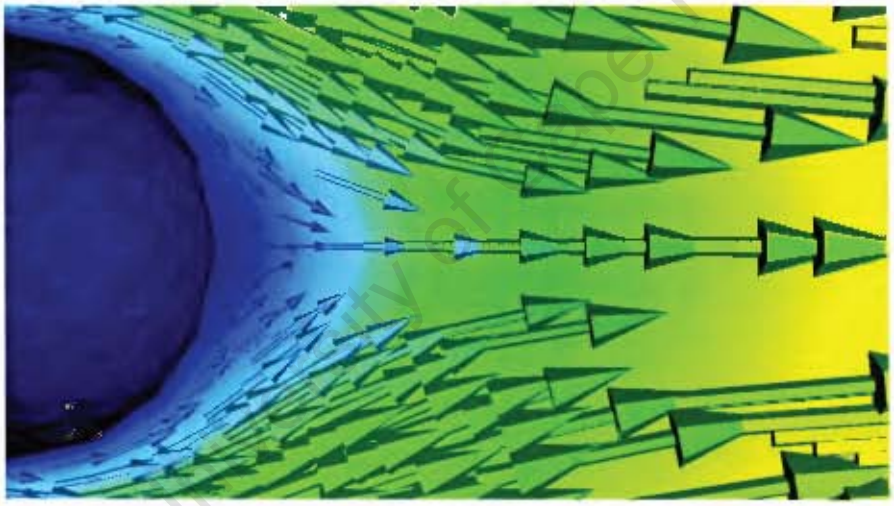

Figure 6.5: Velocity flow field behind a solid sphere for Re=73.6 using the Stokes solver.

6.4 An Analysis of the Wake

At higher Reynolds numbers, eddies and backmixing occurred behind the solid sphere. The region that contains these eddies may be referred to as the wake (Taneda, 1956). Due to the backmixing influence, along the centerline behind the sphere an unstable point exists at which the velocity has an approximate value of zero. This point is indicated in Figure 6.3 which also shows that the wake extends from the surface of the sphere to this so-called point of zero velocity. Thus the wake length may be measured from the surface of sphere between the symmetrical eddies to this so-called point of zero velocity.

The open source Paraview software was used to plot the velocity magnitude along the centerline behind the sphere. Figure 6.6 shows a cut-away section of the computational domain, with half of the sphere visible. The white line indicates the domain over which the velocity magnitude was plotted in Figure 6.7. The velocity magnitude increased with distance along the white line, then decreased to almost zero, then increased again. The fluid was travelling in the reverse direction to the bulk fluid in the region between $0mm$ and $9.68mm$. Thus for this particular Reynolds number the wake length was calculated to be $9.68mm$ according to the above mentioned definition.

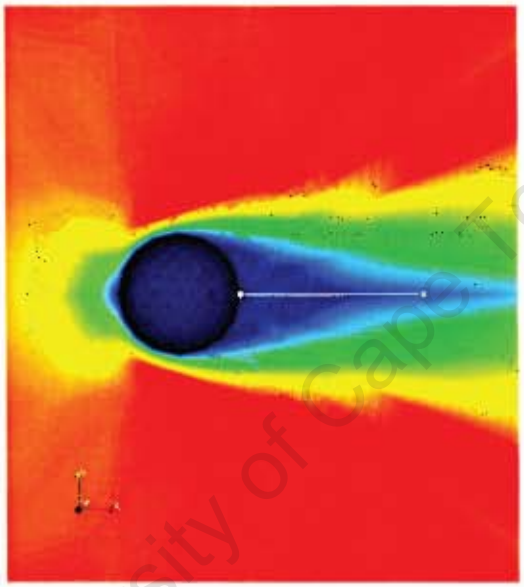

Figure 6.6: Velocity magnitude field with the white line indicating the domain used to plot the wake in Figure 6.7. The main flow direction is from left to right.

A number of wakelengths were measured for various Reynolds numbers ranging between 26.8 and 90, and these were plotted together with experimental data. In Figure 6.8, the dimensionless wake lengths calculated by dividing the wake length by the diameter of the sphere, are plotted against the Reynolds number. The experimental data obtained from Taneda (1956) was plotted using diamonds, squares and triangles, and the numerical result from the Navier-Stokes solver was plotted using circles. Note that the diameter of the sphere for the numerical calculations was $15mm$, which was within the range of the experimental diameters used. A positive result was that the dimensionless wake lengths for the different sized spheres all appeared to fit onto the same line with Re, which meant that the length of the wake was directly proportional to the diameter of the sphere.

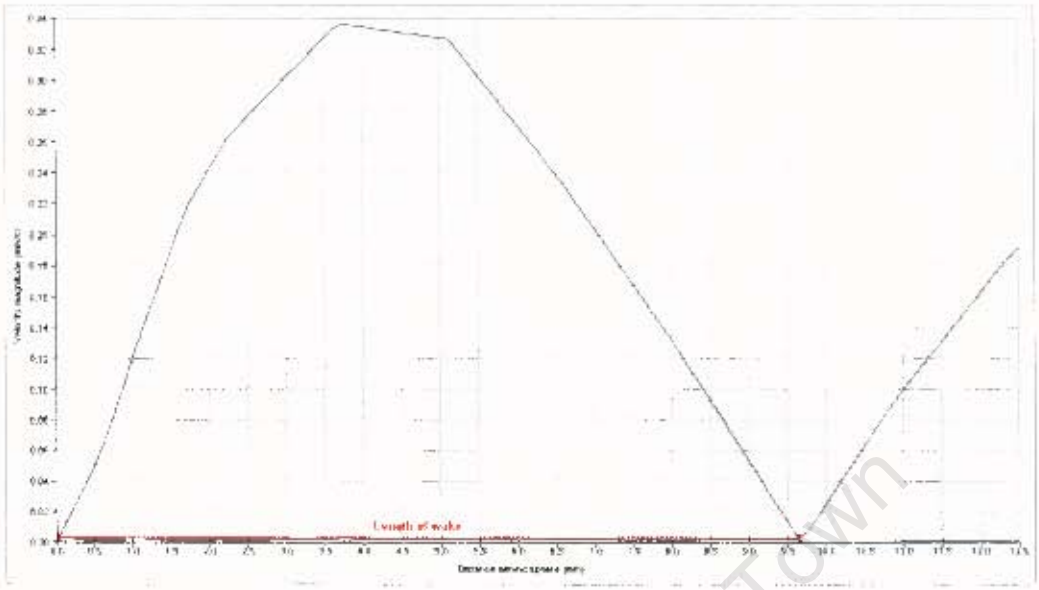

Figure 6.7: Plot of the velocity magnitude profile behind the solid sphere to determine the wake length for a Reynolds number of 73.6.

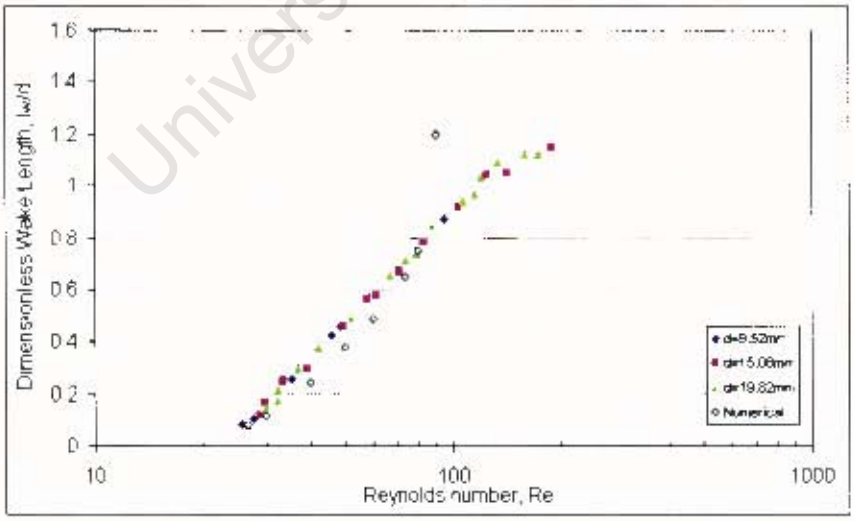

Figure 6.8: Plot of the dimensionless wake lengths with the Reynolds number for various sized solid spheres and a numerical calculation.

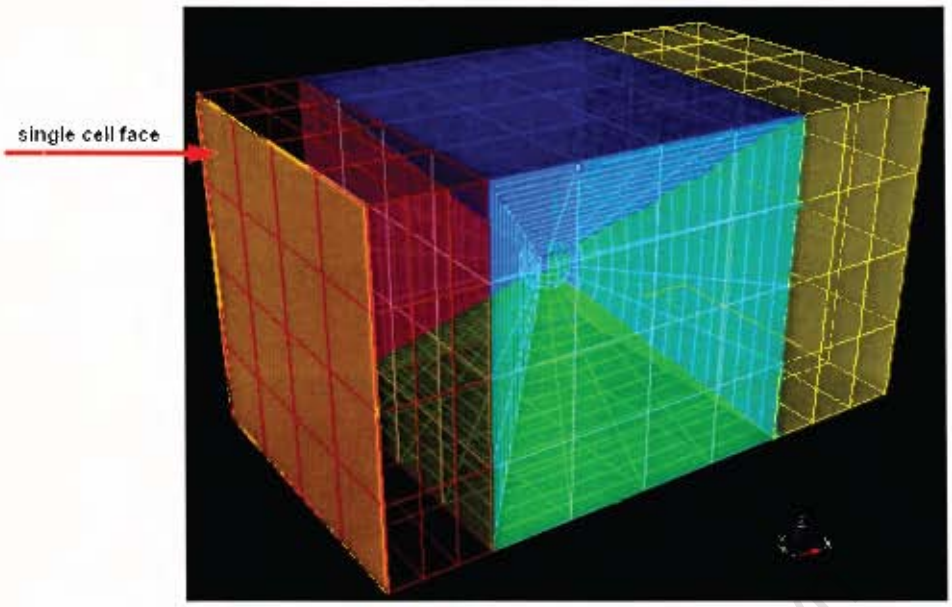

Figure 6.9: Indication of a cell face with a red arrow for which the mass flow is calculated. This was performed for each cell face that is positioned on the outside of the domain.

The numerical data obtained from the Navier-Stokes flow solver was in close agreement with the experimental data, up to a Reynolds number of 80. The plot which used a log scale for the Reynolds number produced a straight line for all data sets, excluding the numerical result at a Re of 90. The data from the Navier-Stokes solver produced a line with the same gradient compared to the experimental results, although at the highest Reynolds number the dimensionless wake length deviated with a larger value.

6.5 Mass Balance

To lend further credibility to the quantitative validation, a mass balance was performed over the domain to ensure that the net flux over the simulation space was zero. This was done for the steady state solutions for the flow around a solid sphere at a Reynolds number of 73.6. Simulations were performed using both the Stokes flow solver and the Navier-Stokes flow solver. The mass flow rate through each face of the rectangular domain was calculated by the post processing software, Paraview. Figure 6.9 shows the meshed geometry with the flow inlet face coloured in orange. The red arrow points to the face of an individual cell.

The total flow through one of the sides of the domain is given in equation (6.1).

$$F_T = \sum_{i=1}^{n_{cells}} v_{n,i} A_i \rho \tag{6.1}$$

In eq. (6.1), $F_T\,[mg/s]$ is the total flow through the side of the domain, $v_{n,i}\,[mm/s]$ is the average normal velocity of the cell face, $A_i\,[mm^2]$ is the area of the cell face and ρ is the density of the fluid which is 1 mg/mm^3. The total flow through each side was calculated. The overall relative error is given in equation (6.2).

$$Err = \frac{F_{T,in} - F_{T,out}}{F_{T,in}} \times 100\% \tag{6.2}$$

Table 6.1 gives the relative errors for different mesh sizes. These errors are all well below 1%. The table shows a slight trend of decreasing error with increasing refinement for both solvers. Generally speaking, mass flow rate was considered to be suitably conserved over the simulation domain for the purposes of the investigation in this thesis.

Table 6.1: Mass balance results for different mesh sizes.

	Percentage error	
Mesh size (cells)	Stokes solver	Navier-Stokes solver
1536	7.16x10^{-4}%	0.209%
1984	5.17x10^{-4}%	0.208%
3720	5.18x10^{-4}%	0.206%

6.6 Summary

The validation of the Navier-Stokes simulation for the flow past a solid sphere was reported in this chapter by observing the changes in the flow field around the sphere at different Reynolds numbers. By comparison with published experimental data, it was shown that the solver predicted the correct flow fields at Reynolds numbers of 26.8 and 73.6, as well as demonstrated similar trends in the variation of the wake length with Reynolds number. Furthermore, surface domain integration showed that the mass balance was closed subject to suitably low errors. The Navier-Stokes solver was therefore considered to be sufficiently accurate for the purpose of testing the Stokes flow solver up to a Reynolds number value of 80.

We note also that flow past a solid sphere, in which case a no-slip boundary condition must be imposed on the sphere, involves a discontinuity in the solution. On the other hand, flow past a bubble, for which the free-slip condition applies, solves far more easily. We can therefore with confidence assume that the restrictions arising from the solid sphere simulations are a sufficiently conservative set to be applied in the case of bubbles.

This approach is necessary because there is not equivalent experimental data available for bubbles.

This exercise therefore justifies the approach adopted in the remainder of this thesis with the end goal being to find the Reynolds number range where the Stokes solver could be used to accurately predict the flow around both the solid sphere and the bubble. These results are presented in the following chapter.

Chapter 7

Results

In this chapter, we attempt to gauge accuracy of the Stokes solution by observing how far it departs from the solution predicted by the Navier-Stokes equations as a function of Reynolds number. Analyses are carried out for both flow around a solid sphere and flow around a bubble. The NVS solution, which, according to the validation presented in chapter 6 can be accepted as a sufficiently accurate benchmark was compared with the Stokes solution. As the Stokes velocity field was compared with the NVS velocity field, the error analysis was split into two parts. Firstly, the relative difference between both solution fields based on the velocity magnitude was determined and regarded as the magnitude error in the Stokes solution. Secondly, the average angle between vectors at corresponding nodes for the Stokes and NVS solution fields was determined as the angular error. This approach was chosen to avoid calculating the relative error of the individual velocity components, because some components particularly in the y and z directions were close to zero, which forced the relative error to be extremely large. By calculating relative errors using the velocity magnitudes and determining the angles between the vectors, all components of the solution data were used in the analysis. By determining the Reynolds range over which the Stokes solution is accurate enough, this will effectively be a way to partition the solution domain in a real reactor.

In Figures 7.1 and 7.2 the NVS and Stokes velocity magnitude fields are shown for a *Re* of 75. In these simulations the mesh was refined twice using the Stokes refinement algorithm explained in chapter 4. Both NVS and Stokes simulations used a mesh consisting of 3720 cells with identical BC's. These solutions represent the highest *Re* explored, thus also differ the most in the Reynolds number range. The essential difference between the NVS velocity field in Fig. 7.1 compared to the Stokes velocity field in Fig. 7.2 is that the velocities around the bubble are higher and a long, low velocity 'tail' exists on the RHS of the bubble for the NVS simulation. These differences may be attributed to

the convective term $\rho \mathbf{v} \cdot \nabla \mathbf{v}$ in the NVS momentum balance, which is not included in the Stokes momentum balance. This is also considered to be an inertial term as it contains the product of mass (due to ρ) and spatial acceleration of the fluid.

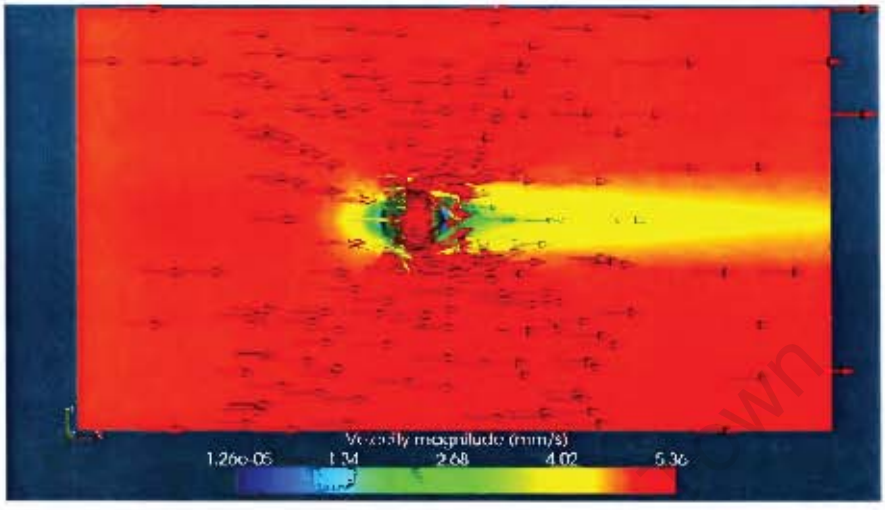

Figure 7.1: Section of NVS velocity magnitude field for the flow past a bubble at a Reynolds number of 75.

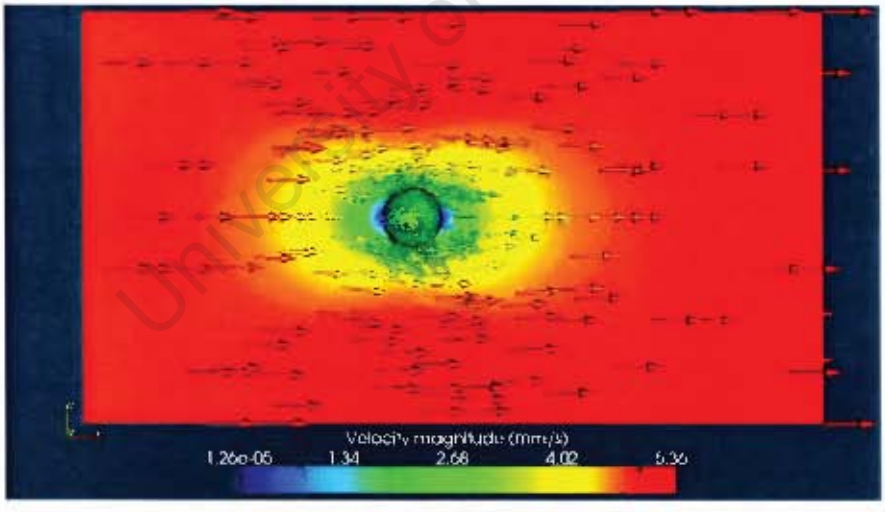

Figure 7.2: Section of Stokes velocity magnitude field for the flow past a bubble at a Reynolds number of 75.

7.1 Error Analysis

7.1.1 The Role of the Convective Term

In determining the cause of the error between the Stokes and the NVS solutions, the role of the convective term $\rho\mathbf{v} \cdot \nabla\mathbf{v}$ in the NVS momentum balance with respect to the flow field is established. Firstly, at high Reynolds numbers ($Re = \frac{DU}{\nu}$) the free stream fluid velocity U is typically high and at low Re the free stream velocity is low. The convective term contains the dot product of the velocity $\mathbf{v}$ and the gradient of the velocity $\nabla\mathbf{v}$.

In this specific case for flow around a bubble, the 'slip' BC imposed on the sphere surface means that the fluid flows smoothly around the bubble, and as a result there are no steep velocity gradients regardless of the value of Re. Thus the term $\nabla\mathbf{v}$ does not vary by orders of magnitude when Re is varied.

However for high values of Re the velocity is high, which means that the convective term is significantly large. At low Reynolds numbers the velocity is low, which means that the convective term is small. Thus at increasingly lower values of Re, the convective term in the NVS momentum balance approaches zero, which also means that difference between the NVS and Stokes solution should approach zero too.

7.1.2 Analysis Methods

The relative error between the NVS and the Stokes solutions was calculated at each node in the solution domain, using the velocity magnitudes. The relative error field between the Stokes and the NVS solutions is defined in equation (7.1).

$$err\,(x,y,z) = \frac{|\|\mathbf{u_{nvs}}\| - \|\mathbf{u_s}\||}{\|\mathbf{u_{nvs}}\|} \tag{7.1}$$

In equation (7.1), $\mathbf{u_{nvs}}$ and $\mathbf{u_s}$ are the NVS and Stokes velocity fields respectively and $\|\mathbf{u_{nvs}}\|$ and $\|\mathbf{u_s}\|$ are the NVS and Stokes velocity magnitude fields respectively. The volume-average relative error ϵ was calculated by volume integrating eq. (7.1) and dividing by the total volume, and is shown in eq (7.2).

$$\epsilon = \frac{\int_V err\,(x,y,z)\,\mathrm{d}V}{V_{total}} \tag{7.2}$$

The post-processing software Paraview was used to perform both calculations described by eq. (7.1) and eq. (7.2). In order to verify that the volume integration in equation

(7.2) was performed correctly, a known, constant relative error field was imposed, simulated, and compared to the value calculated by the Paraview software. The results were identical. The full test calculations are available in the Appendix.

The angle between the NVS velocity vector and the Stokes velocity vector at a node defined by Stewart (2001) is of the form eq. (7.3).

$$\theta_n = arccos\left(\frac{\mathbf{u_{nvs,n}} \cdot \mathbf{u_{s,n}}}{\|\mathbf{u_{nvs,n}}\|\|\mathbf{u_{s,n}}\|}\right) \tag{7.3}$$

The velocities $\mathbf{u_{nvs,n}}$ and $\mathbf{u_{s,n}}$ are the nodal NVS and Stokes velocity vectors respectively. The average angle between the NVS and Stokes solution field is given in eq. (7.4).

$$\overline{\theta} = \frac{\int_V \theta\,(x,y,z)\,\mathrm{d}V}{V_{total}} \tag{7.4}$$

Equation (7.4) gives the volume averaged error angle between corresponding NVS and Stokes solution vectors in the domain. A numerical challenge associated with equation (7.3) is that for the flow past a solid sphere, a zero velocity (no slip) BC is assumed on the sphere surface. Equation (7.3) calculated the NVS and Stokes vectors to be perpendicular on the sphere surface, despite their velocities each being zero, thus introducing a 0.05% error in the overall calculation of $\overline{\theta}$ for Re=30. This error calculation is available in the appendix.

7.1.3 The Error Domain

It was found that significant error between the Stokes and NVS solutions was only present in the region immediately adjacent to the sphere and in the wake, for both the flow around the solid sphere and the bubble. For this reason, the error analysis was performed in these regions specifically and not over the entire solution domain. Figure 7.2 and Figure 7.1 presented in the beginning of this chapter show sections of the Stokes and NVS velocity magnitude fields respectively, for flow around a bubble at a Re of 75. The NVS flow solution contains high velocities around the sphere and low velocities in the wake, which is not the case in the Stokes flow solution. Figure 7.4 is a section of the relative error field between these solutions. In this error field, dark blue indicates zero error and red indicates a relative error of 65%, thus confirming the regions discussed above. The relative error field for the flow around a bubble at a Re of 1 is shown in Figure 7.3, indicating a much lower error in the vicinity of the sphere and no error in the wake. This decrease in error with the decrease in Re is due to the convective term becomming less significant, which

is described earlier in section 7.1.1. Thus by volume integrating the relative errors over the entire solution domain, the resulting error will be diluted, thereby underestimating the degree to which the error will vary with Reynolds number. In order to prevent this, a subdomain was constructed over which the errors were calculated, based on the error field from Figure 7.4, which are the largest errors over the Reynolds number range of interest.

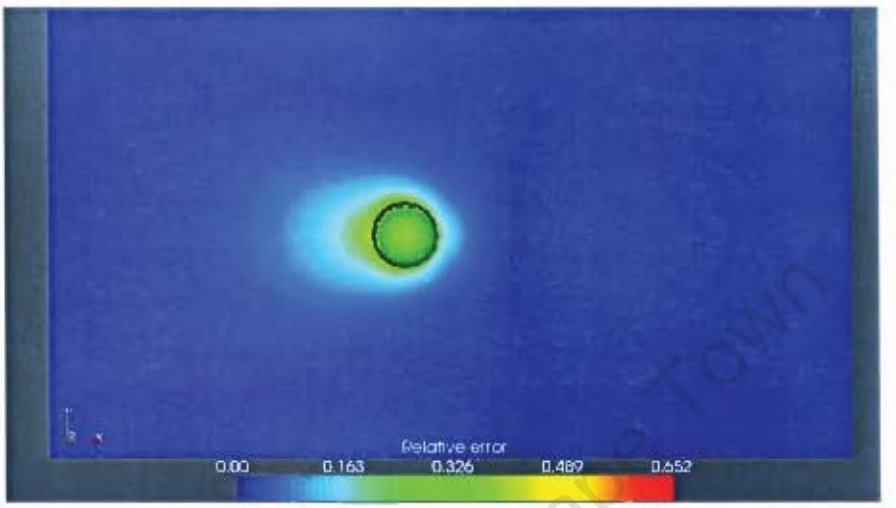

Figure 7.3: Section of relative error field for the flow past a bubble at a Reynolds number of 1.

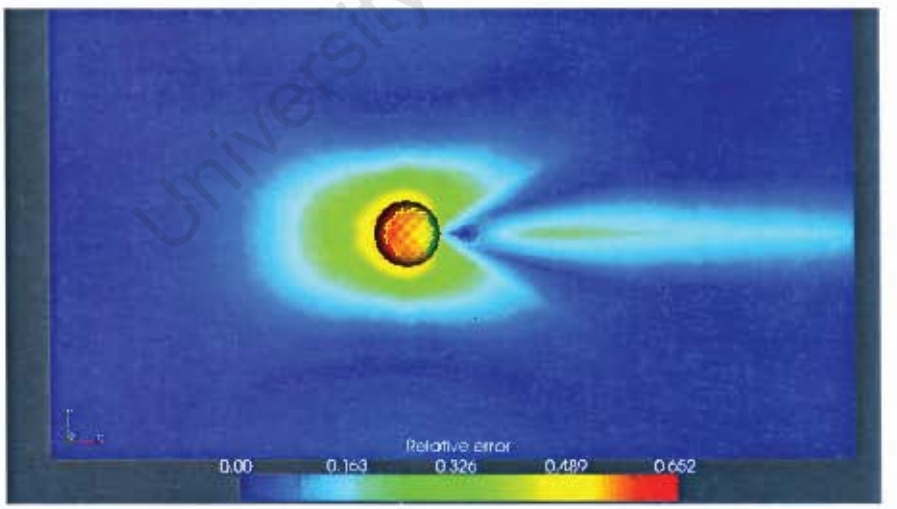

Figure 7.4: Section of relative error field for the flow past a bubble at a Reynolds number of 75.

The subdomain was sized with lengths of 1 bubble diameter (1D) left of the bubble, 4D behind the bubble on the wake side, 1D on either side of the bubble in the y-direction and 1D on either side of the bubble in the z-direction. Comparisons between the Stokes and NVS solutions for both flow around the bubble and flow around the solid sphere were made using this subdomain, which is illustrated in Figure 7.5. The white outline indicates the total size of the solution domain. The reason that the subdomain is not rectangular is due to the irregularly shaped mesh comprising of different sized cells (optimised for solution accuracy). The algorithm which generated the subdomain had flagged the cells to be included in the calculation if the co-ordinates of the center of the cell lay inside the subdomain, with cells positioned outside being excluded. An irregular edge in the domain was created when a larger cell was positioned directly alongside a smaller cell, with the one cell being flagged and the other cell excluded.

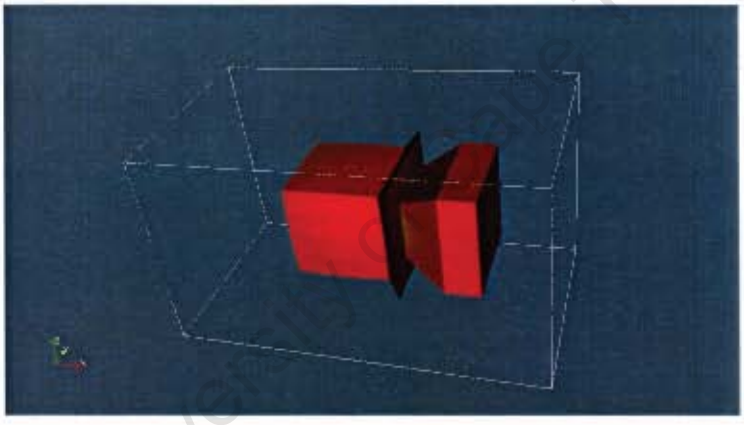

Figure 7.5: Subdomain over which the error analysis was performed.

7.2 Error Trends with Reynolds Number

The error trends with Re for the flow past a bubble are illustrated qualitatively in Figures 7.6 to 7.9 below. Figure 7.6 and Figure 7.7 show similar velocity fields for the NVS and Stokes simulations respectively at a Re of 1. At a higher Reynolds number of 20, the NVS solution illustrated in Figure 7.8 shows higher velocities around the bubble and a low velocity fluid wake behind the sphere, which the Stokes solution at the same Re does not predict. This Stokes solution is shown in Figure 7.9. At even higher Reynolds numbers, the convective term discussed earlier in this chapter in section 7.1.1 becomes more dominant in the NVS solution. This may be illustrated by Figure 7.1 presented in the beginning of the chapter for a Re of 75, where the fluid wake behind the bubble becomes

longer in the direction of the flow. The flow pattern for Stokes flow remains unchanged when Re is increased to 75, shown in Fig. 7.2.

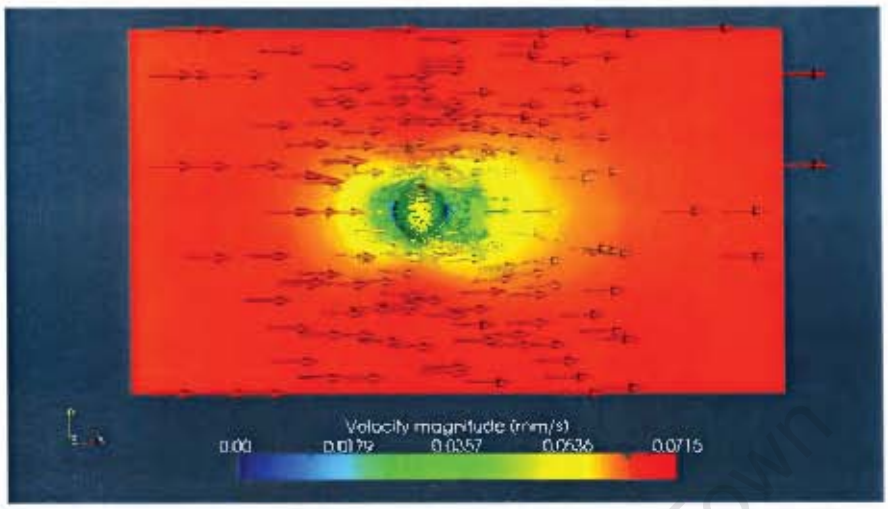

Figure 7.6: Section of NVS velocity magnitude field for the flow past a bubble at a Reynolds number of 1.

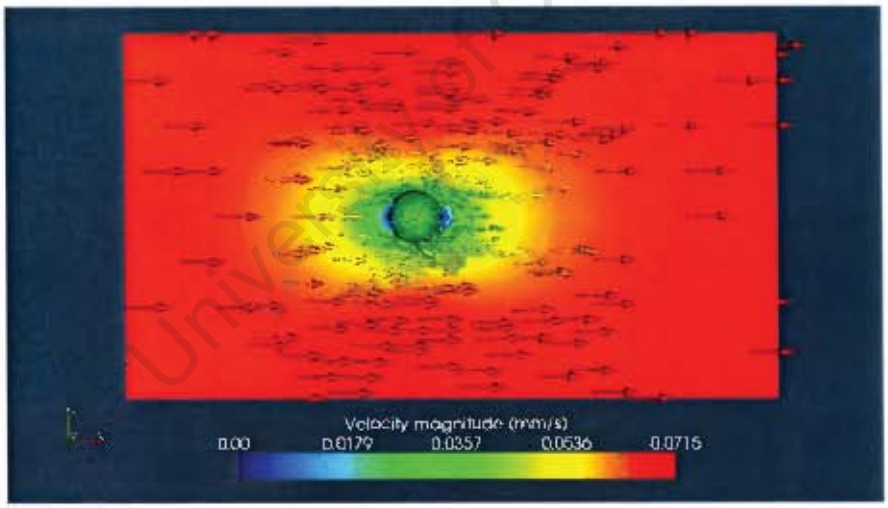

Figure 7.7: Section of Stokes velocity magnitude field for the flow past a bubble at a Reynolds number of 1.

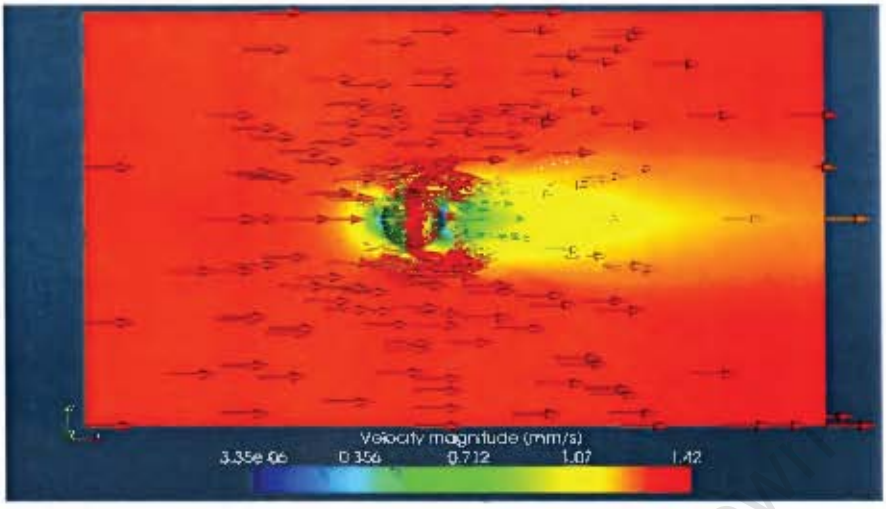

Figure 7.8: Section of NVS velocity magnitude field for the flow past a bubble at a Reynolds number of 20.

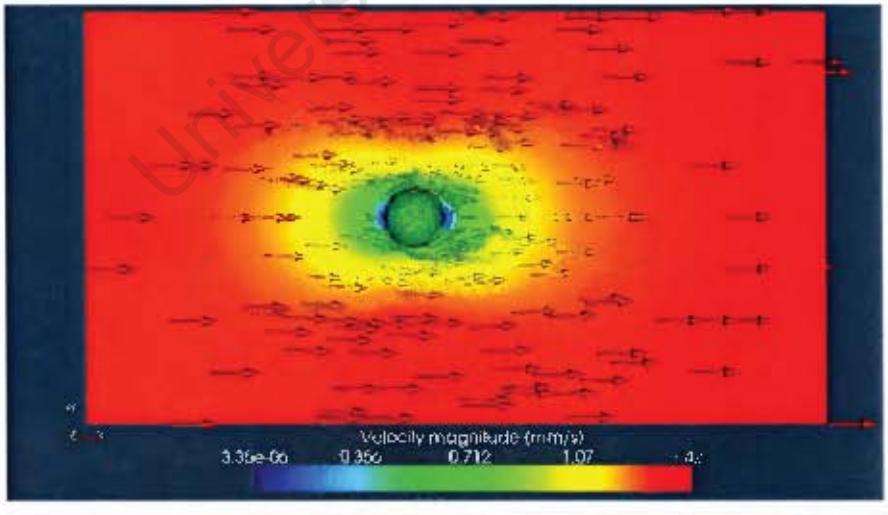

Figure 7.9: Section of Stokes velocity magnitude field for the flow past a bubble at a Reynolds number of 20.

The error results for the flow around a solid sphere are presented in Figure 7.10 and Figure 7.11, and analogous results for the flow around a bubble are shown in Figure 7.12 and Figure 7.13. The simulations which generated the NVS and Stokes velocity fields for which these errors were computed, used the refined mesh of 3720 cells. Figure 7.10 shows the increase in the volume averaged relative error with Reynolds number, and 7.11 shows a similar trend in the plot of volume averaged angle with Reynolds number. In the case of the bubble, Figure 7.12 shows the volume averaged relative error with Re, which increases sharply between $1 < Re < 20$. The volume averaged angle is plotted as a function of Re in Figure 7.13, and shows an identical trend to Figure 7.12.

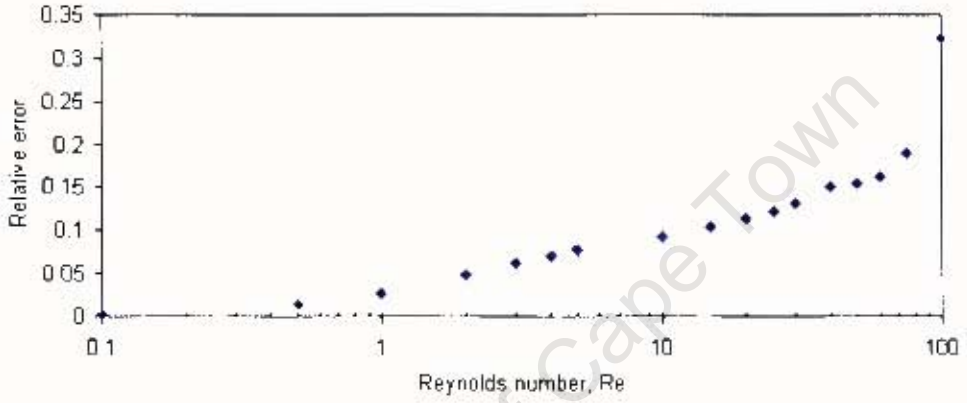

Figure 7.10: Plot of volume averaged relative error based on velocity magnitude against Reynolds number, for flow past a solid sphere.

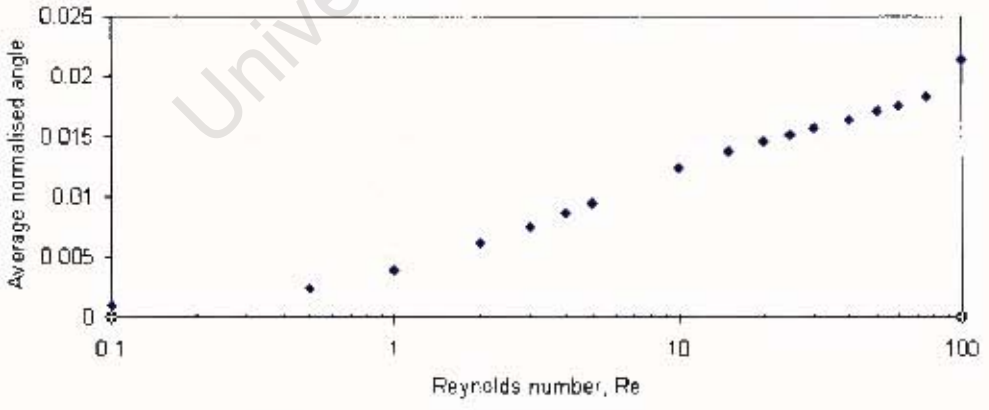

Figure 7.11: Plot of volume averaged angle between NVS and Stokes solution vectors against Reynolds number, for flow past a solid sphere.

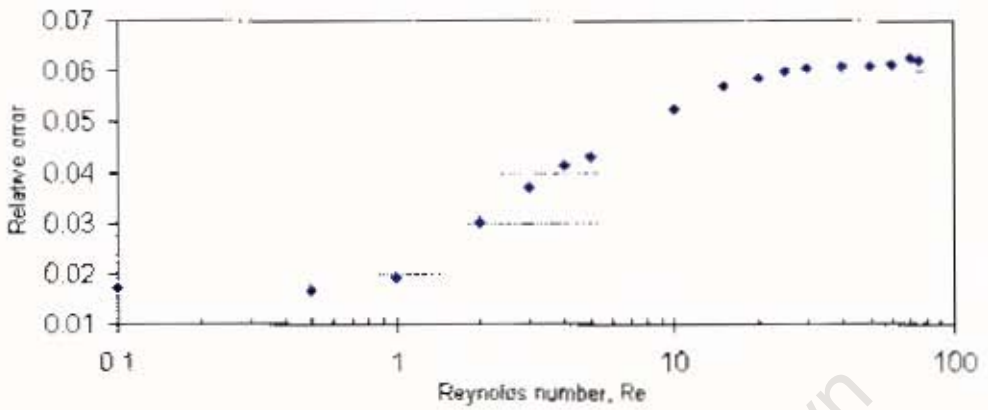

Figure 7.12: Plot of volume averaged relative error based on velocity magnitude against Reynolds number, for flow past a bubble.

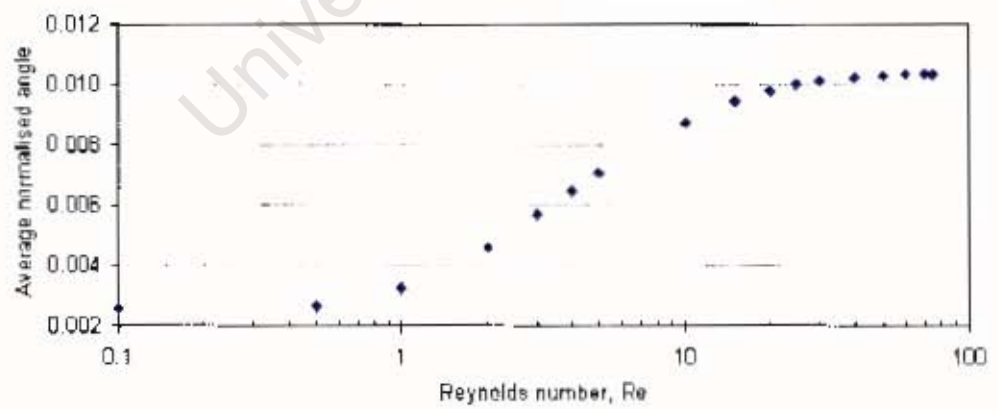

Figure 7.13: Plot of volume averaged angle between NVS and Stokes solution vectors against Reynolds number, for flow past a bubble.

In finding the error trends between the NVS and the Stokes solutions, this will provide sufficient information which may be used to choose either the steady NVS or the steady Stokes method for solving the fluid flow equations around a bubble, depending on the Reynolds number and acceptable error for the specific problem. In terms of a real bubble column, the solution domain may be partitioned by using the accuracy of the solver and Figure 7.12 and 7.13 above to determine the Reynolds number that should be used as the criterion for the partitioning. A discussion on these error trends will be presented in the next chapter.

Chapter 8

Discussion

When describing the flow of a fluid past a bubble using a mathematical model, ie. either the NVS or the Stokes model, a primary issue is the accuracy of the numerical result compared to the physically observed flow field. In Chapter 6, it was shown that the NVS model predicted the flow of water around a solid sphere for the Reynolds number range of interest, to some degree of error, where experimental data was used in the comparison. Additional error between the numerical solution and the physical flow field creeps in when the Stokes model is used, due to its assumption of zero convective flow.

In the finite element method, the FEM solution should converge to the exact solution as the number of computational cells in the domain increases to infinity. Due to a FEM problem containing a finite number of elements, there is always some error between the FEM solution and a hypothetical perfect solution, which is highlighted in Figure 8.1 by Error 5. The value of Error 5 depends on the FEM code used, such as the choice of finite element, preconditioner, solver, etc. The FEM code for the 3-D incompressible NVS solver had been validated against the analytical solution for Beltrami flow, where the unsteady term balances the viscous term and the convective term balances the pressure term (Etheir and Steinman, 1994). Errors 1 to 4 will be discussed in this chapter, with the focus on finding the solution which minimises the computational time required to solve the problem whilst still maintaining suitable accuracy.

However, the focus of this study was not to improve the performance of the existing NVS model, but rather to propose a model which predicted the flow field around a bubble with the same accuracy as the NVS model, with less computational expense.

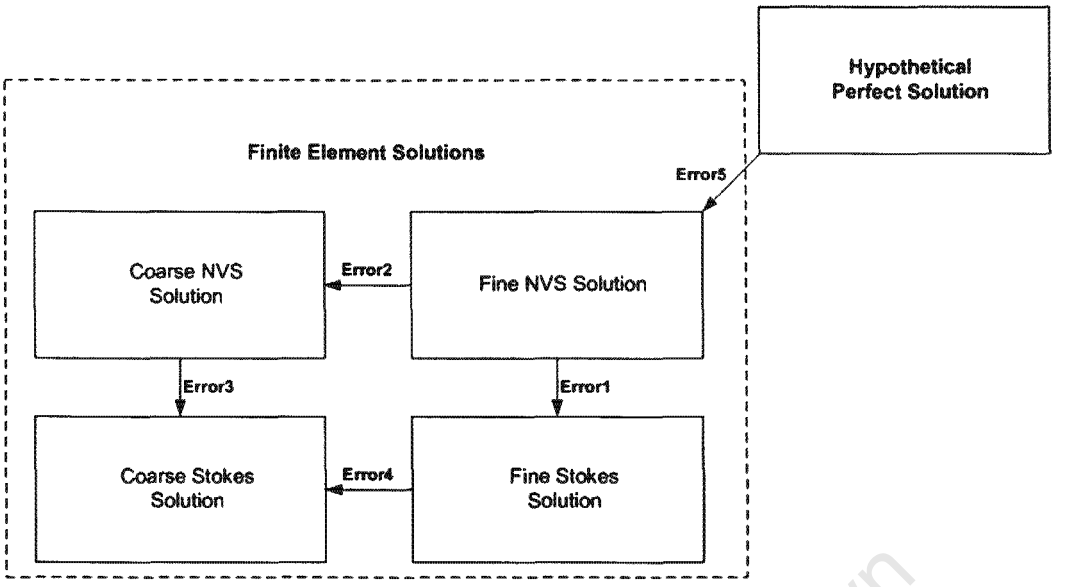

Figure 8.1: Diagram showing the different errors between the various FEM solutions obtained.

8.1 Error Analysis on the Bubble

8.1.1 Comparison between the NVS and the Stokes Solutions

The errors between the NVS and the Stokes solutions as a function of Re presented in Chapter 7, Section 2, are shown in Figures 8.2 and 8.3, which include plots of both the coarsest and the finest meshes used on the same axes. Thus the error introduced by using a coarser mesh instead of a finer one was determined. Graphs of both the relative error based on velocity magnitude and the average angle are used in the analysis.

Figure 8.2 shows the increase in relative error between the NVS and the Stokes solutions, which is apparent for both the coarse mesh of 1536 cells and the fine mesh of 3720 cells. Below a Reynolds number of 1, relative errors are typically below 2% while for $1 < Re < 30$ the errors increase from 2% to 6%. As the Re is increased further, the error appears to increase slightly. This error may be attributed to the low velocity 'tail' region behind the bubble which the NVS solver predicts but the Stokes solver does not. This graph shows the expected trend that the error increases with increasing Reynolds number, because the convective term from the NVS momentum balance becomes increasingly important. The role of the convective term is summarised in chapter 7.1.1.

Above a Reynolds number of 30 the error seems to saturate. This may be due to the

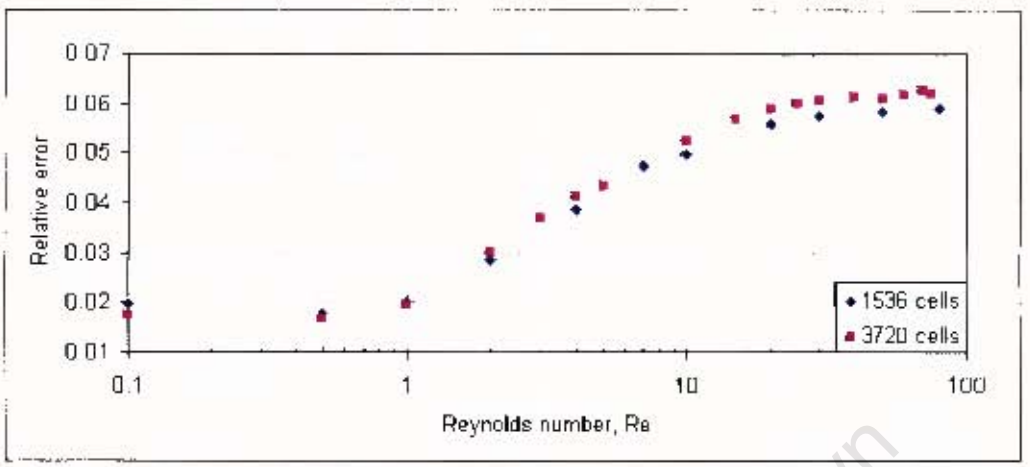

Figure 8.2: Plot of volume averaged relative error based on velocity magnitude against Reynolds number, for flow past a bubble, using both the finest and the coarsest meshes.

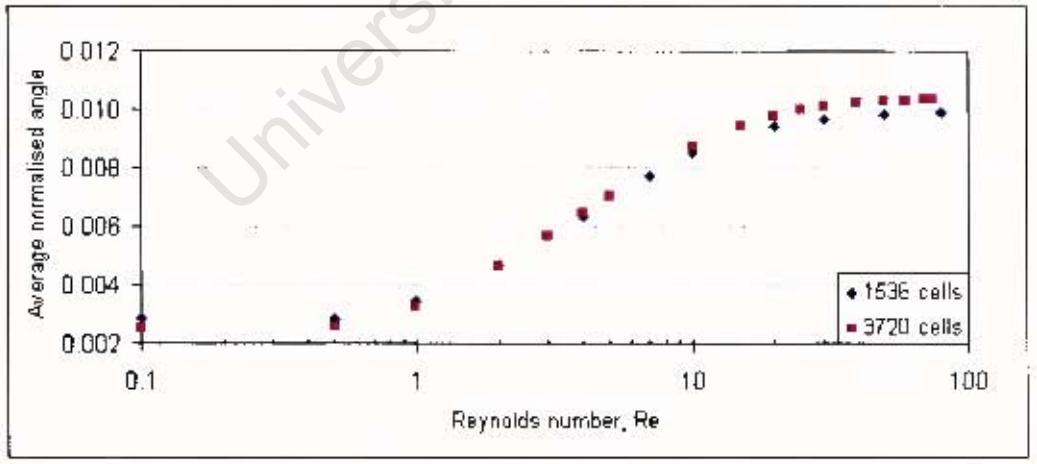

Figure 8.3: Plot of volume averaged angle between NVS and Stokes solution vectors against Reynolds number, for flow past a bubble, using both the finest and the coarsest meshes.

low velocity region behind the sphere increasing in length with Re, and actually exceeding the length of the error domain. As this low velocity region is a primary source of error because it does not exist in the Stokes flow simulations, it may be the cause of the saturation. In terms of the NVS and Stokes equations, there is too much uncertainty about how the terms behave in the very high Re region and the region of interest is where the error is between 1-2% anyway.

In a similar manner to the analysis on the relative errors above, the errors on the angles were also taken into account. Figure 8.3 shows this for both the coarse mesh and the fine mesh. Again the general trend was a steep rise in the average angle for $1 < Re < 30$. This trend was identical to that found in Figure 8.2, where the relative error was plotted with Re. Finally the effect of mesh size on the average angles was found to be negligible. These observations from Fig. 8.3 are consistent with those found in Figure 8.2, meaning that an increase in magnitude error was always accompanied by an increase in angle between the NVS and Stokes solutions. By taking into account both the errors with respect to the velocity magnitude and the direction, every component of the solution data was analysed.

Another point to consider is that the volume averaged error is a function of the size of the constricted error domain, and decreases with increasing size if the error is significant in only a small volume of the overall domain. However, if the constricted domain is too small, then important differences between the two solutions would not be included in the calculation. Thus according to the information presented in Chapter 7, Section 1.2, the error domain was a sufficient size over which the volume integrated errors were calculated.

It is important to note that the size of the error domain affects the magnitude of the errors, since the further away the boundary lies from the sphere (around which the error is concentrated), the lower the volume-averaged error will be. However, the specific error domain size used was suitable for the purpose of implementing the results in a larger model framework as the region of interest was the volume in the vicinity of the bubble. The error domain was increased until it incorporated all significant error, and this domain was fixed for all further calculation of error. By still enlarging this domain, the volume averaged relative errors would decrease, but the error trend would remain the same over the range of Re. If the error domain was made smaller, then the results would not accurately represent the error between the NVS and Stokes solutions.

In summary, the data plotted for 3720 cells (fine mesh) in Fig. 8.2 and Fig. 8.3 rep-

resents Error 1, illustrated in Figure 8.1, and the data plotted for 1536 cells (coarse mesh) represents Error 3. Thus Error 1 is approximately equal to Error 3 for the Reynolds number range of interest. The importance of this result will be discussed further on, and Errors 2 and 4 will be determined in the next subsection.

8.1.2 Refinement Errors

In this subsection the solutions determined using meshes of 1536 cells and 3720 cells are compared for each of the NVS and Stokes solutions. This corresponds to Error 2 from Figure 8.1 for the NVS solutions and to Error 4 for the Stokes solutions. Unlike the comparison between the NVS and Stokes solutions which resulted in Errors 1 and 3, a volume averaged error was not calculated. Instead, the velocity magnitude profile was plotted over two lines in the 3-D domain space, together which represented the most important flow trends. This was done because a direct comparison between the two solutions was not possible as the comparison involves calculating the relative errors at each node in the computational domain. As different sized meshes were used in the simulations, a different number of nodes existed in each mesh. Figure 8.4 shows the two lines, where Line 1 is parallel to the bulk flow direction from left to right and runs directly through the center of the bubble, and in the wake. Line 2 is positioned $7.5mm$ behind the bubble, perpendicular to the main flow direction, along the y-axis. Significant fluid velocity gradients in the y-direction occur around the bubble, which are identical to those in the z-direction as the solution is symmetrical about Line 1. Both Lines 1 and 2 are positioned in the middle of the domain with respect to the z-axis.

Comparisons between the NVS and Stokes solutions for different mesh sizes are shown in Figures 8.5 to 8.8, where each graph contains the velocity magnitude plot for each of the three different sized meshes used, namely those containing 1536, 1984 and 3720 cells. The graphs show these results at a Reynolds number of 15, although the same plots were produced at a Re of 1, which showed identical trends, and are not shown. Additional plots at higher Reynolds numbers were not made as the relative errors from Fig. 8.2 and Fig. 8.3 did not increase substantially above a Re of 20, thus the range of interest over which the error increased was covered.

In Figure 8.5, the velocity magnitudes are plotted along Line 1 for a Re of 15, and the solution for the mesh of 1536 cells is drawn in black, whilst the solutions for the meshes of 1984 cells and 3720 cells are drawn in red and blue respectively. The red and blue lines show almost identical solutions, while the black line is slightly above the other two in the region behind the bubble, which shows that the mesh was refined until the solution no

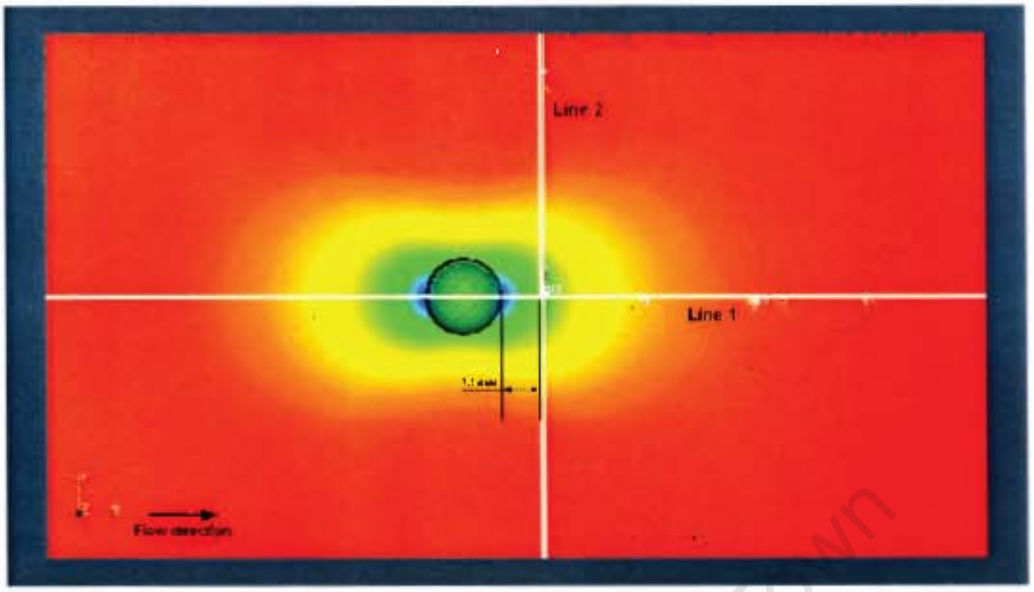

Figure 8.4: Illustration showing the two lines over which the velocity magnitudes were plotted.

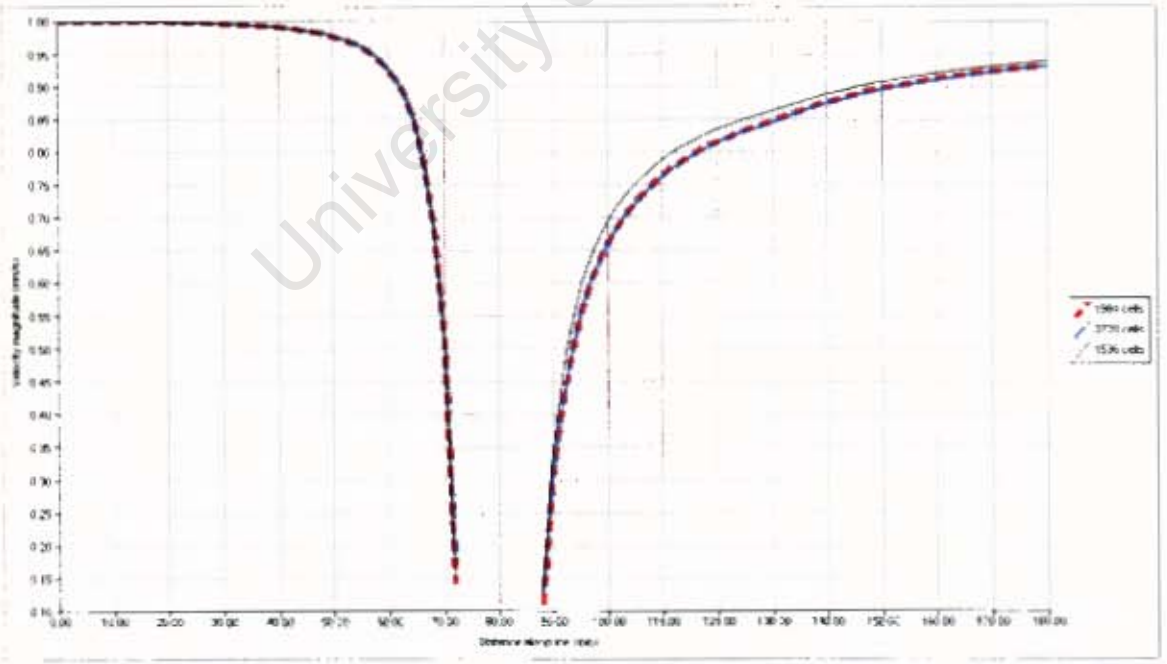

Figure 8.5: Plot of NVS velocity magnitude along Line 1, for the flow around a bubble at Re=15.

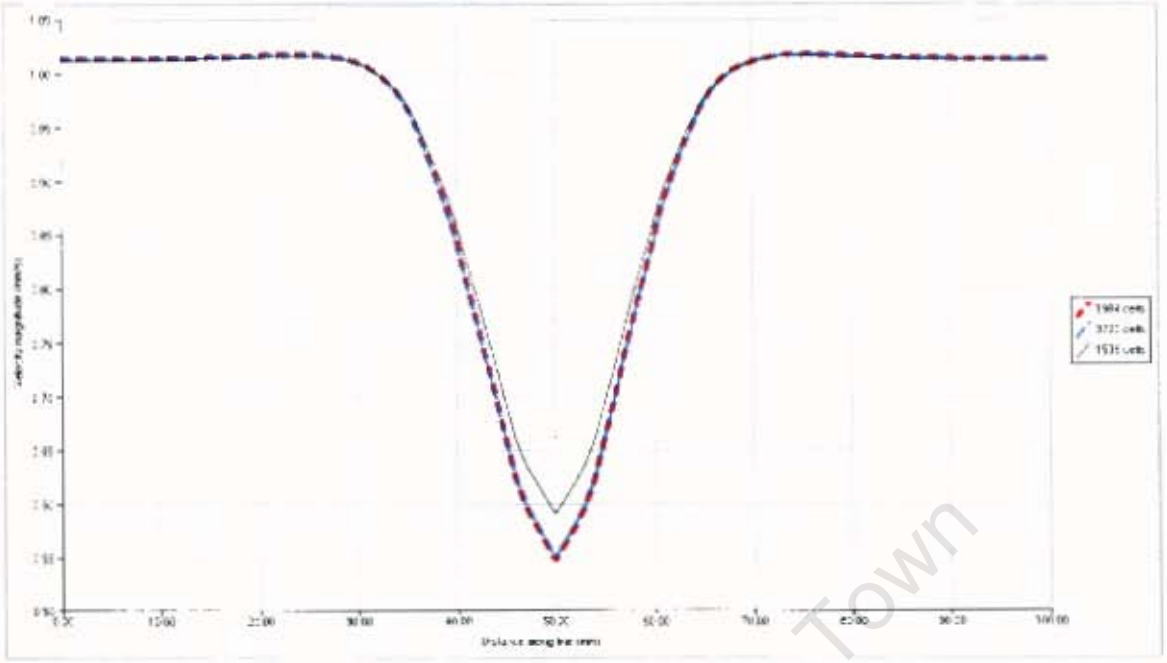

Figure 8.6: Plot of NVS velocity magnitude along Line 2, for the flow around a bubble at Re=15.

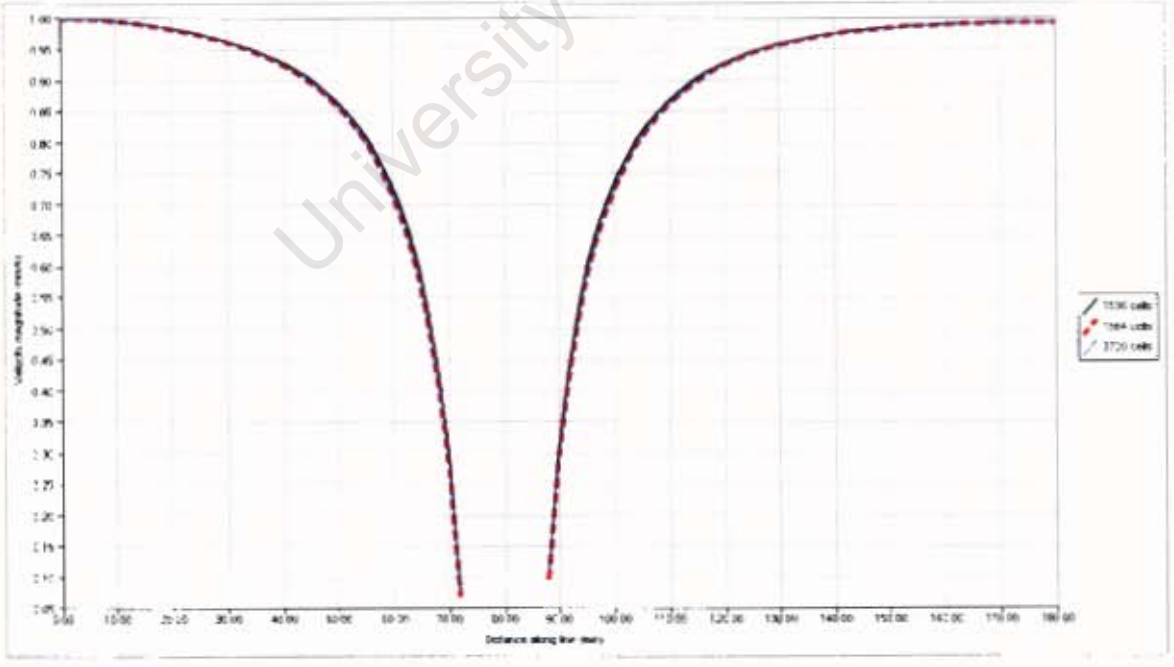

Figure 8.7: Plot of Stokes velocity magnitude along Line 1, for the flow around a bubble at Re=15.

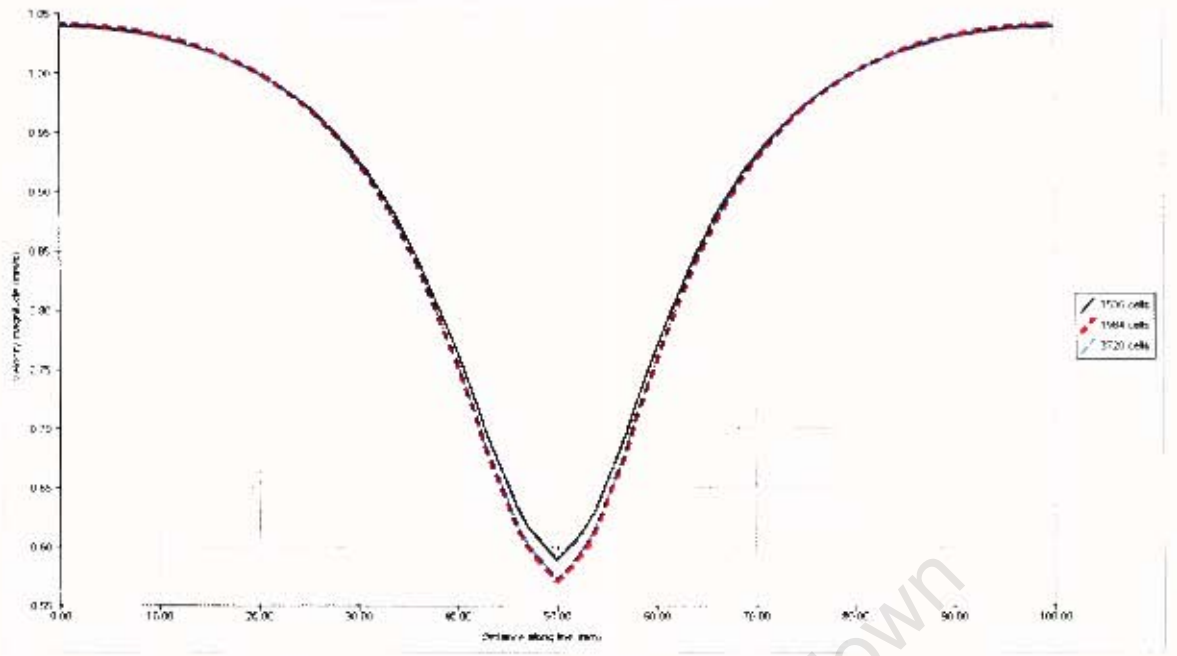

Figure 8.8: Plot of Stokes velocity magnitude along Line 2, for the flow around a bubble at Re=15.

longer changed, hence we may assume that adequate refinement was implemented. The maximum deviation of the solution generated using the coarsest mesh compared with the solution generated using the finest mesh (relative error) was 2.5%. These observations show that Error 2 from Figure 8.1 is small but significant.

In Figure 8.6, the velocity magnitudes were plotted over Line 2 for the same Re and similar trends were observed. These trends also showed convergence of solution as the mesh was refined twice, with a 7% maximum relative error, hence confirming the significant error (Error 2) from Figure 8.1. Finally, Fig. 8.7 and Fig. 8.8 are analogous to Fig. 8.5 and 8.6 for the NVS comparisons respectively, although show the Stokes results. The maximum relative error for Line 1 is 1%, and is 4% for Line 2. This means that the Stokes coarse and fine solutions are slightly different, and that Error 4 from 8.1 is somewhat significant. In addition, the maximum relative error found at a Re of 1 for the Stokes solution was 20%, which means that Error 4 is fairly large. As the solutions which were generated using meshes of 1984 cells and 3720 cells were almost identical for each of the above mentioned cases, including at a Re of 1, and considering that the lines over which these solutions were plotted represented the important trends, it is fair to conclude that a mesh size of 1984 cells was sufficient to calculate the solution, and that using the mesh of 3720 cells results in an unnecessary computational expense.

8.2 Computational Requirements

In order to determine the increase in computational speed by solving the Stokes equations compared with the NVS equations, varying mesh sizes and Reynolds numbers were tested using both the Stokes and NVS programs for the flow around a bubble. These simulations were run on the Chimera cluster, using a 2.2 GHz processor and 8 Gb of RAM. Additional NVS programs were run using multithreading, where the assembling of the matrix equations was performed on four of the 2.2 GHz processors simultaneously, so that the effect of multiple CPU use was determined. Table 8.1 gives the computational times using different mesh sizes, for both the Stokes and the NVS solvers at a Reynolds number of 1.

Table 8.1: Computational times for flow around a bubble at a *Re* of 1.

	Computational time		
Mesh size (cells)	Stokes solver	NVS solver (1 CPU)	NVS solver (4 CPU's)
1536	49s	1h 1min 41s	44min 57s
1984	1min 2s	1h 30min 31s	1h 8min 46s
3720	2min 5s	3h 15min 4s	2h 31min 39s

The most significant trend in Table 8.1 is that the NVS equations take two orders of magnitude longer to solve compared with the time required to solve the Stokes equations. This is true for each of the different mesh sizes. The NVS solutions using 4 CPU's are obtained in approximately 75% of the time required to solve using only 1 CPU. Finally, as the refinement of the mesh increases, the calculation times increase. Table 8.2 represents analogous data to table 8.1, for a Reynolds number of 15. Identical trends to those found in table 8.1 were observed, namely an approximate 25% decrease in the computational time when multithreading was implemented, a significant difference in computational time for the Stokes algorithm compared with the NVS algorithm, and an increase in computational time with mesh refinement.

Table 8.2: Computational times for flow around a bubble at a *Re* of 15.

	Computational time		
Mesh size (cells)	Stokes solver	NVS solver (1 CPU)	NVS solver (4 CPU's)
1536	44s	1h 16min 29s	54min 39s
1984	1min 1s	2h 15min 43s	1h 39min 58s
3720	2min 7s	4h 16min 9s	3h 08min 06s

It is clear the steady NVS solution required a much greater computational time to solve compared with the steady Stokes solution, so that in simulating the steady flow around a bubble, the Stokes flow approximation would significantly save computational power. Although the unsteady state NVS equations were solved, and the solution was allowed to converge to a steady solution which significantly added to the computational time, this approach was justified because an accurate steady solution may be calculated by stepping forward in time in small time increments. Even though the Stokes solutions only apply when the Reynolds number is less than 1, there is significant value in modelling the flow around bubbles at these values of *Re*. If this low velocity region occupies 20% of the bubble column, then this study shows that the computational time is reduced by effectively 20%.

From the data presented, the Stokes flow solutions at a Reynolds number of less than 1 are accurate and do not require a great deal of computational time. In addition, accurate solutions are obtained for both the Stokes and NVS algorithms using the intermediate mesh size of 1984 cells, so computational time was saved by not using the fully refined mesh.

Chapter 9

Conclusions

In this work a fundamentally different approach was used in developing a bubble column model. A "cell" model was constructed which was used to calculate the flow of water past a bubble. This model may be incorporated into a larger framework such as a population balance model with the purpose of using less computational power in solving for the hydrodynamics of the whole bubble column reactor. However the focus of the study was on the analysis of the Reynolds number range where the Stokes equations could be used to predict the velocity field in the vicinity of the bubble instead of the full NVS equations.

It was found that the simulation results from the "cell" model for the flow of water past a solid sphere when solving the NVS equations were in good agreement with experimental data for the Reynolds number range of 25 to 80. The Stokes model only predicted similar velocity fields to the NVS model at low Reynolds numbers, typically below 1. As the Reynolds number was increased, the Stokes solution deviated further from the NVS solution. The Stokes solution failed to predict the circulating eddies and backmixing which developed behind the solid sphere at Reynolds numbers above 40.

For the flow of water past a bubble, the Stokes flow model produced very similar flow fields to the NVS flow model at Reynolds numbers below 1, where the NVS flow field was determined to be correct. At higher Reynolds numbers, the Stokes flow model did not predict the high velocities on the bubble surface and the low velocity region or wake behind the bubble. Such phenomena were observed when the NVS flow equations were solved, thus it was concluded that the convective term in the NVS equations is needed in order to predict these. The relative error based on the velocity magnitude was less than 2% for Reynolds numbers less than 1 and increased to 6% for Reynolds numbers greater than 20.

The computational time required to solve the NVS equations for the flow around the bubble was considerably greater than that required to solve the Stokes equations, where the NVS flow solver took two orders of magnitude longer. As the number of computational cells doubled, the computation time increased by a factor of approximately two.

Finally, the error analysis performed in this work may be used to partition a bubble column into regions governed by the Stokes equations with the remainder of the column governed by the NVS equations, which would help reduce the computational load. The movement of bubbles in clusters in the column may provide another opportunity to use the Stokes model as the relative velocity of the bubbles is such that very low Reynolds numbers are observed.

Bibliography

Anderson, D. A., Tannehill, J. C., Pletcher, R. H., 1984. Computational Fluid Mechanics and Heat Transfer. Hemisphere, New York.

Bangerth, W., Hartmann, R., Kanschat, G., 2007. deal.II — A general-purpose object-oriented finite element library. ACM Transactions on Mathematical Software 33 (4), article 24.

Becker, S., De Bie, H., Sweeney, J., 1999. Dynamic flow behaviour in bubble columns. Chemical Engineering Science 54, 4929–4935.

Becker, S., Sokolichin, A., Eigenberger, G., 1994. Gas-liquid flow in bubble columns and loop reactors: part II. Comparison of detailed experiments and flow simulations. Chemical Engineering Science 49, 5747–5762.

Belytschko, T., Fish, J., 2006. A First Course in Finite Elements. Wiley.

Bennett, C. O., 1962. Momentum, Heat and Mass Transfer., 6th Edition. McGraw-Hill, New York.

Bohr, T., Jensen, M. H., Paladin, G., Vulpiani, A., 1998. Dynamical Systems Approach to Turbulence. Cambridge University Press.

Brennen, C. E., 2005. Fundamentals of Multiphase Flow. Cambridge University Press.

Buffler, A., 2007. Introduction to fluid mechanics, Lecture Notes, Fields and Fluids, University of Cape Town.

Chen, R. C., Reece, J., Fan, L. S., 1994. Flow structure in a three-dimensional bubble column and three-phase fluidized bed. AIChE Journal 40 (7), 1093–1104.

Cliffe, K. A., Lever, D. A., 1986. A comparison of finite-element methods for solving flow past a sphere. Journal of Computational Physics 62, 321–330.

Clift, R., Grace, J. R., Weber, M. E., 1978. Bubbles, Drops and Particles. Academic Press, New York.

Cook, T. L., Harlow, F. H., 1986. Vortices in bubbly two-phase flow. International Journal of Multiphase Flow 12, 35–61.

Crowe, C., Sommerfeld, M., Tsuji, Y., 1998. Multiphase Flows with Droplets and Particles. CRC Press.

Delnoij, E., 1998. Fluid dynamics of gas-liquid bubble columns. A theoretical and experimental study. Ph.D. thesis, University of Twente, The Netherlands.

Etheir, C. R., Steinman, D. A., 1994. Exact fully 3d Navier-Stokes solutions for benchmarking. International Journal for Numerical Methods in Fluids 19, 369–375.

Fan, L. S., Tsuchiya, K., 1990. Bubble Wake Dynamics in Liquids and Liquid-Solid Suspensions. Butterworth.

Geankoplis, C. J., 2003. Transport Processes and Separation Process Principles., 4th Edition. Prentice Hall, New Jersey.

Hamielec, A. E., Johnson, A. I., Houghton, W. T., 1967. Viscous flow around circulating spheres of low viscosity. AICHE Journal 13 (2), 220–224.

Heath, M. T., 2002. Scientific Computing. An Introductory Survey., 2nd Edition. McGraw-Hill, New York.

Hirt, C. W., Nichols, B. D., 1981. Volume of fluid (VOF) method for the dynamics of free boundaries. Journal of Computational Physics 39, 201–225.

Hoomans, B. P. B., Kuipers, J. A. M., Briels, W. J., Van Swaai, W. P. M., 1996. Discrete particle simulation of bubble and slug formation in a two-dimensional gas-fluidised bed: A hard sphere approach. Chemical Engineering Science 51 (1), 99–118.

Jakobsen, H. A., Lindborg, H., Dorao, C. A., 2005. Modeling of bubble column reactors: Progress and limitations. Industrial and Engineering Chemistry Research 44, 5107–5151.

Juncu, G., 1999. A numerical study of steady viscous flow past a fluid sphere. International Journal of Heat and Fluid Flow 20, 414–421.

Lapin, A., Lubbert, A., 1994. Numerical simulatin of the dynamics of two-phase gas-liquid flows in bubble columns. Chemical Engineering Science 49, 3661–3674.

Launder, B. E., Reece, G. J., Rodi, W., 1975. Progress in the development of a Reynolds-stress turbulence closure. Journal of Fluid Mechanics 68, 537–566.

Launder, B. E., Spalding, D. B., 1974. The numerical computation of turbulent flows. Computer Methods in Applied Mechanics and Engineering 3, 269–289.

Logan, D. L., 2002. A First Course in the Finite Element Method. Brooks and Cole, California.

Nakamura, I., 1976. Steady wake behind a sphere. Physics of Fluids 19, 5–8.

Navier, C. L. M. H., 1822. Memoire sur les lois du mouvement des fluides. Mem. Acad. Sci. Inst. France 6, 389–440.

Odar, F., Hamilton, W. S., 1964. Forces on a sphere accelerating in a viscous liquid. Journal of Fluid Mechanics 18, 302.

Pan, Y., Banerjee, S., 1997. Numerical investigation of the effects of large particles on wall-turbulence. Physics of Fluids 9, 3786–3807.

Rudman, M., 1997. Volume-tracking methods for interfacial flow calculations. International Journal for Numerical Methods in Fluids 24, 671–691.

Schwarz, M. P., Turner, W. J., 1988. Applicability of the standard k-e turbulence model to gas-stirred baths. Applied Mathematical Modelling 12, 273–279.

Smagorinsky, J., 1963. General circulation experiments with the primitive equations. I. The basic experiment. Mon. Weather Rev. 91 (3), 99–164.

Sokolichin, A., Eigenberger, G., 1994. Gas-liquid flow in bubble columns and loop reactors: part I. Detailed modelling and numerical simulation. Chemical Engineering Science 49, 5735–5746.

Stewart, J., 2001. Calculus: Concepts and Contexts., 5th Edition. Brooks and Cole, California.

Taneda, S., 1956. Experimental investigation of the wake behind a sphere at low Reynolds numbers. Journal of the Physical Society of Japan 11, 1104–1108.

Torvic, R., Svendsen, H. F., 1990. Modelling of slurry reactors: A fundamental approach. Chemical Engineering Science 45, 2325–2332.

Versteeg, H. K., Malalasekera, W., 2007. An Introduction to Computational Fluid Dynamics: The Finite Volume Method., 2nd Edition. Prentice Hall, London.

Webb, C., Que, F., Senior, P. R., 1992. Dynamic simulation of gas-liquid dispersion behaviour in a 2-d bubble column using a graphics mini-supercomputer. Chemical Engineering Science 47, 3305–3312.

Yuu, S., Yasukouchi, N., Hirosawa, Y., Jotaki, T., 1978. Particle diffusion in a dust laden round jet. AIChE Journal 24, 509.

Zienkiewicz, O. C., Taylor, R. L., 2000. The Finite Element Method, Volume 3: Fluid Dynamics., 5th Edition. Butterworth-Heinemann, Oxford.

Appendix A

Derivation of the Navier-Stokes Equations

In this appendix, the mass, momentum and energy balances are derived from first principles for incompressible fluid flow in 3-D. The substantial derivative, which is used in these balances is introduced first.

A.1 The Substantial Derivative

The substantial derivative is given by equation (A.1).

$$\frac{D\phi}{Dt} = \frac{\partial\phi}{\partial t} + \frac{\partial\phi}{\partial x}\frac{dx}{dt} + \frac{\partial\phi}{\partial y}\frac{dy}{dt} + \frac{\partial\phi}{\partial z}\frac{dz}{dt} \tag{A.1}$$

For a given particle, the property per unit mass, ϕ, is a function of position (x, y, z) and time, t. Buffler (2007) stated that the terms

$$\frac{\partial\phi}{\partial x}\frac{dx}{dt} + \frac{\partial\phi}{\partial y}\frac{dy}{dt} + \frac{\partial\phi}{\partial z}\frac{dz}{dt}$$

are the convective part of the function and describe the variation of ϕ in space. The term $\frac{\partial\phi}{\partial t}$ is local and describes the variation in the field with time at a given point. The substantial derivative is used when the particle is not following the flow field. In the case of a fluid particle which follows the flow field, $\frac{\partial x}{\partial t} = v_x$, $\frac{\partial y}{\partial t} = v_y$ and $\frac{\partial z}{\partial t} = v_z$. The total derivative is given by equation (A.2) (Versteeg and Malalasekera, 2007).

$$\frac{D\phi}{Dt} = \frac{\partial\phi}{\partial t} + \frac{\partial\phi}{\partial x}v_x + \frac{\partial\phi}{\partial y}v_y + \frac{\partial\phi}{\partial z}v_x \tag{A.2}$$

The total derivative can be expressed in a slightly different form too:

$$\frac{\partial(\rho\phi)}{\partial t} + div(\rho\phi\mathbf{v}) =$$

$$= \rho\frac{\partial\phi}{\partial t} + \phi\frac{\partial\rho}{\partial t} + \rho\phi div\mathbf{v} + \mathbf{v}grad(\rho\phi)$$

$$= \rho\frac{\partial\phi}{\partial t} + \phi\frac{\partial\rho}{\partial t} + \rho\phi div\mathbf{v} + \rho\mathbf{v}grad\phi + \phi\mathbf{v}grad\rho$$

$$= \rho\left[\frac{\partial\phi}{\partial t} + \mathbf{v}grad\phi\right] + \phi\left[\frac{\partial\rho}{\partial t} + \rho div\mathbf{v} + \mathbf{v}grad\rho\right]$$

$$= \rho\left[\frac{\partial\phi}{\partial t} + \mathbf{v}grad\phi\right] + \phi\left[\frac{\partial\rho}{\partial t} + div(\rho\mathbf{v})\right]$$

$$= \rho\left[\frac{\partial\phi}{\partial t} + \mathbf{v}grad\phi\right]$$

$$= \rho\frac{D\phi}{Dt}$$

Where $div(\rho\mathbf{v}) = \rho div\mathbf{v} + \mathbf{v}grad\rho$

The term, $\phi\left[\frac{\partial\rho}{\partial t} + div(\rho\mathbf{v})\right]$ equates to zero due to the mass conservation equation, which will be formulated in the next section (Versteeg and Malalasekera, 2007).

A.2 Derivation of the Continuity Equation

This derivation was extracted from (Geankoplis, 2003).

From the law of conservation of mass:
(rate of mass into fluid element)-(rate of mass out of fluid element)=(accumulation of mass inside fluid element)

Figure A.1 illustrates a typical fluid element.

In the x-direction:

(rate of mass in)=$(\rho v_x)_x \Delta y \Delta z$
(rate of mass out)=$(\rho v_x)_{x+\Delta x} \Delta y \Delta z$
(accumulation)=$\frac{\partial\rho}{\partial t}\Delta x \Delta y \Delta z$
Mass flow equations for the y-direction and the z-direction are obtained in a similar way. Adding all these expressions and dividing by $\Delta x \Delta y \Delta z$ gives eq. (A.3).

$$\frac{(\rho v_x)_x - (\rho v_x)_{x+\Delta x}}{\Delta x} + \frac{(\rho v_y)_y - (\rho v_y)_{y+\Delta y}}{\Delta y} + \frac{(\rho v_z)_z - (\rho v_z)_{z+\Delta z}}{\Delta z} = \frac{\partial\rho}{\partial t} \qquad \text{(A.3)}$$

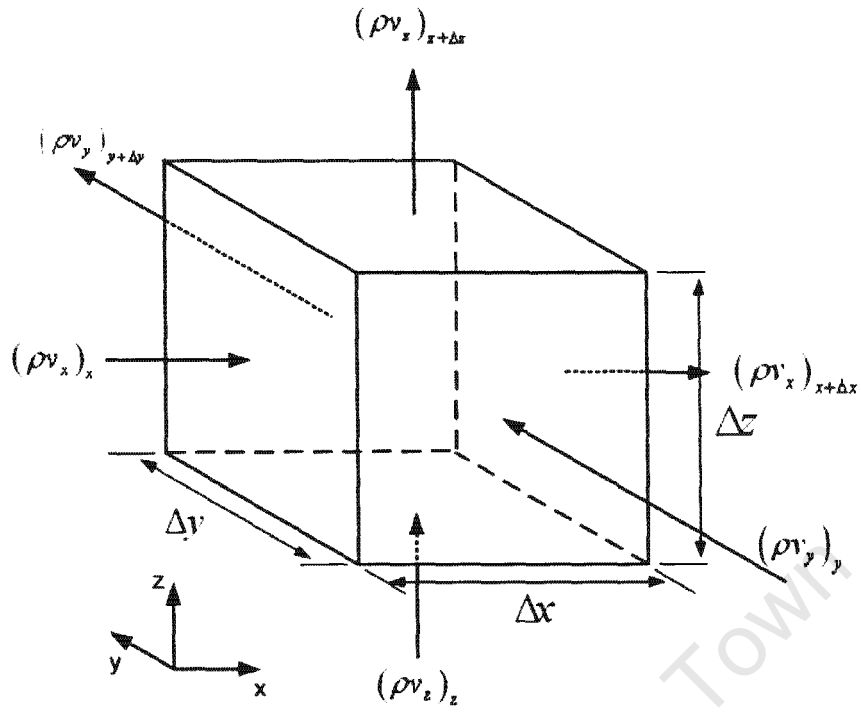

Figure A.1: Mass fluxes into and out of a fluid element.

Taking the limit as Δx, Δy and Δz each approach zero yields eq. (A.4), which is the mass balance equation.

$$\frac{\partial \rho}{\partial t} = -\left[\frac{\partial(\rho v_x)}{\partial x} + \frac{\partial(\rho v_y)}{\partial y} + \frac{\partial(\rho v_z)}{\partial z}\right] = -(\nabla \cdot \rho \mathbf{v}) \tag{A.4}$$

For incompressible fluids of constant density, eq. (A.4) becomes the continuity equation, eq. (A.5).

$$(\nabla \cdot \mathbf{v}) = (\frac{\partial v_x}{\partial x} + \frac{\partial v_y}{\partial y} + \frac{\partial v_z}{\partial z}) = 0 \tag{A.5}$$

$$\nabla \cdot \mathbf{v} = 0$$

A.3 Derivation of the Momentum Balance

This derivation was extracted from (Versteeg and Malalasekera, 2007) and (Geankoplis, 2003).

The starting point is Newton's second law which states that the sum of the forces acting on a fluid element equals the rate of change of momentum of that fluid element. This is

given in eq. (A.6).

$$\sum \mathbf{F} = \frac{d\mathbf{P}}{dt} \tag{A.6}$$

The sum of forces acting on a fluid element equals the rate of change of momentum of that fluid element. This can also be expressed as:

(rate of momentum in) - (rate of momentum out) + (sum of forces acting on system) = (rate of momentum accumulation)

In the x-direction:

(rate of momentum in)$=(\rho v_x v_x)_x \Delta y \Delta z + (\rho v_y v_x)_y \Delta x \Delta z + (\rho v_z v_x)_z \Delta x \Delta y$
(rate of momentum out)$=(\rho v_x v_x)_{x+\Delta x} \Delta y \Delta z + (\rho v_y v_x)_{y+\Delta y} \Delta x \Delta z + (\rho v_z v_x)_{z+\Delta z} \Delta x \Delta y$
(accumulation of momentum)$=\frac{\partial(\rho v_x)}{\partial t} \Delta x \Delta y \Delta z$

Inserting the terms above into the expression for the conservation of momentum, dividing by $\Delta x \Delta y \Delta z$ and taking the limit as $\Delta x, \Delta y$ and Δz each approach zero yields eq. (A.7).

$$\frac{\partial(\rho v_x)}{\partial t} = -\left[\frac{\partial(\rho v_x v_x)}{\partial x} + \frac{\partial(\rho v_y v_x)}{\partial y} + \frac{\partial(\rho v_z v_x)}{\partial z}\right] + \sum F_x \tag{A.7}$$

Note that the term in square brackets represents the net momentum flow in the x-direction by convection. Expanding eq. (A.7) gives eq. (A.8).

$$\begin{aligned} \rho\frac{\partial v_x}{\partial t} + v_x\frac{\partial \rho}{\partial t} = &-\left[v_x\frac{\partial(\rho v_x)}{\partial x} + \rho v_x\frac{\partial v_x}{\partial x} + v_x\frac{\partial(\rho v_y)}{\partial y}\right] \\ &-\left[\rho v_y\frac{\partial v_x}{\partial y} + v_x\frac{\partial(\rho v_z)}{\partial z} + \rho v_z\frac{\partial v_x}{\partial z}\right] + \sum F_x \end{aligned} \tag{A.8}$$

Using the general form of the continuity equation, eq. (A.4), and multiplying through by v_x gives eq. (A.9).

$$v_x\frac{\partial \rho}{\partial t} = -[v_x\frac{\partial(\rho v_x)}{\partial x} + v_x\frac{\partial(\rho v_y)}{\partial y} + v_x\frac{\partial(\rho v_z)}{\partial z}] \tag{A.9}$$

By substituting eq. (A.9) into eq. (A.8), the result is eq. (A.10).

$$\rho\frac{\partial v_x}{\partial t} = -\left[\rho v_x\frac{\partial v_x}{\partial x} + \rho v_y\frac{\partial v_x}{\partial y} + \rho v_z\frac{\partial v_x}{\partial z}\right] + \sum F_x \tag{A.10}$$

Rearranging eq. (A.10) gives eq. (A.11).

$$\rho\left(\frac{\partial v_x}{\partial t} + v_x\frac{\partial v_x}{\partial x} + v_y\frac{\partial v_x}{\partial y} + v_z\frac{\partial v_x}{\partial z}\right) = \sum F_x \tag{A.11}$$

Using the definition of the total derivative, the result is eq. (A.12).

$$\rho\frac{Dv_x}{Dt} = \sum F_x \tag{A.12}$$

In a similar manner equations (A.13) and (A.14) may be derived for the y and z directions respectively.

$$\rho\frac{Dv_y}{Dt} = \sum F_y \tag{A.13}$$

$$\rho\frac{Dv_z}{Dt} = \sum F_z \tag{A.14}$$

The forces acting on the fluid element can be grouped into two categories, namely surfaces forces and body forces. Surface forces include pressure and viscous forces. Body forces include centrifugal, gravitational, Coriolis and electromagnetic forces. Body forces are included in the overall source term in the momentum equation. An illustration of a fluid element is shown in Figure A.2, where τ_{ij} denotes viscous stress. The subscript i denotes the surface normal and the j denotes the direction of the stress. The stress τ_{ii} indicates the *total* normal stress, excluding pressure which is dealt with separately.

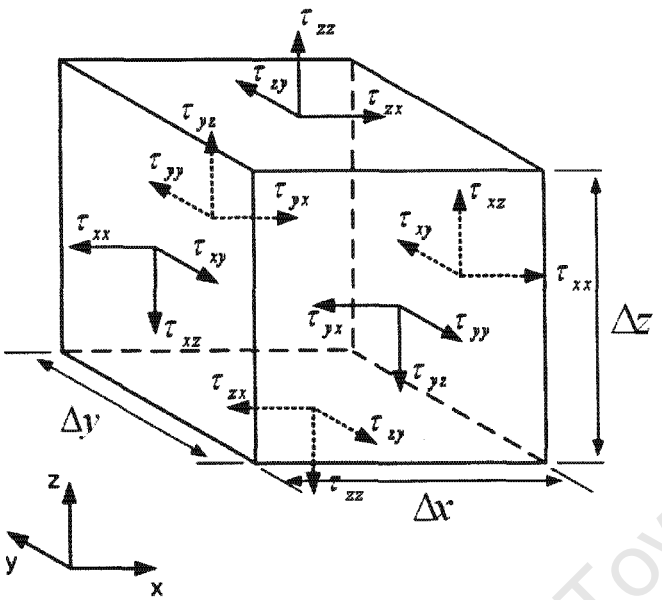

Figure A.2: Stress components on a fluid element.

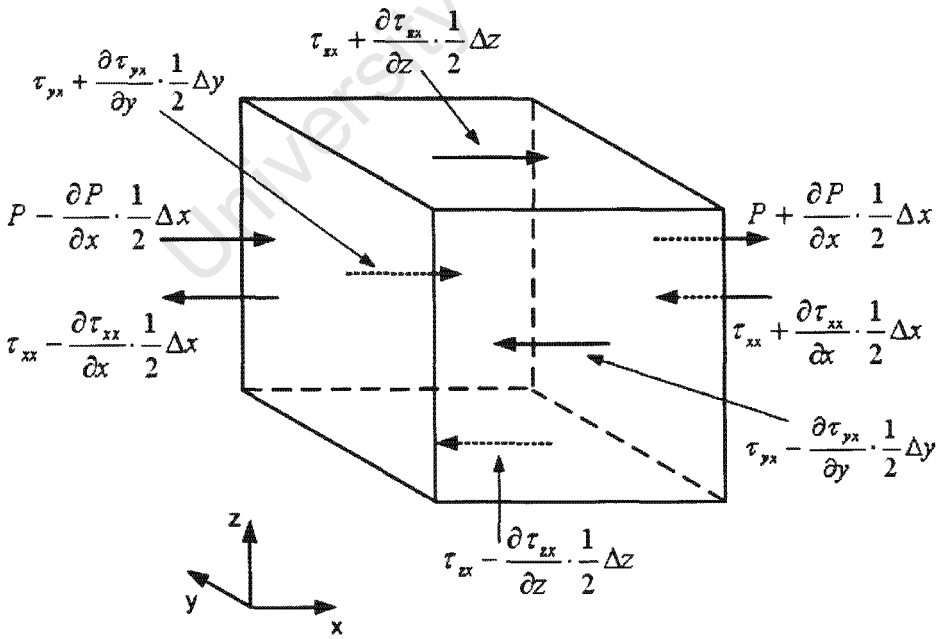

Figure A.3: Stress and pressure components on a fluid element in the x-direction.

In the x-direction:

The total force due to surface stresses can be calculated with the aid of Figure A.3. The stress and pressure terms which are shown on each of the faces in Figure A.3 represent the respective quantities at the center of the face. The net force for the East and West faces is:

$$\left[\left(P - \tfrac{\partial P}{\partial x}\tfrac{1}{2}\Delta x\right) - \left(\tau_{xx} - \tfrac{\partial \tau_{xx}}{\partial x}\tfrac{1}{2}\Delta x\right)\right]\Delta y\Delta z + \left[-\left(P + \tfrac{\partial P}{\partial x}\tfrac{1}{2}\Delta x\right) + \left(\tau_{xx} + \tfrac{\partial \tau_{xx}}{\partial x}\tfrac{1}{2}\Delta x\right)\right]\Delta y\Delta z$$

The net force for the North and South faces is:

$$-\left(\tau_{yx} - \frac{\partial \tau_{yx}}{\partial y}\frac{1}{2}\Delta y\right)\Delta x\Delta z + \left(\tau_{yx} + \frac{\partial \tau_{yx}}{\partial y}\frac{1}{2}\Delta y\right)\Delta x\Delta z$$

The net force for the Top and Bottom faces is:

$$-\left(\tau_{zx} - \frac{\partial \tau_{zx}}{\partial z}\frac{1}{2}\Delta z\right)\Delta x\Delta y + \left(\tau_{zx} + \frac{\partial \tau_{zx}}{\partial z}\frac{1}{2}\Delta z\right)\Delta x\Delta y$$

Adding the forces for each of the faces and diving by the control volume ($\Delta x\Delta y\Delta z$) gives the net force due to surface stresses:

$$\frac{\partial\left(-P + \tau_{xx}\right)}{\partial x} + \frac{\partial \tau_{yx}}{\partial y} + \frac{\partial \tau_{zx}}{\partial z}$$

Equating the net surface force and source term with the rate of change of momentum in the x-direction gives eq. (A.15).

$$\rho\frac{Dv_x}{Dt} = \frac{\partial\left(-P + \tau_{xx}\right)}{\partial x} + \frac{\partial \tau_{yx}}{\partial y} + \frac{\partial \tau_{zx}}{\partial z} + S_x \tag{A.15}$$

In a similar manner equations (A.16) and (A.17) may be derived for the y and z directions respectively.

$$\rho\frac{Dv_y}{Dt} = \frac{\partial \tau_{xy}}{\partial x} + \frac{\partial\left(-P + \tau_{yy}\right)}{\partial y} + \frac{\partial \tau_{zy}}{\partial z} + S_y \tag{A.16}$$

$$\rho\frac{Dv_z}{Dt} = \frac{\partial \tau_{xz}}{\partial x} + \frac{\partial \tau_{yz}}{\partial y} + \frac{\partial\left(-P + \tau_{zz}\right)}{\partial z} + S_z \tag{A.17}$$

For Newtonian fluids, the viscous stresses are proportional to the rates of deformation. The viscous stress components are given by equations (A.18) to (A.23).

$$\tau_{xx} = 2\mu\frac{\partial v_x}{\partial x} + \lambda\left(\nabla \cdot \mathbf{v}\right) \tag{A.18}$$

$$\tau_{yy} = 2\mu\frac{\partial v_y}{\partial y} + \lambda\left(\nabla \cdot \mathbf{v}\right) \tag{A.19}$$

$$\tau_{zz} = 2\mu\frac{\partial v_z}{\partial z} + \lambda\left(\nabla \cdot \mathbf{v}\right) \tag{A.20}$$

$$\tau_{xy} = \tau_{yx} = \mu\left(\frac{\partial v_x}{\partial y} + \frac{\partial v_y}{\partial x}\right) \tag{A.21}$$

$$\tau_{xz} = \tau_{zx} = \mu\left(\frac{\partial v_x}{\partial z} + \frac{\partial v_z}{\partial x}\right) \tag{A.22}$$

$$\tau_{yz} = \tau_{zy} = \mu\left(\frac{\partial v_y}{\partial z} + \frac{\partial v_z}{\partial y}\right) \tag{A.23}$$

The dynamic viscosity, μ, relates stress to linear deformation and the second viscosity, λ, relates stress to volumetric deformation. For incompressible fluids, $\nabla \cdot \mathbf{v} = 0$, thus the second viscosity term is neglected. These viscous stress terms are derived from first principles (Bennett, 1962). Equation (A.24) arises from the definition of viscosity.

$$\tau = \mu\frac{dv_x}{dy} \tag{A.24}$$

Figure A.4 illustrates the deformation of a fluid element.

The fluid element deforms by an angle, $d\phi$, over time, $d\theta$, given in eq. (A.25).

$$d\phi = -\frac{\frac{dv_x}{dy}dyd\theta}{dy} \tag{A.25}$$

Equation (A.25) simplifies to eq. (A.26).

$$\frac{d\phi}{d\theta} = -\frac{dv_x}{dy} \tag{A.26}$$

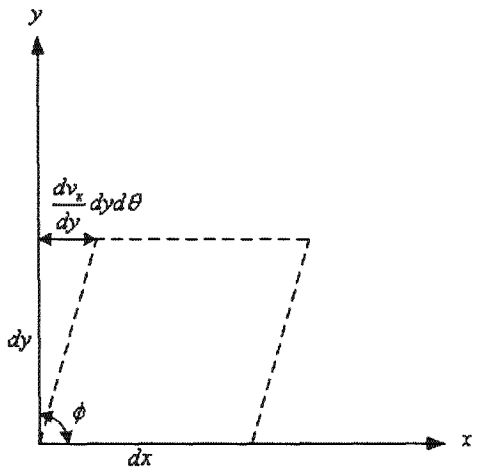

Figure A.4: Deformation of a two-dimensional fluid element due to shear.

Substitution of equation (A.26) into eq. (A.24) gives eq. (A.27).

$$\tau = -\mu\frac{d\phi}{d\theta} \tag{A.27}$$

Figure A.5 illustrates the deformation of another hypothetical fluid element.

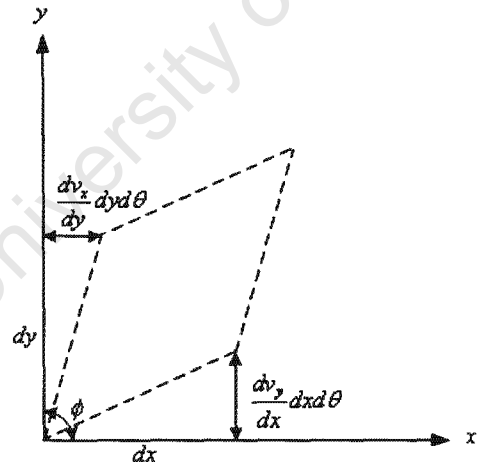

Figure A.5: Deformation of a two-dimensional fluid element due to shear.

The fluid element deforms by an angle, $d\phi$, over time, $d\theta$, given in eq. (A.28).

$$d\phi = -\frac{\frac{dv_x}{dy}dyd\theta}{dy} - \frac{\frac{dv_y}{dx}dxd\theta}{dx} \tag{A.28}$$

Equation (A.28) simplifies to eq. (A.29).

$$\frac{d\phi}{d\theta} = -\frac{dv_x}{dy} - \frac{dv_y}{dx} \tag{A.29}$$

Substitution of equation (A.29) into eq. (A.27) gives eq. (A.21). Equations (A.22) and (A.23) can be derived in a similar manner. The general relationship can be concluded from equations (A.21) to (A.23):

$$\tau_{ii} = \mu\left(\frac{dv_i}{di} + \frac{dv_i}{di}\right) = 2\mu\frac{dv_i}{di}$$

The substitution of the viscous stresses from equations (A.18) to (A.23) into eq. (A.15) gives eq. (A.30).

$$\rho\frac{Dv_x}{Dt} = \frac{\partial}{\partial x}\left(-P + 2\mu\frac{\partial v_x}{\partial x}\right) + \mu\frac{\partial}{\partial y}\left(\frac{\partial v_x}{\partial y} + \frac{\partial v_y}{\partial x}\right) + \mu\frac{\partial}{\partial z}\left(\frac{\partial v_x}{\partial z} + \frac{\partial v_z}{\partial x}\right) + S_x \tag{A.30}$$

Multiplying the terms out gives eq. (A.31).

$$\rho\frac{Dv_x}{Dt} = -\frac{\partial P}{\partial x} + 2\mu\frac{\partial^2 v_x}{\partial x^2} + \mu\frac{\partial^2 v_x}{\partial y^2} + \mu\frac{\partial^2 v_x}{\partial z^2} + \mu\frac{\partial^2 v_y}{\partial x \partial y} + \mu\frac{\partial^2 v_z}{\partial x \partial z} + S_x \tag{A.31}$$

Rearranging the terms in eq. (A.31) gives eq. (A.32).

$$\rho\frac{Dv_x}{Dt} = -\frac{\partial P}{\partial x} + \mu\frac{\partial^2 v_x}{\partial x^2} + \mu\frac{\partial^2 v_x}{\partial y^2} + \mu\frac{\partial^2 v_x}{\partial z^2} + \mu\frac{\partial}{\partial x}\left(\frac{\partial v_x}{\partial x} + \frac{\partial v_y}{\partial y} + \frac{\partial v_z}{\partial z}\right) + S_x \tag{A.32}$$

Substituting the continuity equation $[(\nabla \cdot \mathbf{v}) = 0]$ into eq. (A.32) gives eq. (A.33).

$$\rho\frac{Dv_x}{Dt} = -\frac{\partial P}{\partial x} + \mu\nabla^2 v_x + S_x \tag{A.33}$$

In a similar manner equations (A.16) and (A.17) can be modified to form equations (A.34) and (A.35).

$$\rho\frac{Dv_y}{Dt} = -\frac{\partial P}{\partial y} + \mu\nabla^2 v_y + S_y \tag{A.34}$$

$$\rho\frac{Dv_z}{Dt} = -\frac{\partial P}{\partial z} + \mu\nabla^2 v_z + S_z \tag{A.35}$$

Equations (A.34) and (A.35) are represented in vector form in eq. (A.36).

$$\rho\frac{D\mathbf{v}}{Dt} = -\nabla P + \mu\nabla^2\mathbf{v} + \mathbf{F} \tag{A.36}$$

A.4 Converting the Navier-Stokes Equations into a Dimensionless Form

This derivation was reported in the work by (Clift et al., 1978).

The momentum balance in the Navier-Stokes equations is given by eq. (A.37).

$$\rho\frac{D\mathbf{v}}{Dt} = -\nabla P + \mu\nabla^2\mathbf{v} + \mathbf{F} \tag{A.37}$$

The following dimensionless quantities are defined, where the variables L, V_o, p_o and h_v are reference quantities.

$$\mathbf{v}' = \frac{\mathbf{v}}{V_o}, \quad x' = \frac{x}{L}, \quad y' = \frac{y}{L}, \quad z' = \frac{z}{L}, \quad t' = \frac{tV_o}{L}$$

$$P_m{}' = \frac{(p - p_o - \rho g h_v)}{\rho {V_o}^2}, \quad Re = \frac{\rho L V_o}{\mu}$$

Expanding the total derivative term in equation (A.37) gives eq. (A.38):

$$\rho\frac{\partial\mathbf{v}}{\partial t} + \rho\mathbf{v}\cdot\nabla\mathbf{v} = -\nabla P + \mu\nabla^2\mathbf{v} + \mathbf{F} \tag{A.38}$$

Each term can be written in terms of dimensionless quantities, as shown below.

$$\rho\frac{\partial\mathbf{v}}{\partial t} = \rho\frac{\partial\mathbf{v}'}{\partial t'}\cdot\frac{{V_o}^2}{L}$$

$$\begin{aligned}
\rho\mathbf{v}\cdot\nabla\mathbf{v} &= \rho\left[\frac{\partial\mathbf{v}}{\partial x}v_x + \frac{\partial\mathbf{v}}{\partial y}v_y + \frac{\partial\mathbf{v}}{\partial z}v_z\right] \\
&= \rho\left[\frac{\partial\mathbf{v}'}{\partial x'}{v_x}'\left(\frac{{V_o}^2}{L}\right) + \frac{\partial\mathbf{v}'}{\partial y'}{v_y}'\left(\frac{{V_o}^2}{L}\right) + \frac{\partial\mathbf{v}'}{\partial z'}{v_z}'\left(\frac{{V_o}^2}{L}\right)\right] \\
&= \frac{\rho {V_o}^2}{L}\mathbf{v}'\cdot\nabla\mathbf{v}'
\end{aligned}$$

$$\begin{aligned}\nabla P &= \left(\frac{\partial P'}{\partial x'}\cdot\frac{\rho {V_o}^2}{L}, \quad \frac{\partial P'}{\partial y'}\cdot\frac{\rho {V_o}^2}{L}, \quad \frac{\partial P'}{\partial z'}\cdot\frac{\rho {V_o}^2}{L}\right) \\ &= \frac{\rho {V_o}^2}{L}\left(\frac{\partial P'}{\partial x'}, \quad \frac{\partial P'}{\partial y'}, \quad \frac{\partial P'}{\partial z}\right) \\ &= \frac{\rho {V_o}^2}{L}\nabla P'\end{aligned}$$

$$\begin{aligned}\mu\nabla^2\mathbf{v} &= \mu\left[\frac{\partial^2\mathbf{v}}{\partial x^2}+\frac{\partial^2\mathbf{v}}{\partial y^2}+\frac{\partial^2\mathbf{v}}{\partial z^2}\right] \\ &= \mu\left[\frac{\partial^2\mathbf{v}'}{\partial x'^2}\left(\frac{V_o}{L^2}\right)+\frac{\partial^2\mathbf{v}'}{\partial y'^2}\left(\frac{V_o}{L^2}\right)+\frac{\partial^2\mathbf{v}'}{\partial z'^2}\left(\frac{V_o}{L^2}\right)\right] \\ &= \frac{\mu V_o}{L^2}\left[\frac{\partial^2\mathbf{v}'}{\partial x'^2}+\frac{\partial^2\mathbf{v}'}{\partial y'^2}+\frac{\partial^2\mathbf{v}'}{\partial z'^2}\right] \\ &= \frac{\mu V_o}{L^2}\nabla^2\mathbf{v}'\end{aligned}$$

Inserting the modified terms back into the Navier-Stokes equation, eq. (A.38) results in eq. (A.39).

$$\rho\frac{\partial\mathbf{v}}{\partial t}\cdot\frac{{V_o}^2}{L}+\frac{\rho {V_o}^2}{L}\mathbf{v}'\cdot\nabla\mathbf{v}' = -\frac{\rho {V_o}^2}{L}\nabla P'+\frac{\mu V_o}{L^2}\nabla^2\mathbf{v}' \tag{A.39}$$

Dividing eq. (A.39) through by $\frac{\rho {V_o}^2}{L}$ produces the dimensionless form of the Navier-Stokes equation, eq. (A.40).

$$\frac{D\mathbf{v}'}{Dt'} = -\nabla P'+\frac{1}{Re}\nabla^2\mathbf{v}' \tag{A.40}$$

A.5 Derivation of the Energy Balance Equation

The derivation for the energy balance equation was extracted from (Versteeg and Malalasekera, 2007) and (Geankoplis, 2003).

The energy equation was derived from the first law of thermodynamics, which states that the rate of change of energy of a fluid particle is equal to the rate of heat addition to the particle plus the rate of work done on that particle. The rate of work done on the fluid element is equal to the product of the force and velocity components in the direction of the force. Figure A.3 was used to determine the total rate of work done in the x-direction, and the result is given in eq. (A.41).

$$\begin{aligned}\dot{W} = &\left[\left(Pv_x - \frac{\partial(Pv_x)}{\partial x}\cdot\frac{1}{2}\Delta x\right) - \left(\tau_{xx}v_x - \frac{\partial(\tau_{xx}v_x)}{\partial x}\cdot\frac{1}{2}\Delta x\right)\right]\Delta y\Delta z \\ &+\left[-\left(Pv_x + \frac{\partial(Pv_x)}{\partial x}\cdot\frac{1}{2}\Delta x\right) + \left(\tau_{xx}v_x + \frac{\partial(\tau_{xx}v_x)}{\partial x}\cdot\frac{1}{2}\Delta x\right)\right]\Delta y\Delta z \\ &+\left[-\left(\tau_{yx}v_x - \frac{\partial(\tau_{yx}v_x)}{\partial y}\cdot\frac{1}{2}\Delta y\right) + \left(\tau_{yx}v_x + \frac{\partial(\tau_{yx}v_x)}{\partial y}\cdot\frac{1}{2}\Delta y\right)\right]\Delta x\Delta z \\ &+\left[-\left(\tau_{zx}v_x - \frac{\partial(\tau_{zx}v_x)}{\partial z}\cdot\frac{1}{2}\Delta z\right) + \left(\tau_{zx}v_x + \frac{\partial(\tau_{zx}v_x)}{\partial z}\cdot\frac{1}{2}\Delta z\right)\right]\Delta x\Delta y\end{aligned} \tag{A.41}$$

Equation (A.41) simplifies to eq. (A.42).

$$\left[\frac{\partial(v_x(-P+\tau_{xx}))}{\partial x} + \frac{\partial(v_x\tau_{yx})}{\partial y} + \frac{\partial(v_x\tau_{zx})}{\partial z}\right]\Delta x\Delta y\Delta z \tag{A.42}$$

In a similar manner, the net work done by surface forces may be determined for the y-directions and z-directions, given in equations (A.43) and (A.44) respectively.

$$\left[\frac{\partial(v_y\tau_{xy})}{\partial x} + \frac{\partial(v_y(-P+\tau_{yy}))}{\partial y} + \frac{\partial(v_y\tau_{zy})}{\partial z}\right]\Delta x\Delta y\Delta z \tag{A.43}$$

$$\left[\frac{\partial(v_z\tau_{xz})}{\partial x} + \frac{\partial(v_z\tau_{yz})}{\partial y} + \frac{\partial(v_z(-P+\tau_{zz}))}{\partial z}\right]\Delta x\Delta y\Delta z \tag{A.44}$$

The total rate of work done on the fluid particle by surface stresses per unit volume is the sum of equations (A.42) to (A.44), and is expressed in eq. (A.45).

$$\begin{aligned}\dot{W} = &[-div(P\mathbf{v})] + \frac{\partial(v_x\tau_{xx})}{\partial x} + \frac{\partial(v_x\tau_{yx})}{\partial y} + \frac{\partial(v_x\tau_{zx})}{\partial z} + \frac{\partial(v_y\tau_{xy})}{\partial x} \\ &+\frac{\partial(v_y\tau_{yy})}{\partial y} + \frac{\partial(v_y\tau_{zy})}{\partial z} + \frac{\partial(v_z\tau_{xz})}{\partial x} + \frac{\partial(v_z\tau_{yz})}{\partial y} + \frac{\partial(v_z\tau_{zz})}{\partial z}\end{aligned} \tag{A.45}$$

The heat flux through the element can be calculated with the aid of Figure A.6.

The net rate of heat transfer by conduction in the x-direction is:

$$\left[\left(q_x - \frac{\partial q_x}{\partial x}\cdot\frac{1}{2}\Delta x\right) - \left(q_x + \frac{\partial q_x}{\partial x}\cdot\frac{1}{2}\Delta x\right)\right]\Delta y\Delta z$$

$$= -\frac{\partial q_x}{\partial x}\Delta x\Delta y\Delta z$$

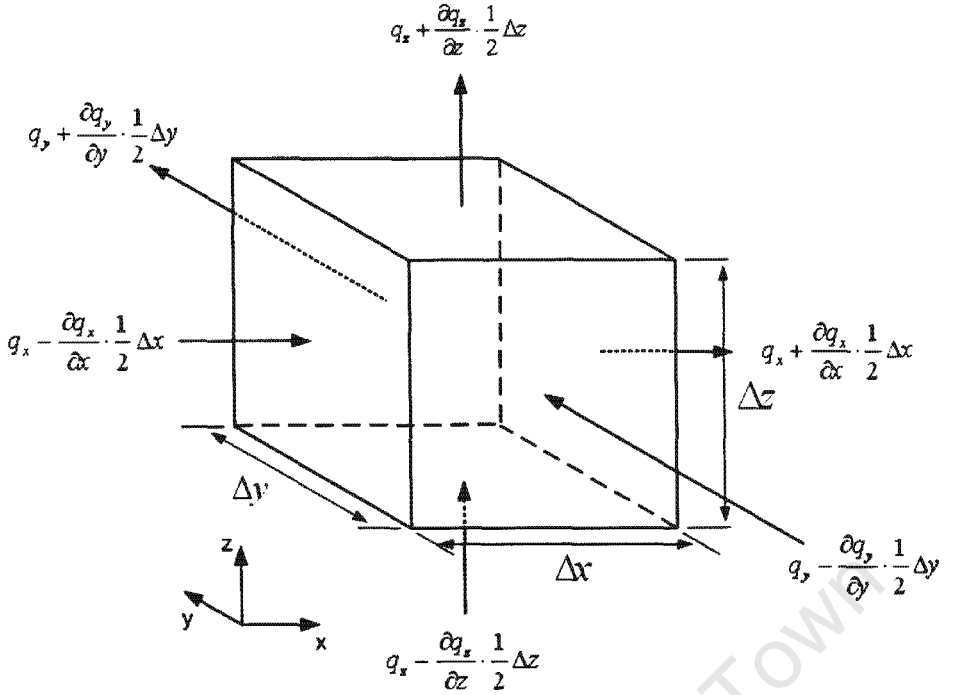

Figure A.6: Differential element including the heat fluxes through the element.

The net rates of heat transfer by conduction in the y and z directions are:

$$-\frac{\partial q_y}{\partial y}\Delta x\Delta y\Delta z$$

$$-\frac{\partial q_z}{\partial z}\Delta x\Delta y\Delta z$$

Adding the rates of heat transfer in each direction and dividing by the control volume gives the total rate of heat transfer due to heat flows, eq. (A.46).

$$\dot{Q} = -\frac{\partial q_x}{\partial x} - \frac{\partial q_y}{\partial y} - \frac{\partial q_z}{\partial z} \tag{A.46}$$

From Fourier's law of heat conduction:

$$q_x = -k\frac{\partial T}{\partial x}, \quad q_y = -k\frac{\partial T}{\partial y}, \quad q_z = -k\frac{\partial T}{\partial z}$$

Thus $\mathbf{q} = -k\ grad\ T$.
The final form for the total rate of heat flow by conduction into the particle for constant

k is eq. (A.47).

$$\dot{Q} = k\nabla^2 T \tag{A.47}$$

The total rate of change of energy, $\rho\frac{DE}{Dt}$, of a fluid particle is equal to the sum of equations (A.45) and (A.47), plus any other sources which includes gravitational potential energy. It should be mentioned that by analogy to the Navier-Stokes equations, the total derivative includes the convective fluxes of energy entering and leaving the differential volume element. The energy, E, includes both internal and kinetic energy. Thus the energy equation is eq. (A.48).

$$\begin{aligned}\rho\frac{DE}{Dt} = &-div\,(P\mathbf{v}) + \frac{\partial\,(v_x\tau_{xx})}{\partial x} + \frac{\partial\,(v_x\tau_{yx})}{\partial y} + \frac{\partial\,(v_x\tau_{zx})}{\partial z} + \frac{\partial\,(v_y\tau_{xy})}{\partial x} \\ &+ \frac{\partial\,(v_y\tau_{yy})}{\partial y} + \frac{\partial\,(v_y\tau_{zy})}{\partial z} + \frac{\partial\,(v_z\tau_{xz})}{\partial x} + \frac{\partial\,(v_z\tau_{yz})}{\partial y} + \frac{\partial\,(v_z\tau_{zz})}{\partial z} \\ &+ k\nabla^2 T + SE\end{aligned} \tag{A.48}$$

The component of internal energy is:

$$\rho\frac{D\left[0.5\left({v_x}^2 + {v_y}^2 + {v_z}^2\right)\right]}{Dt}$$

Expanding the component of internal energy gives eq. (A.49).

$$\begin{aligned}\rho\frac{D\left({v_x}^2\right)}{Dt} &= \frac{\partial\left({v_x}^2\right)}{\partial x}v_x + \frac{\partial\left({v_x}^2\right)}{\partial y}v_y + \frac{\partial\left({v_x}^2\right)}{\partial z}v_z + \frac{\partial\left({v_x}^2\right)}{\partial t} \\ &= 2v_x\frac{\partial v_x}{\partial x}v_x + 2v_x\frac{\partial v_x}{\partial y}v_y + 2v_x\frac{\partial v_x}{\partial z}v_z + 2v_x\frac{\partial v_x}{\partial t} \\ &= 2v_x\frac{Dv_x}{Dt}\end{aligned} \tag{A.49}$$

The internal energy term may be represented in the form eq. (A.50).

$$\begin{aligned}\rho\frac{D\left[0.5\left({v_x}^2 + {v_y}^2 + {v_z}^2\right)\right]}{Dt} &= v_x\rho\frac{Dv_x}{Dt} + v_y\rho\frac{Dv_y}{Dt} + v_z\rho\frac{Dv_z}{Dt} \\ &= -\mathbf{v}\cdot\nabla P + v_x\left(\frac{\partial\tau_{xx}}{\partial x} + \frac{\partial\tau_{yx}}{\partial y} + \frac{\partial\tau_{zx}}{\partial z}\right) \\ &\quad + v_y\left(\frac{\partial\tau_{xy}}{\partial x} + \frac{\partial\tau_{yy}}{\partial y} + \frac{\partial\tau_{zy}}{\partial z}\right) \\ &\quad + v_z\left(\frac{\partial\tau_{xz}}{\partial x} + \frac{\partial\tau_{yz}}{\partial y} + \frac{\partial\tau_{zz}}{\partial z}\right) + \mathbf{v}\cdot SM\end{aligned} \tag{A.50}$$

Subtracting eq. (A.50) from eq. (A.48) gives the internal energy equation, eq. (A.51).

$$\rho\frac{Di}{Dt} = -Pdiv\ \mathbf{v} + k\nabla^2 T + \tau_{xx}\frac{\partial v_x}{\partial x} + \tau_{yx}\frac{\partial v_x}{\partial y} + \tau_{zx}\frac{\partial v_x}{\partial z} + \tau_{xy}\frac{\partial v_y}{\partial x} + \tau_{yy}\frac{\partial v_y}{\partial y} + \tau_{zy}\frac{\partial v_y}{\partial z} + \tau_{xz}\frac{\partial v_z}{\partial x} + \tau_{yz}\frac{\partial v_z}{\partial y} + \tau_{zz}\frac{\partial v_z}{\partial z} + Si \tag{A.51}$$

Note that $Si = SE - \mathbf{v} \cdot SM$. Substituting equations (A.18) to (A.23) into eq. (A.51) and rearranging yields eq. (A.52).

$$\rho\frac{Di}{Dt} = -Pdiv\ \mathbf{v} + k\nabla^2 T + \Phi + Si \tag{A.52}$$

The term, Φ, is given in eq. (A.53).

$$\Phi = 2\mu\left[\left(\frac{\partial v_x}{\partial x}\right)^2 + \left(\frac{\partial v_y}{\partial y}\right)^2 + \left(\frac{\partial v_z}{\partial z}\right)^2\right] + \mu\left(\frac{\partial v_x}{\partial y} + \frac{\partial v_y}{\partial x}\right)^2 + \mu\left(\frac{\partial v_x}{\partial z} + \frac{\partial v_z}{\partial x}\right)^2 + \mu\left(\frac{\partial v_y}{\partial z} + \frac{\partial v_z}{\partial y}\right)^2 + \lambda(div\ \mathbf{v})^2 \tag{A.53}$$

Finally for the special case of an incompressible fluid, $i = C_p T$ and $(\nabla \cdot \mathbf{v}) = 0$, thus the temperature equation is presented in equation (A.54).

$$\rho C_p\frac{DT}{Dt} = -Pdiv\ \mathbf{v} + k\nabla^2 T + \Phi + Si \tag{A.54}$$

Appendix B

Sample Calculations

Calculation of the relative error

The volume averaged relative error calculation performed in Paraview was tested by constructing solutions with identical values throughout the domain for both the NVS and Stokes solutions and manually calculating the relative error. This calculation is performed below.

The NVS velocity at each node in the solution domain was set to $< 2, 2, 2 >$ and the Stokes velocity at each node was set to $< 0.5, 0.5, 0.5 >$. The volume averaged relative error obtained in Paraview for these two solutions was $\sqrt{0.75}$.

Using these solution fields, the relative error between the NVS and Stokes solutions at a node is:

$$err\,(x,y,z) = \frac{|\|\mathbf{u_{nvs}}\| - \|\mathbf{u_s}\||}{\|\mathbf{u_{nvs}}\|}$$

$$\|\mathbf{u_{nvs}}\| = \sqrt{2^2 + 2^2 + 2^2} = \sqrt{12}$$

$$\|\mathbf{u_s}\| = \sqrt{0.5^2 + 0.5^2 + 0.5^2} = \sqrt{0.75}$$

$$\therefore err\,(x,y,z) = \frac{\sqrt{12} - \sqrt{0.75}}{\sqrt{12}} = \sqrt{0.75}$$

The volume averaged error for the entire domain is:

$$\begin{aligned}\epsilon &= \frac{\int_V err\,(x,y,z)\,\mathrm{d}V}{V_{total}} \\ &= \frac{\int_V \sqrt{0.75}\mathrm{d}V}{V_{total}} \\ &= \sqrt{0.75}\end{aligned}$$

This value is exactly equal to the value calculated in Paraview.

Calculation of the average angle between the solution fields

The volume averaged angle calculation performed in Paraview was tested by constructing solutions with identical values throughout the domain for both the NVS and Stokes solutions and manually calculating the average angle. This calculation is performed below.

The NVS velocity at each node in the solution domain was set to $< 1,1,1 >$ and the Stokes velocity at each node was set to $< -1,-1,-1 >$.

The angle between the NVS and Stokes vectors at a node is

$$\begin{aligned}\theta_n &= arccos\left(\frac{\mathbf{u_{nvs,n}}\cdot\mathbf{u_{s,n}}}{\|\mathbf{u_{nvs,n}}\|\|\mathbf{u_{s,n}}\|}\right) \\ \theta_n &= arccos\left(\frac{<1,1,1>\cdot<-1,-1,-1>}{\|<1,1,1>\|\|<-1,-1,-1>\|}\right) \\ \theta_n &= arccos\left(\frac{-3}{\sqrt{3}\sqrt{3}}\right) \\ \theta_n &= arccos\,(-1) = \pi\end{aligned}$$

The volume averaged angle is

$$\begin{aligned}\overline{\theta} &= \frac{\int_V \theta\,(x,y,z)\,\mathrm{d}V}{V_{total}} \\ \overline{\theta} &= \frac{\int_V \pi\mathrm{d}V}{V_{total}} = \pi\end{aligned}$$

This value was exactly equal to the value calculated in Paraview.

Calculation of error introduced into $\overline{\theta}$ for Re=30

The calculation of the angle between vectors is inaccurate when the velocities approach zero. When two vectors both have velocities of zero, they are identical thus there should

be an angle of zero between them. When using the formulae for calculating the angle between these vectors, the result is 90°. Despite this, it is shown that for the flow around a solid sphere, where the velocity is specified as zero everywhere on the surface of the sphere, the error introduced is not significant. Thus for the flow around a bubble, where the velocities are higher, the error is even less significant. This calculation is shown below.

The refined cells on the surface of the sphere had a thickness of $\approx 1.1mm$.
Volume of single layer of cells around sphere $= \frac{4}{3}\pi\,(8.6 - 7.5)$
$=4.607669mm^3$
Total domain volume $= 265098mm^3$
Assume worst case of average cell angle of $90° = \pi/2$ radians
The volume integrated angle for the volume of cells around the sphere is

$$\theta = \int_V \frac{\pi}{2} \mathrm{d}V = 7.237709$$

The total volume integrated angle by Paraview including the error above = 13036.4
Percentage error=$\frac{7.237709}{13036.4} \times 100 = 0.05\%$

Effect of time step size on steady state solution

Figure B.1 provides the volume averaged relative error between a given steady NVS solution using a particular time step size with the NVS solution which used a time step size of 0.1 seconds. These NVS solutions were performed for flow around a bubble at a Reynolds number of 15. The volume averaged normalised angle is also plotted with time step size. Clearly the length of the time step does not change the steady state solution by much.

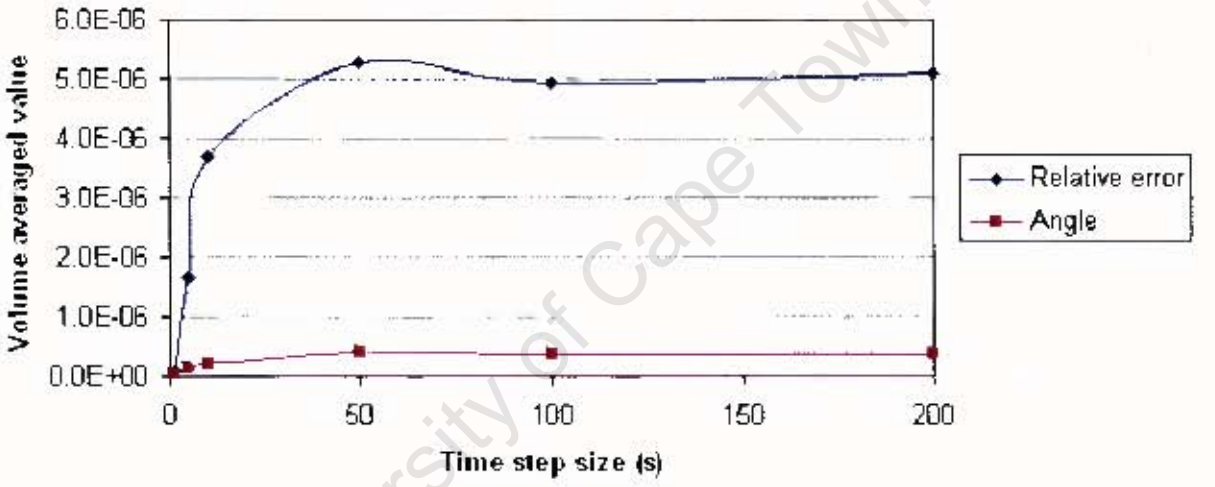

Figure B.1: Plot of the average relative error and average angle between the NVS solution using a step size of 0.1 seconds.